The research on preparation of ZnO nano-material and photoelectric devices

Zhen Guo

ÉCOLE DOCTORALE SCIENCES ET TECHNOLOGIE

Centre de Recherche sur la Matière Divisée

Changchun Institute of Optics, Fine Mechanics and Physics

THÈSE EN COTUTELLE INTERNATIONALE présentée par :

Zhen GUO

Soutenue le : 25 mai 2011

pour obtenir le grade de :

Docteur de l'université d'Orléans et du Chinese Academy of Sciences

Discipline : Physique

The research on preparation of ZnO Nano-material and photoelectric devices

---

Membres du JURY :

M Shiyong LIU, Professeur, Université de Jilin - Chine	Président
M Jacques ZHENG, Chargé de recherche, CNRS Paris	Rapporteur
M Bin YAO, Professeur, Université de Jilin – Chine	Rapporteur
M Hang Song Professeur, Académie des sciences Changchun – Chine	Examinateur
Mme Caroline ANDREAZZA, Maitre de conférences, Université d'Orléans	Directeur de thèse

Acknowledgements

Acknowledgements

The thesis was finished under supervisors of researcher Dongxu Zhao, researcher Caroline Andreazza-Vignolle, Prof Yichun Liu and researcher Pascal Andreazza. During learning and work, I deeply realized the care of my four teachers for the cultivation, I will never forget. I not only learned from them the knowledge and methods, but also learned a rigorous educational philosophy. Their vast knowledge, keen academic thinking, abundant scientific research experience and effective methods make me benefit greatly, I would like to express my sincere thanks to the four supervisors.

Researchers Dongxu Zhao and Caroline Andreazza-Vignolle gave careful instructions in the entire thesis work, from the selection of thesis and the experimental program, the results of discussion, I once again to express my deepest gratitude to researchers Dongxu Zhao and Caroline Andreazza-Vignolle.

In my own learning and work, I got a lot of guidance and help from teachers and students in II-VI semiconductor research group, open-minded attitude towards life, wise words of prof. Fan made me learn a lot of knowledge outside of books and made benefite me for all the life. I would like to thank researcher Chongxin Shan, Prof Bin Yao, Associate Professors Ji-Ying, Zhang Zhenzhong Zhang and Li Bing Hui, assistant researcher Shuangpeng Wang for useful discussions in the work.

I would like to thank the entire students in II-VI semiconductor research group for their support and help. Special thanks to post-doctors Lanlan Sun, Yong-Feng Li, Zhengang Ju, Dr. Yang Tang, Dr. Yanmin Zhao, Dr. Lin Li, Dr. Changji Zheng, Dr. Liang Guo, Dr. Lidan Wang, Dr. Meng Ding, Dr. Zhikun Xu, Dr. Zhongkui Zheng, Masters Zhiming Song, Fei Wang, Jing Zhang, Master liFei Tian in the experiments for give me helps and useful discussions.

I would like to thank researchers Xing-Yuan Liu, Ligong Zhang, Zhao Haifeng, Shi-Yong Luo and Xinguang Ren of key Laboratory of Excited States in Chinese Academy of Sciences and Annie Richard, Thierry Sauvage in Université d'Orléans for their help in measurements.

I would like to thank Hong Wei, Jingxuan Wang and other teachers of Changchun Institute of Optics, Fine Mechanics and Physics in Chinese Academy of Sciences for the care and assistance in life, study and work.

I would like to thank French government for supplying scholarship for my study; I would also like to thank all the persons in Crous d'Orleans-Tours such as Mrs Sylvie Rigard and so on.

I would also like to thank director Marie-Louise Sabounqi for the care and assistance in life.

I would like to thank secretary Nicole Nourry of Centre de Recherche sur la Matière Divisée, Centre National de la Recherche Scientifique for the care and assistance in life.

I would like to thank my parents, sister and brother for the understanding, full support, care and help of my learning and work.

Finally, I would like to give heartfelt thanks to all the people for their care and help during my work!

Préparation de nanostructures de ZnO et intégration dans des dispositifs photoélectriques

L'oxyde de Zinc (ZnO) est un oxyde semi-conducteur à large bande interdite (gap direct de 3.37 eV à température ambiante). Ce paramètre est fondamental pour des applications de type émission de lumière (lasers et diodes). De plus, une de ses principales caractéristiques est la valeur de l'énergie du premier exciton qui caractérise la stabilité de l'exciton et donc de l'état excité (60meV) qui est bien supérieure à celle des matériaux semi-conducteurs classiques (Si : 15meV, GaN : 25meV). Fort de ces caractéristiques, ZnO est un matériau qui a un fort potentiel applicatif. Il est déjà largement utilisé dans des domaines tels que la catalyse ou la cosmétique mais c'est dans le domaine de l'électronique, de l'optique et de la mécanique que les propriétés de ZnO paraissent les plus prometteuses. Pour l'industrie de l'électronique et notamment pour les applications dans le domaine des diodes électroluminescentes, la valeur de son gap permettrait l'obtention de diodes émettant dans le spectre UV. Il est possible d'envisager la conception de laser solide émettant dans l'UV et fonctionnant à température ambiante. La possibilité de générer de la lumière à partir de nanofils de ZnO permet également d'envisager la réalisation de nano-lasers. Toutes ces applications en font un matériau très largement étudié par la communauté scientifique internationale.

Cette thèse développe d'une part l'étude de la croissance contrôlée de nanostructures de ZnO sur différents supports et d'autre part l'étude de l'intégration de telles nanostructures dans des nano-composants.

Plusieurs méthodes de préparation ont été utilisées au cours de ce travail. L'élaboration par voie chimique en phase vapeur a permis, grâce au contrôle du flux d'oxygène d'obtenir des nanofils (croissance 1D) ou des « nanopilliers » (croissance 1D puis 2D). Par la méthode de synthèse hydrothermale, des nanofils sont obtenus de plusieurs microns de longueur, leur diamètre dépendant de la concentration des précurseurs (de 10 à 100nm). L'utilisation d'une sous couche de ZnO orientée, a permis l'obtention de réseaux de nanofils alignés perpendiculairement par rapport au support. Les paramètres de la sous-couche et notamment la taille des grains permet de contrôler la taille des nanofils et leur densité sur le support.

L'intégration de ces réseaux alignés de nanofils dans des nano-composants a

permis d'obtenir des résultats très prometteurs. Ainsi une émission stimulée a pu être obtenue avec ces réseaux de nanofils de ZnO orientés par pompage optique utilisant un laser femtoseconde présentant un seuil de 96KW/cm^2. Pour diminuer la valeur du seuil de l'émission stimulée, une couche de platine utilisée comme miroir de haute réflectivité a permis la diminution du seuil jusque 17.3KW/cm^2.

Un film mince monocristallin de GaN sur substrat de saphir a aussi été utilisé comme support. Par synthèse hydrothermale un film quasi continu de micro-tiges de ZnO a été obtenu, les micro-tiges présentant un arrangement périodiques avec des faces parallèles entre elles ce qui permet l'obtention d'une cavité résonante de qualité. Par pompage optique, une émission stimulée est observée dans ces hétérojonctions GaN / micro-tiges de ZnO. Des expériences d' électoluminescence ont montré une raie d'émission unique centrée à 407nm avec une largeur à mi-hauteur de 0.7nm. L'analyse des spectres de photoluminescence de ces hétérojonctions il a été montré que cette émission provenait des micro-tiges de ZnO.

Enfin, des réseaux très compacts de nanofils de ZnO sur substrat de silicium ont été obtenus par pulvérisation magnétron et ont permis la conception de nano-photodetecteurs.

Dans le premier chapitre de ce manuscrit, seront présentés le contexte de l'étude, ainsi qu'une étude bibliographique sur les domaines d'application des films minces et des nanostructures de ZnO dans les domaines des lasers UV, des diodes électroluminescentes, des photodétecteurs, …
Dans le second chapitre seront décrits les méthodes actuellement utilisées pour l'élaboration de nanostructures ou de films minces nanostructurés de ZnO ainsi que les méthodes de caractérisation morphologiques, structurales et électriques associées.
Le troisième chapitre présente les résultats obtenus sur la préparation des nanofils à la fois par la méthode de dépôt en phase vapeur et la synthèse hydrothermale ainsi que les méthodes utilisées pour orienter les nano-objets dans la perspective de former des réseaux alignés de nanofils.
Les chapitres 4 et 5 sont consacrés à l'intégration des nanostructures dans des nano-dispositifs et aux résultats obtenus sur leurs propriétés (électrique, photoluminescence et électroluminescence).
Enfin un bilan des résultats obtenus ainsi que les perspectives seront présentés dans le chapitre 6.

The Research on Preparation of ZnO Nano-material and Photoelectric Devices

Zinc Oxide (ZnO) is a wide band gap semiconductor material, which has a band gap of 3.37 eV at room temperature, its most important characteristic is the high exciton bounding energy of 60 meV. Based on these characteristics, ZnO has potential applications in short wavelength photoelectric devices. Since nanodevices such as ZnO nanowire based nanolasers, solar cells and nanogenerators were obtained, the applications of ZnO nanostructures in the photoelectric field have attracted wide spread interests in the international, which has become a hot spot in the nano-optoelectronic field of the international frontier topics. The dissertation develops the following creative research on the problems of the growth controlled ZnO nanostructures, design and preparation of nanodevices:

Exploring chemical vapor deposition method, through controlling the oxygen flux, the conversion from one dimensional (1D) to two dimensional (2D) growth was realized, thus ZnO nanobolt arrays were obtained; exploring hydrothermal method, through adjusting the size of the seed particle and solution concentration, ZnO nanowires with different size were obtained.

Exploring hydrothermal method aligned ZnO nanowires array on the ZnO seed film were obtained, the stimulated emission were observed with threshold of 96 KW/cm^2 excited by femtosecond laser in the optically pumped ZnO nanowires; in order to lower the threshold of the stimulated emission, Pt layer as a high reflectivity mirror was fabricated on Si substrate, optical loss has been effectively decreased, thus the threshold of the stimulated emission was further lowered to 17.3 KW/cm^2 for the optically pumped ZnO nanowires.

Using p-GaN single crystalline film as template, the quasi continuous ZnO micro-rods was obtained by hydrothermal method with multiple growth, these ZnO micro-rods present periodically arranged structure with parallel sides, and this kind of structure provides excellent resonance cavity. The stimulated emission was observed in optically pumped ZnO micro-rods; using p-GaN as carrier injection layer the heterojunction was formed with ZnO micro-rods, single mode lasing emission located at 407 nm with a full width at half maximum (FWHM) of 0.7 nm was obtained through electroluminescence (EL) measurement. Through comprehensive analysis of

the photoluminescence (PL) for the ZnO/GaN heterojunction, optically pumped stimulated emission and EL, the emission was originated from ZnO.

Closely packed ZnO nanowire array was fabricated on Si substrate by magnetron sputtering method, the visible and UV dual bands alternative photo-detection was realized through adjusting forward and reverse bias.

Table of Contents

Chapter 1 Introduction

1.1 Background and Significance of the Research

Currently the GaN based blue light devices have being commercially produced. Researchers found that ZnO material owning similar crystal structure, physical properties with GaN and large exciton bounding energy, which could be a new candidate for low threshold UV laser material. Therefore, the research on ZnO material has being the foundation in the field of optoelectronics internationally. ZnO is a direct wide band gap semiconductor material with the band gap of 3.37 eV and a large exciton binding energy of 60 meV at room temperature. [1,2] The exciton can not be ionized at room temperature, so the effective exciton emission can be obtained, which will greatly reduce the lasing threshold at room temperature. Because nano-materials own the properties that bulk materials do not have, such as larger surface area to volume ratio, quantum size effects, confinement effects and so on. Thus many researchers have devoted their interests to the research of ZnO nano-material. Nano-technology in the world is still in its infancy, a few countries such as United States, Japan, Germany, and France have some foundation, but they are still in the research period. The emergence of new theories and technologies are growing up. China has made efforts to catch up with the level of advanced countries, the research teams are also growing stronger.

1.2 Properties of ZnO

ZnO has a hexagonal wurtzite structure with lattice constant: a = 3.296 Å and c = 5.2065Å. The structure can be simply described as a four-coordinated $O^{2-}$and Zn^{2+} ions sub-lattice structure along the c-axis shown in Fig 1.1.

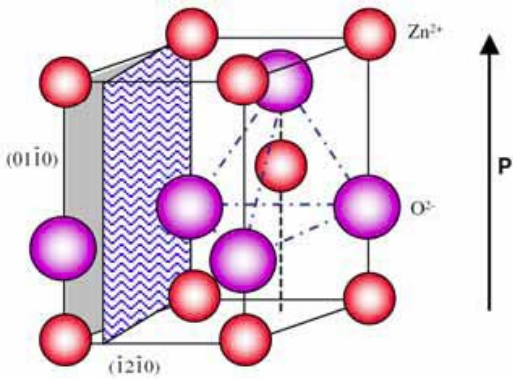

Fig. 1.1 Structural model of wurtzite ZnO, in which dot lines show tetrahedron structure of oxygen.

Due to existence of intrinsic defects such as interstitial Zn and O vacancy in ZnO, which result in deviation of the stoichiometric composition, intrinsic ZnO is a n-type semiconductor material. [3] Table 1.1 lists some basic properties of ZnO, as a comparison, Table 1.2 lists basic parameters of some common wide band gap semiconductor materials. It is observed that ZnO semiconductor material has some obvious characteristics such as higher melting point, wider band gap and larger exciton binding energy.

Table 1.1 Basic properties of ZnO material.

Properties	**Parameters**
Molecular Weight	81.389
Density（g/cm^3）	5.64
Melting point（°C）	1975
Specific heat（cal/g. °C）	0.125
Thermoelectricity constant (mV/K)	1200（300K）
Conductivity（Ω.cm）	10
Linear expansion coefficient（K^{-1}）	4.75 (a axis)， 2.92 (c axis)
Hardness	4.5
Thermal conductivity（W/cm.K）	1.16 (Zn plane)，1.10 (O plane)
Band gap（Room temperature）	3.37 eV
Exciton bounding energy	60 meV
Radiation resistance	2 MeV

Table 1.2 The common properties of some wide band gap semiconductor materials.

Material	Crystal Structure	Lattice constant		Band gap energy (eV)	Bounding energy (eV)	Melting point (K)	Exciton binding energy (meV)	Dielectric constant	
		a(Å)	c(Å)					ε (0)	ε (g)
ZnO	Wurtzite	3.25	5.207	3.37	1.89	2248	60	8.75	3.73
ZnS	Wurtzite	3.82	6.261	3.80	1.59	2103	30	9.6	5.7
ZnSe	Sphalerite	5.66		2.70	1.29	1793	20	9.1	6.3
GaAs	Sphalerite	5.65		1.43			4.2		
GaN	Wurtzite	3.19	5.185	3.39	2.24	1973	21	8.9	5.35
6H-SiC	Wurtzite	3.18	15.12	2.86	3.17	>2100		9.66	6.52

1.3 The Overview of ZnO Materials

1.3.1 The UV Lasers of Optically Pumped ZnO

(1) Optically pumped ZnO microcrystalline thin film UV lasers

During the years 1997-1998, Zhu Z and Tang Zikang who realized optically pumped ultraviolet (UV) stimulated emission in ZnO thin films at room temperature, [4,5,6] the research in ZnO has being set off a boom internationally.

Self-assembled ZnO microcrystallites with thickness of 200 nm were grown on sapphire substrate using the laser molecular beam epitaxy (MBE) technique by Tang Zikang et al. Fig. 1.2 shows the AFM topography of prepared ZnO thin film, [5] X-ray diffraction measurement revealed that the ZnO microcrystallites have high crystallinity with *c*-axis orientation. The thin film consists of close-packed hexagons as shown in AFM image.

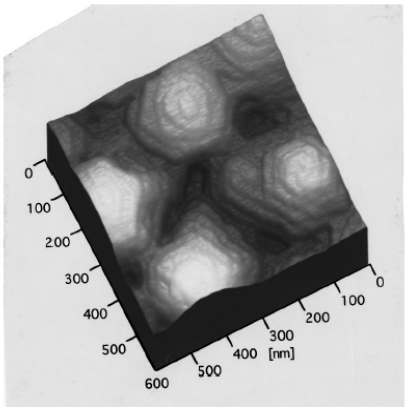

Fig 1.2 AFM top view image of ZnO epitaxial film grown on a sapphire (0001) substrate.

Using frequency-tripled output (355) nm from a pulsed Nd: YAG laser (15 ps, 10 Hz) as excitation source, Fig 1.3 shows the emission spectra pumped near a threshold I_{th} = 40 kW/cm^2 .[5]

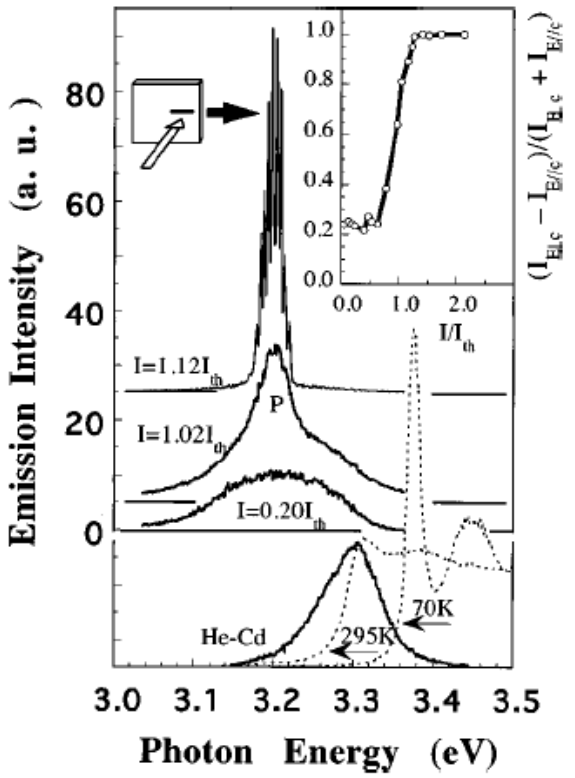

Fig 1.3 The lower trace shows the absorption spectrum (dotted curve) and photoluminescence spectrum, measured at 70 K and room temperature, respectively. The upper traces show spontaneous and stimulated emission spectra.

At low pump intensity, a broad emission band is observed at 3.2 eV which is lower than E_{ex} by about 110 meV. The intensity of this emission band increases quadratically when the pump intensity is below the threshold. When the ZnO film is pumped at an intensity just above the threshold, $I = 1.02I_{th}$, a narrow emission band P emerges directly from the broad spontaneous spectrum. The P band grows superlinearly with pump intensity. The origination of P band emission was considered as collisions among excitons. At higher pump intensity, many sharp lines equally spaced in energy appear in the emission spectrum. The above observations indicate unequivocally that room temperature (RT) UV lasing occurred in these ZnO microcrystallites.

(2) Optically pumped UV lasers based on ZnO polycrystalline thin film and powder

During the years 1998-2000, Cao Hui and others who observed random laser in optically pumped ZnO polycrystalline thin film and semiconductor powder, and their results have been published in Applied Physics letters and Physical Reviewer Letters. [7, 8,9]

ZnO powder with an average particle size of 100 nm was deposited onto ITO coated glass substrates by electrophoresis, thickness of the powder films varied from 6 to 15 μm. As shown in Fig 1.4 when the ZnO powder was optically pumped, at low excitation intensity, the spectrum was consisted of a single broad spontaneous emission peak.

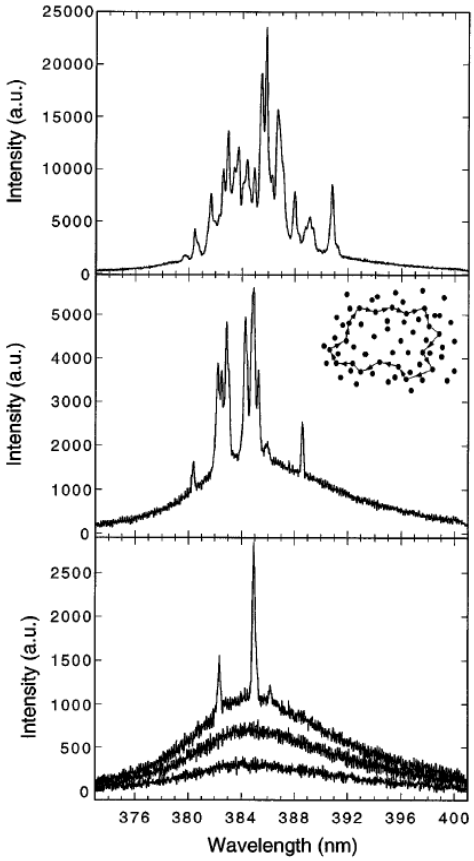

Fig 1.4 Emission spectra of ZnO powder when the excitation intensity is (from bottom to top) 400, 562, 763, 875, 1387 kW/cm^2.

As the pump power increased the emission peak became narrower due to the preferential amplification at frequencies close to the maximum of the gain spectrum. When the excitation intensity exceeded a threshold, very narrow peaks emerged in the emission spectra. The linewidth of these peaks was less than 0.3 nm, which was more than 30 times smaller than the linewidth of the amplified spontaneous emission peak below the threshold. When the pump intensity increased further, more sharp peaks appeared. It is found out that the stimulated emission in ZnO was due to the formation of the closed path by the strong scattering among the particles, thus the emission of coherent light was magnified.

(3) **Optically pumped ZnO NW array based UV lasers**

In the year 2001, Yang Peidong et al published an article related to the RT UV NW lasers in Science, [10] single ZnO NW with diameter of bout 100 nm and better orientation can be used as a micro-laser, so a wide spread range of researchers devoted their interests to the research of optically pumped ZnO nanostructure lasers.

As shown in Fig 1.5, ZnO NWs were synthesized by a vapor phase transport process via catalyzed epitaxial crystal growth. [10]

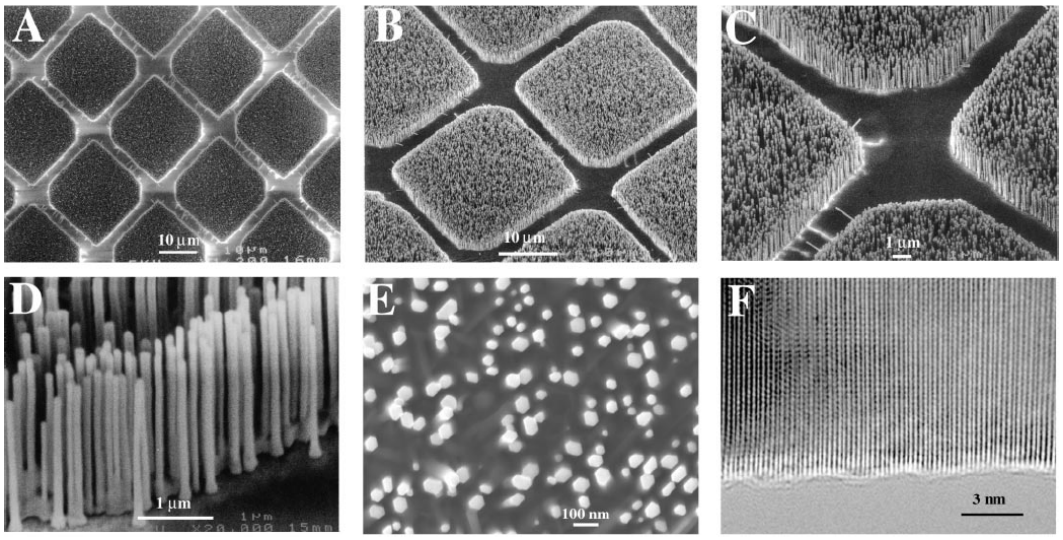

Fig 1.5 (A-E) SEM images of ZnO nanowire arrays grown on sapphire substrates, (F) High-resolution TEM image of an individual ZnO nanowire showing its (0001) growth direction.

Using Au thin film as the catalysts for NW growth, the NWs are highly oriented on the substrate. Selective NW growth can be readily achieved by patterning the Au thin film before growth. SEM images of NW arrays grown on sapphire (110)

substrates with patterned Au thin film confirm that the ZnO NWs grow only in the Au-coated areas. The diameters of these wires range from 20 to 150 nm, whereas more than 95% of them have diameters of 70 to 100 nm. The diameter dispersity is due to the inhomogeneous sizes of the Au nanocluster catalysts when the substrate is annealed during the growth process. The lengths of these NWs can be varied between 2 and 10 μm by adjusting the growth time. The capability of patterned nanowire growth allows fabricating nanoscale light emitters on the substrate in a controllable fashion.

Photoluminescence (PL) spectra of NWs were measured with a He-Cd laser (325 nm) as an excitation source. Strong near band gap edge emission at ~377 nm has been observed. In order to explore the possible stimulated emission from these oriented NWs, the power-dependent emission has been examined. The samples were optically pumped by the fourth harmonic of Nd: yttrium-aluminum-garnet laser (266 nm, 3 ns pulse width) at RT. The pump beam was focused on nanowires at an incidence angle 10° to the symmetric axis of the nanowire. Light emission was collected in the direction normal to the end surface plane of the NWs. In the absence of any fabricated mirrors, Yang peidong et al observed lasing action in these ZnO NWs during the evolution of the emission spectra with increasing pump power as shown in Fig 1.6 (A). [10] At low excitation intensity, the spectrum consists of a single broad spontaneous emission peak with a full width at half maximum of ~17 nm. This spontaneous emission is 140 meV below the band gap (3.37 eV) and is generally ascribed to the recombination of excitons through an exciton- exciton collision process, where one of the excitons radiatively recombines to generate a photon. As the pump power increases, the emission peak narrows because of the preferential amplification of frequencies close to the maximum of the gain spectrum. When the excitation intensity exceeds a threshold (~ 40 kW/cm^2), sharp peaks emerge in the emission spectra. The linewidths of these peaks are <0.3 nm, which are >50 times smaller than the linewidth of the spontaneous emission peak below the threshold. Above the threshold, the integrated emission intensity increases rapidly with the pump power (Fig 1.6 B). The narrow linewidth and the rapid increase of emission intensity indicate that stimulated emission takes place in these NWs. The observed single or multiple sharp peaks represent different lasing modes at wavelengths between 370 and 400 nm. The lasing threshold is quite low in comparison with previously reported values for random lasing (~300 kW/cm^2) in disordered particles or thin films. These short-wavelength

NW nanolasers operate at RT, and the area density of these nanolasers readily reaches $1.1\times10^{10}/cm^2$. They considered that end planes would be excellent mirrors for the resonant cavity as shown in Fig 1.6 C.

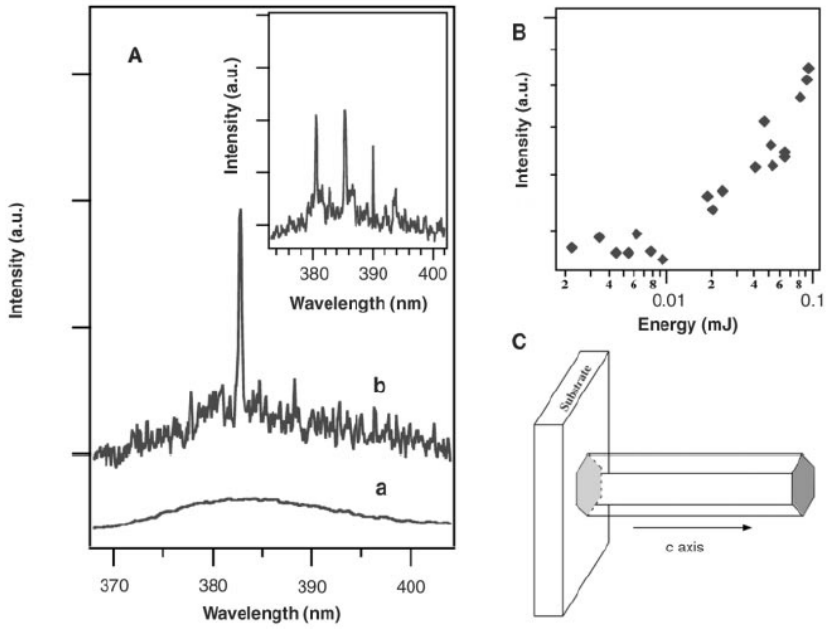

Fig 1.6 (A) Emission spectra from NW arrays below (line a) and above (line b and inset) the lasing threshold. The pump power for these spectra are 20, 100, and 150 kW/cm^2, respectively. (B) Integrated emission intensity from NWs as a function of optical pumping energy intensity. (C) Schematic illustration of a NW as a resonance cavity with two naturally faceted hexagonal end faces acting as reflecting mirrors.

Currently there are many reports related to optically pumped ZnO UV lasers, however, there may have a long time to wait for the commercial applications of ZnO based lasers. Realization of low threshold with direction controlled optically pumped ZnO lasers are our research objects.

1.3.2 Electrically Pumped ZnO UV lasers

Based on the work of the optically pumped ZnO lasers, researchers try to realize electrically pumped ZnO UV lasers, in the year 2006, Yu Siu Fung et al published an article entitled "UV Random Lasing Action in p-SiC(4H)/i-ZnO–SiO_2 Nanocomposite/n-ZnO:Al Heterojunction Diodes " in Advanced Materials, [11] during the years 2007-2008, Yang Deren and Liu Jianlin et al published in Applied Physics Letters related to electrically pumped ZnO UV laser diodes, [12,13] during the years 2009-2010, Shan Chongxin et al in our laboratory have published article "Ultra-low

threshold laser realized in ZnO" in Advanced Materials. [14,15]

In the year 2004, Yu Siu Fung et al used the sol-gel method to prepare ZnO-SiO_2 composite waveguide ultraviolet laser. [16] The proposed ZnO-SiO_2 composite waveguide ultraviolet laser is shown in Fig 1.7. A SiO_2 buffer layer (of refractive Index 1.45) is inserted between the composite film (of effective refractive index varying between 1.5 and 1.9, depending on the concentration of ZnO powder) and Si substrate so that transverse optical confinement can be achieved in the composite film with minimal absorption loss. Hence, light can only be scattered in a direction parallel to the surface of the composite films (such as two-dimensional light confinement).

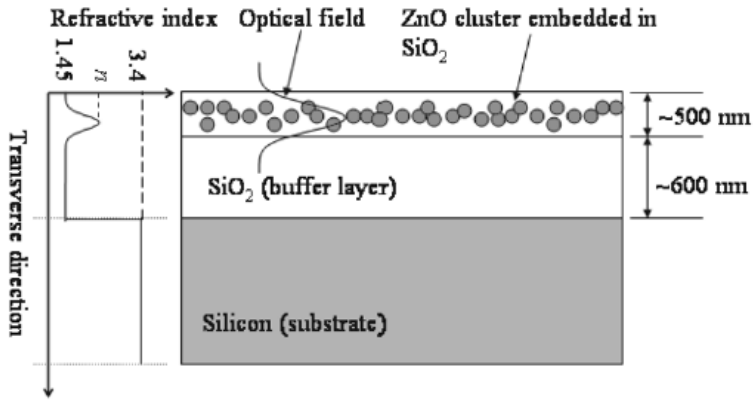

Fig 1.7 Schematic of a ZnO–SiO_2 composite waveguide laser.

The optical characteristics of ZnO–SiO_2 composite waveguide lasers at room temperature were studied under optical excitation by a frequency-tripled Nd :YAG laser (355 nm) at pulsed operation (6 ns, 10 Hz). Fig 1.8 (a) shows the emission spectra of the ZnO: SiO_2 with molar ratio of 1:20 under different pump intensity. Fig 1.8 (b) shows the emission spectra with molar ratio of 1:30 under different pump intensity. [16] The stimulated emission above threshold has been obtained in two cases, but the threshold is different.

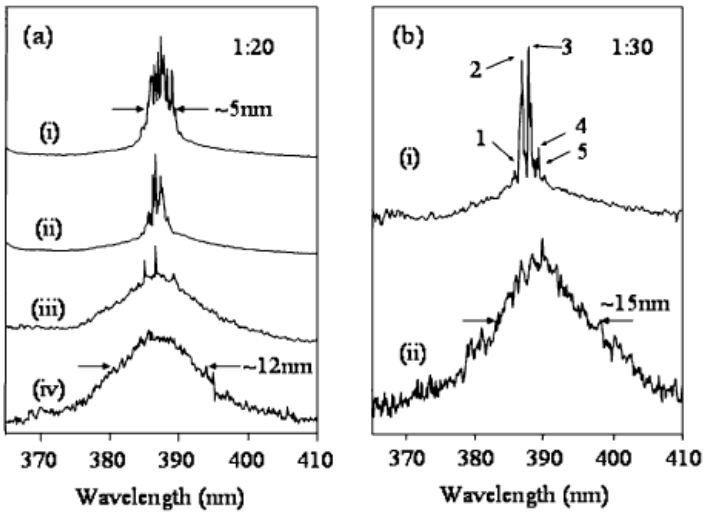

Fig 1.8 Emission spectra of samples with molar ratio (a) 1 : 20 with pump intensities (i) 2.2 MW/cm^2 , (ii) 1.48 MW/cm^2, (iii) 0.62 MW/cm^2, and (iv) 0.26 MW/cm^2, and (b) 1 : 30 with pump intensities (i) 2.2 MW/cm^2 and (ii) 1.48 MW/cm^2.

Their experimental results indicate that RT random laser action with coherent feedback is realized in ZnO–SiO_2 composite waveguidelasers prepared by the sol–gel technique. [16] The proposed waveguide lasers provide two-dimensional confinement of light inside the ZnO–SiO_2 composite films. In addition, the formation of different spacing of parallel-stripe pattern of ZnO clusters, which can be controlled by selecting the desired concentration of ZnO clusters, further enhanced the possibility of realizing closed loop paths of light along the surface of the composite films. Hence, coherent random lasing can be found in waveguide lasers even at low concentration of ZnO clusters. More importantly, they have demonstrated that lasing characteristics of random cavity lasers can be controlled and this will contribute to the future development of random lasers for practical applications. In the year 2006, Yu Siu Fung et al began to realize electrically pumped laser diode based on the structure mentioned above. [11] 4H-SiC substrate is used as the hole-injection layer, Al doped ZnO is used as electrons injecting layer. An intrinsic layer, which consists of ZnO powder embedded in a SiO_2 matrix, is inserted between the n- and p-injection layers to form the p–i–n junction diode shown in Fig 1.9. The intrinsic layer is prepared by the sol–gel technique so that clusters of ZnO powder with a stripe pattern can be formed. The thickness of the SiO_2 matrix is selected to be 60–100 nm so as to optimize the series resistance across the p–i–n junction and to direct the injected electrons and holes into the ZnO powder.

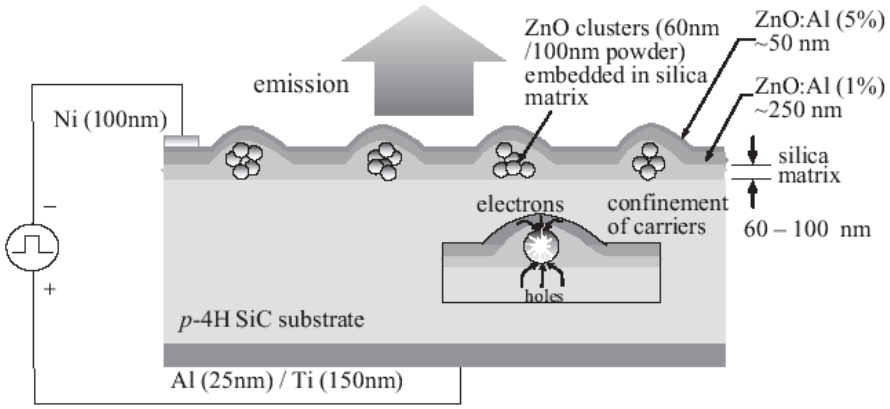

Fig 1.9 Schematic of the p-SiC (4H)/i-ZnO–SiO_2 nanocomposite/n-ZnO: Al heterojunction diode structure.

Fig 1.10 shows the electroluminescence spectra of the p-i-n diode fabricated using ZnO powder of 100 nm and 60 nm by Yu Siu Fung. [11]

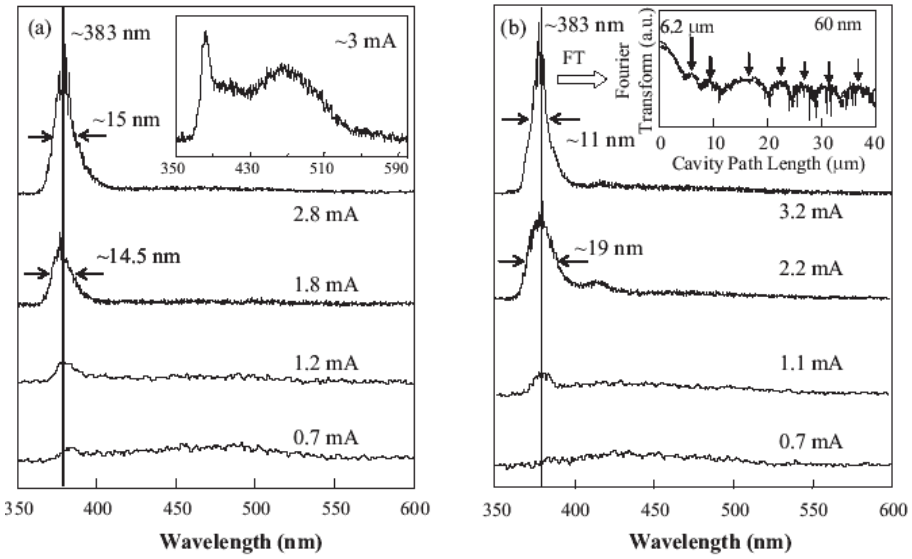

Fig 1.10 EL spectra of the p–i–n diode with (a) 100 nm and (b) 60 nm ZnO powder. The inset of (a) shows the EL emission obtained near the center of the diode at an injection current of 3 mA. The Fourier transform spectrum of the EL emission of the diode with the 60 nm ZnO powder diodes exhibit random lasing under biased at 3.2 mA is shown in the inset of (b).

The narrowing of the emission spectra and the appearance of the sharp peaks confirme the existence of the random laser behavior inside the laser diode, and the peaks located at around 383 nm. The UV emission of the laser diodes originates from

the ZnO–SiO_2 nanocomposite layer, and the use of ZnO powder can improve the electrical to optical conversion efficiency of the heterojunction. In addition, the patterned ZnO clusters in the SiO_2 matrix enhance the quality of random media so that the random lasing action can be sustained.

Due to design and fabrication techniques for electrically pumped lasers are much more complicated than those for optically pumped lasers. However, considering the factors such as convience of transport, many researchers have devoted their interests to the electrically pumped ZnO lasers. Currently there are just some initial exploring researches for the electrically pumped ZnO lasers, and further research is needed.

1.3.3 ZnO Based LEDs

The research on the ZnO-based LEDs is still a hot spot in the photoelectric field at present. For the research of ZnO pn homojunctions, if p type doping problems were resolved, the UV-blue LEDs with low threshold voltage at room temperature would be realized based on ZnO. This kind of ZnO LEDs would have high stability and long life at room temperature. In the year 2005, Kawasaki et al in Northeastern University, Institute of materials reported "Repeated temperature modulation epitaxy for p-type doping and light-emitting diode based on ZnO" in Nature materials, [17] Fig 1.11 a shows the schematic diagram of the LED, the $ScAlMgO_4$ (SCAM) substrate owning good lattice matching with ZnO was explored, growth quality problem was well solved. At the same time N element was doped at low temperature of 450 °C and annealing process was explored to eliminate non-equilibrium defects such as the introduced donor hydrogen at 900°C. Thus the thicker and repeatable p-type ZnO can be obtained by repeating this growth process. Obviously, the foundation is to grow high quality ZnO during this approach, ZnO should be doped and treated based on this foundation, the purpose of fabricating p-type ZnO thin film can be realized. The ZnO p-i-n homojunction LED can be fabricated. Very good rectifying behavior displays the threshold voltage is about 7 V as shown in Fig 1.11 b. The fabricated p-i-n ZnO homojunction shows excellent rectification characteristic. Meanwhile, the emission peaks are composed of the ultraviolet and visible light applying positive bias.

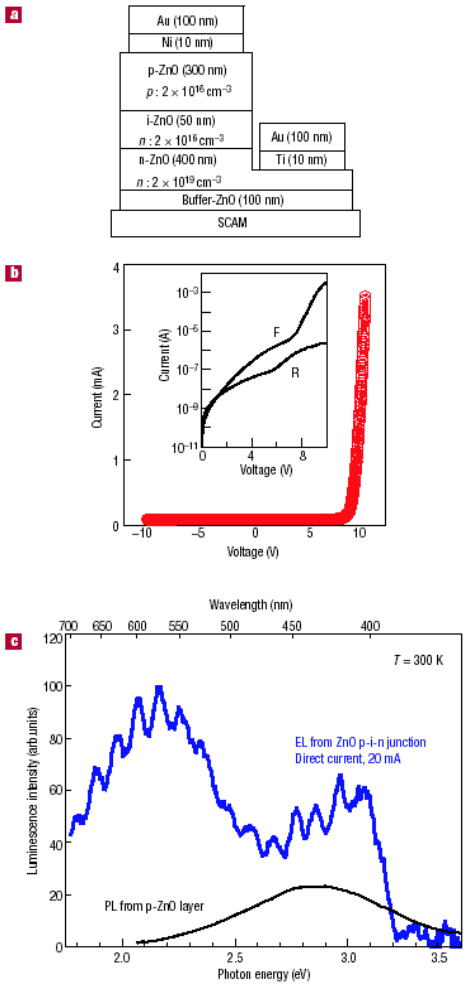

Fig 1.11 a, The structure of a typical p–i–n junction LED. b, Current–voltage characteristics of a p–i–n junction. c, Electroluminescence spectrum from the p–i–n junction (blue) and photoluminescence (PL) spectrum of a p-type ZnO film measured at 300 K.

In January 2006, ZnO homojunction LED were successfully fabricated on sapphire substrate using MBE in our laboratory by Lu Y M et al for the first time, the corresponding article was published in Applied Physics Letters. [18,19] High optical quality p-type ZnO with resistivity of 55 Ω cm, carrier concentration of 2.3×10^{17} cm^{-3}, mobility of 0.50 $cm^2V^{-1}s^{-1}$ were fabricated on sapphire substrate choosing the appropriate growth conditions. ZnO pn homojunction was prepared using non-doped n-type ZnO, Ni-Au electrode was used for the p-type layer, and In electrode for n-type layer. At low temperature (11-200 K) electroluminescence (EL) was obtained. This is the first time that the EL of ZnO pn homojunction on the sapphire substrate was

obtained internationally. Compared with the results of Tohoku University in Japan, the preparation process was simplified without using the expensive SCAM substrate at the same time.

In the same year, Park Seong-Ju et al published an article "UV Electroluminescence Emission from ZnO Light-Emitting Diodes Grown by High-Temperature Radiofrequency Sputtering"in Advanced Materials. [20] ZnO homojunction was prepared by Metal Organic Chemical Vapour deposition and EL was also obtained by Ye Z Z et al. [21] However, due to poor stability of p-type ZnO and difficulties of preparation, researchers use heterostructure to achieve the ZnO-based LED, Gu SL et al used p-Si for fabricating n-ZnO/p-Si heterojunction, and obtained EL. [22] DC Look et al prepared n-ZnO/p-GaN heterojunction and EL peak located at 430nm was obtained, [23] in the present there are many reports on the ZnO/GaN LEDs, [24,25] many reports combined with nano-ZnO LED structure could also be found out. [26,27]

In the year 2007, Myoung Jae-Min et al reported "ZnO-Nanowire-Inserted GaN/ZnO Heterojunction Light-Emitting Diodes". [26] Fig 1.12 a shows SEM and schematic diagram of ZnO NW inserted heterojunction LED device. The Mg-doped GaN film with a thickness of 0.6 mm were epitaxially grown on GaN (0002) template by MBE. ZnO NWs (32 nm in diameter and 600 nm in length) were subsequently fabricated on the Mg-doped GaN film by metal-organic chemical vapor deposition (MOCVD) to form nanosized GaN/ZnO heterojunctions. The nanosized heterojunctions were expected to have good interfacial contacts because the nanosized contact area and the small lattice mismatch of 1.9% between GaN and ZnO led to epitaxial growth of the ZnO NWs on the Mg-doped GaN film. The Mg-doped GaN film exhibited p-type conductivity with a hole concentration of 1.2×10^{18} cm^{-3} and hole mobility of 15 $cm^2V^{-1}s^{-1}$. 0.4 μm thick Al-doped ZnO film with the high electron concentration of 9.7×10^{18} cm^{-3} and an electron mobility of 6.9 $cm^2V^{-1}s^{-1}$ was fabricated on the ZnO nanowire arrays by radio frequency (RF) magnetron sputtering. The Al-doped ZnO film could supply electrons into the heterojunction for radiative recombination and the metal electrodes could be fabricated on the ZnO film without complicated processes. The inset of Fig 1.12 (a) shows photo-image of blue light emission of the LED, Fig 1.12 (b) shows the schematic diagram of the LED.

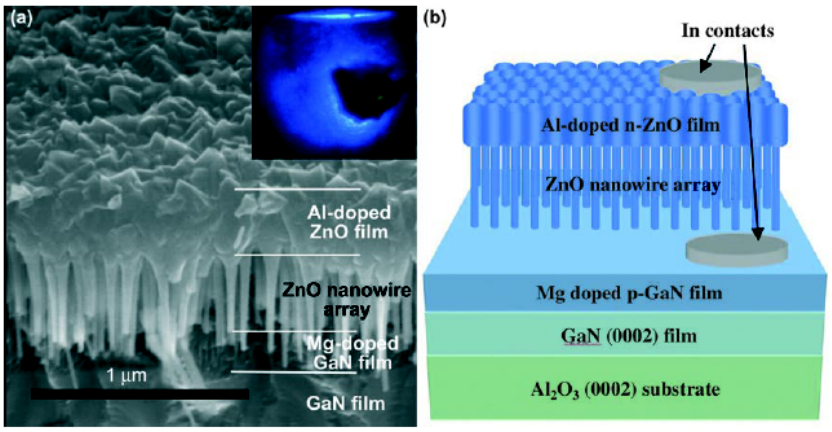

Fig 1.12 (a) A 45°-tilted SEM image and (b) schematic illustration of the Mg-doped GaN film/ZnO NW array/Al-doped ZnO film structures for nanometer-sized GaN/ZnO heterojunction diode, the inset is a photograph of blue-light emission from the heterojunction diodes observed through a microscope at the forward current of 10mA.

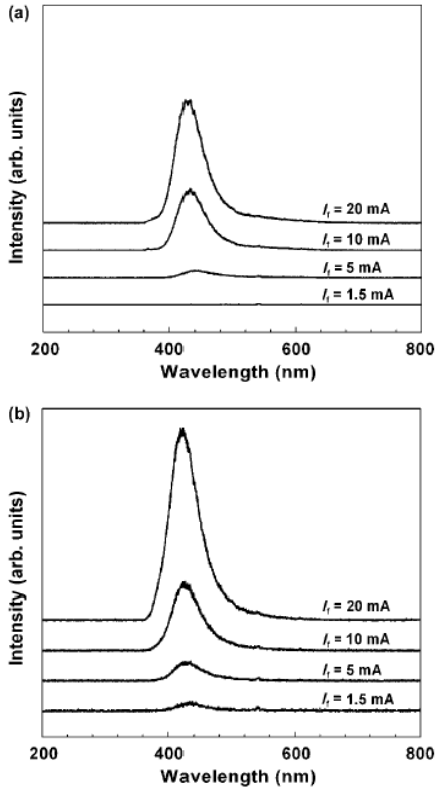

Fig 1.13 EL spectra of (a) film-based GaN/ZnO heterojunction diodes and (b) ZnO NW inserted GaN/ZnO heterojunction diodes.

As shown in Fig 1.13, [26] heterojunction diode based on thin film shows a broad blue emission peak, the intensity of blue emission located at 440 nm increased with forward current of 20 mA and blue-shifted to 425 nm. The EL emission enhanced through inserting NWs. The emission wavelength was located at 432 nm under forward current of 1.5 mA, and blue-shifted to 421 nm under injection current of 20 mA.

Their experimental results illustrate that the EL emission for the heterojunction inserted with NWs has been improved compared with thin film based heterojunction, this is due to the better interface could be formed for the nano-heterojunction and the interface defects is less.

Currently the main problem for the ZnO based LED is p type doping, and p type doping should be built on the high quality ZnO. Due to the lattice mismatch, interface defects for the heterojunction LEDs, the research on how to fabricate heterojunction LED with ideal interface should be further carried out. In the future research area, realization of miniaturation should be based on fabricating minitype-junction such as single NW homojunction or heterojunction owning ideal interface, it also means the birth of NW based LED with high efficiency.

1.3.4 ZnO Based Photodetectors

There are many reports related to the ZnO based photodedetectors (PDs). The main research is focused on ZnMgO PDs in the wavelength range of solar blind (220-280 nm), the photon detection can be realized in the range from ZnO (band gap 3.37 eV) to MgO (7.6 eV) (380-170 nm) through adjusting the Mg component in ZnMgO, its main problem is phase transition, the purpose is to realize fast response for the weak signals. ZnO nanostructures own larger surface to volume ratio, the realization of the PDs with high gain using the characteristic of the electrons inside ZnO can be bounded by adsorbed negative oxygen ions. So ZnO nanostructures based PDs also attracted much interest of the researchers. For the ZnO based PDs, in the year 2001 Lu Y et al reported ZnO Schottky UV PDs. [28] In the year 2006, Thong J T L et al reported on the ultrafast response of ZnO NWs PD. [29] C. Soci et al in 2007 found that very high optical gain can be obtained in ZnO NW PD, [30] the corresponding results were published in Nano Letters. In the year 2008, Greenham Neil C et al fabricated UV PD based on ZnO nanoparticles, and their results were also published in Nano Letters. [31]

The most interesting article is related to ZnO nanostructures based PD with high

gain: C. Soci et al prepared ZnO NW using chemical vapor deposition method, the NW was transferred on oxidezed Si substrate, and the Ti-Au intedigital electrodes were prepared by photolithography method, the schematic diagram for the device is shown in the inset of Fig 1.14. [30] The results of photocurrent measurements performed on single NW devices in standard ambient conditions are summarized in Fig 1.14. Fig 1.14 a shows some typical *I-V* characteristics of the ZnO NWs in dark and under UV illumination (λ) 390 nm) at various light intensities; the *I-V* curves are linear around zero applied bias, which indicates good ohmic behavior of the Ti/Au contacts. The linear increase of the current with applied bias (V) is due to the increase of the carrier drift velocity, hence the reduction of the transit time

$$T_t = l^2 / \mu V \ , \tag{1-1}$$

where μ is the carrier mobility and l is the separation between the electrodes. The current measured in the NW increases significantly under illumination. By varying the light intensity from 6.3 μ W/cm^2 to 40 mW/cm^2, the current increases from 2 to 5 orders of magnitude, as seen in Fig 1.14 b.

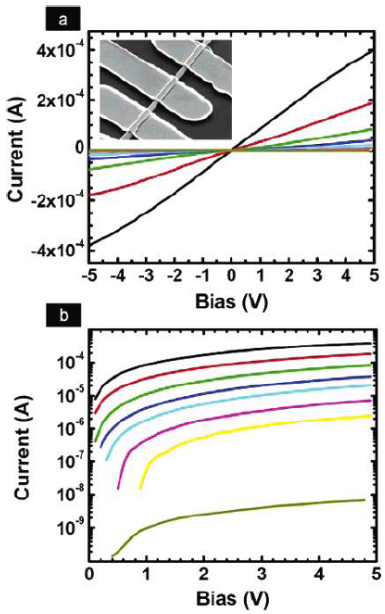

Fig 1.14 (a) *I-V* characteristics of a single-NW PD as a function of light intensity, inset is the SEM image of a typical ZnO NW device (b) the *I-V* curves presented on a natural logarithmic scale.

Because of high surface to volume ratio, traping at surface states drastifically affects the transport and photoconduction properties of NWs. Fig 1.15 shows

schematic of the photoconduction mechanism in the presence of high density of hole trap states at the NW surface: [30]

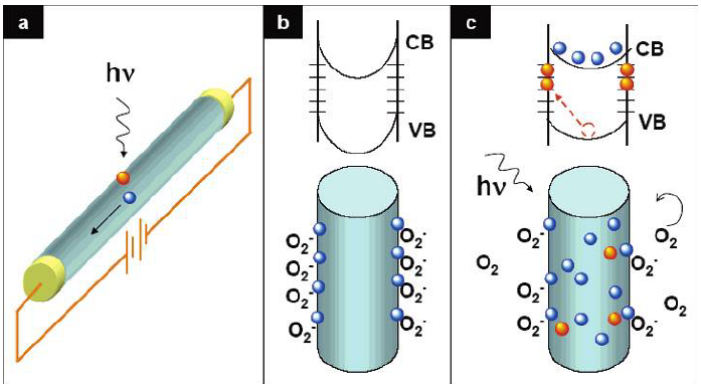

Fig 1.15 (a) Schematic of a NW photoconductor, (b and c) Trapping and photoconduction mechanism in ZnO NWs in dark and under UV illuminescence, respectively.

Upon illumination with photon energy larger than the semiconductor band gap, electron-hole pairs are photogenerated and holes are readily trapped at the surface, leaving behind unpaired electrons, which increase the conductivity under an applied electric field (Fig 1.15 a). Schematics of the NW energy band diagrams in dark and under illumination are displayed in Fig 1.15 (b, c), respectively, illustrating the charge separation process of photogenerated electrons and holes under the intrinsic NW electric field and the occupation of surface states by photogenerated holes. In ZnO, it has been previously shown that the following trapping mechanism is governing the photoconduction in thin films and NWs: [32-37] in the dark (Fig 1.15 b), oxygen molecules are adsorbed on the oxide surface and capture the free electrons present in the n-type oxide semiconductor

$$\left[O_2(gas) + e^- \rightarrow O^{2-}(ad)\right] \tag{1-2}$$

and a low-conductivity depletion layer is formed near the surface. Upon illumination at photon energy above band gap (Fig 1.14 c), electron-hole pairs are photogenerated:

$$\left[h\nu \rightarrow e^- + h^+\right] \tag{1-3}$$

holes migrate to the surface along the potential slope produced by band bending and discharge the negatively charged adsorbed oxygen ions:

$$\left[h^+ + O^{2-}(ad) \rightarrow O_2(gas)\right] \tag{1-4}$$

and consequently, oxygen is photodesorbed from the surface. The unpaired electrons

are either collected at the anode or recombine with holes generated when oxygen molecules are readsorbed and ionized at the surface. This hole-trapping mechanism through oxygen adsorption and desorption in ZnO NWs augments the high density of trap states usually found in NWs due to the dangling bonds at the surface and thus enhances the NW photoresponse. It is well-known that photoconductors with blocking contacts, such as a Schottky barrier at the metal electrode-semiconductor interface, can exhibit hole-trapping in the reversed-bias junction that shrinks the depletion region and allows tunneling of additional electrons into the photoconductor; if electrons pass multiple times, this mechanism yields photoconductive gain greater than unity. [38]

Currently there are not so many reports related ZnMgO nanostructures based PD, if the ZnMgO with band gap adjustable can be combined with the chracteristics of nanostructures, we believe that miniaturized solar blind PDs will be realized.

1.3.5 ZnO Generators

Can ZnO be used for fabricating generators? The answer is yes. Can it be used for fabricating minaturized generators? The response still is yes. During the years 2004-2008, Wang Zhonglin et al have published articles on ZnO based nano-generator in the journals such as Nano Letters and Science. [39-42] The efficiency of the NW-based piezoelectric (PZ) power generator is estimated to be 17 to 30%. Their research is based on aligned ZnO NWs grown on *c* plane-oriented α-Al_2O_3 substrate using Au particles as catalysts by vapor liquid solid process. An epitaxial relation between ZnO and α-Al2O3 allows a thin, continuous layer of ZnO to form at the substrate surface, which serves as a large electrode connecting the NWs with a metal electrode for transport measurement (Fig 1.16 A). [40] The NW grows along the (0001) direction (Fig 1.16 B). Most of the Au particles at the tips of the NWs either evaporate during the growth or fall off during scanning by AFM tip. So for the most of the NWs the growth front is free of Au particles or has a small hemispherical Au particle that covers only a fraction of the top. For pourpose of the measurement they have grown NWs arrays that have relatively less density and shorter length (0.2 μm to 0.5 μm), so that AFM tip can exclusively reach on NW without touching another.

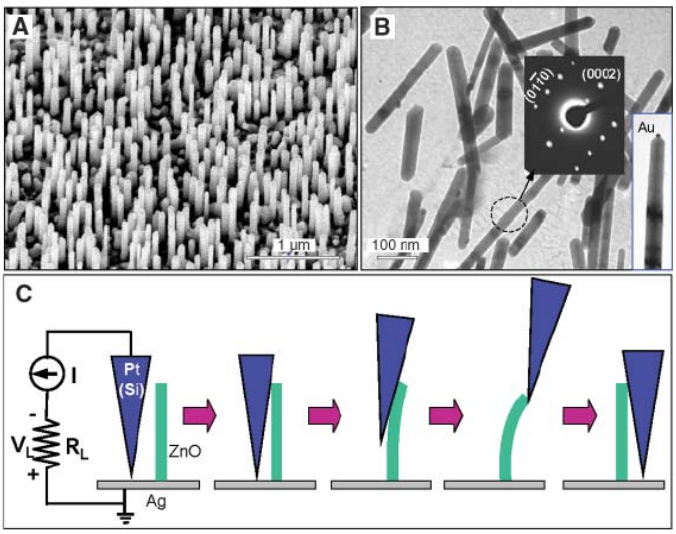

Fig 1.16 Experimental design for converting nanoscale mechanical energy into electrical energy by a vertical PZ ZnO NW. (A) SEM images of aligned ZnO NWs grown on a-Al_2O_3 substrate. (B) TEM images of ZnO NWs. Inset at center: an electron diffraction pattern from a NW. Most of the NWs had no Au particle at the top. Inset at right: image of a NW with an Au particle. (C) Experimental setup and procedures for generating electricity by deforming a PZ NW with a conductive AFM tip.

Experimentally, both the topography (Fig 1.17 A) and the corresponding output voltage images across were recorded simultaneously when the AFM tip was scanned over the aligned NW arrays. [40] In the voltage output image, many sharp output peaks were observed. Most of the voltage peaks are ~6 to 9 mV in height. The average density of NWs whose voltage output events had been captured by the tip in Fig 1.17 B is ~8/μm^2, thus ~40% of the NWs were contacted. The location of the voltage peak is directly registered at the site of the NW. A time series of the voltage output line profiles across one NW acquired at a time interval of 1 min is shown in Fig 1.17 C. Because the dwell time for each data point is 2 ms, which is longer than the average lifetime of the voltage peak of 0.6 ms (Fig 1.17 D). The shape of the discharge peak can be further improved and analyzed by maximizing the tip scanning frequency and reducing the scanning range. Fig 1.17 E is a line profile of voltage output when the tip was scanned over a single NW at a scanning velocity of 12 μm/s. The FWHM of the voltage peak was estimated to be t ~ 0.6 ms.

The physical principle for creating the PZ discharge energy arises from how the piezoelectric and semiconducting properties of ZnO are coupled. For a vertical, straight ZnO NW the deflection of the NW by an AFM tip creates a strain field, with the outer surface being stretched (positive strain ε) and the inner surface compressed

(negative ε). An electric field E_z along the NW (z direction) is then created inside the NW volume through the PZ effect,

$$E_Z = \varepsilon_Z / d \tag{1-5}$$

where d is the PZ coefficient along the NW direction that is normally the positive c axis of ZnO, with the Zn atomic layer being the front-terminating layer. [43] The PZ field direction is closely parallel to the z axis (NW direction) at the outer surface and antiparallel to the z axis at the inner surface. Under the first-order approximation, across the width of the NW at the top end, the electric potential distribution from the compressed to the stretched side surface is approximately between V_s^- to V_s^+ [with

$$V_s^{\mu} = \mu 3T\left|y_m\right| / 4Ld \text{ , [44]} \tag{1-6}$$

where T is the thickness of the NW, L is the length for the NW, y_m is the maximum deflection for the NW]. The electrode at the base of the NW is grounded, V_s^- and V_s^+ are the voltages produced by the PZ effect, the potential is created by the relative displacement of Zn^{2+} cations with respect to the O^{2-} anions, a result of PZ effect in wurtzite crystal structure, thus, these ionic charges can not freely move and recombine without releasing the strain, the potential difference is maintained as long as the deformation is in place.

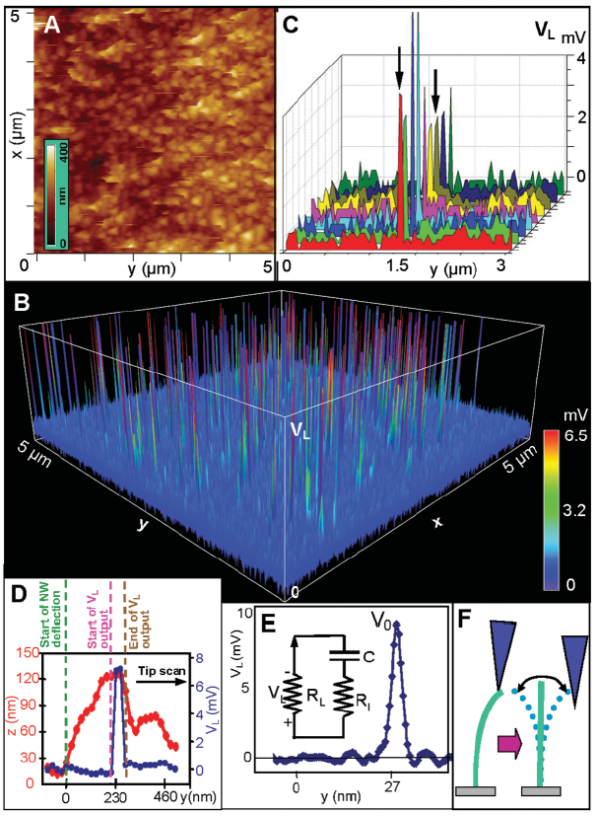

Fig 1.17 Electromechanically coupled discharging process of aligned PZ ZnO NWs observed in contact mode. (A) Topography image and (B) corresponding output voltage image of the NW arrays. (C) A series of line profiles of the voltage output signal when the AFM tip scanned across a vertical NW at a time interval of 1 min. (D) Line profiles from the topography (red) and output voltage (blue) images across a NW. (E) Line profile of the voltage output signal when the AFM tip scans across a vertical NW at about 12 μm/s. (F) the stored elastic energy is transferred mainly into vibrational energy after creating the PZ discharge event.

In the year 2008, Wang et al published an article in Nature nanotechnology entitled "Power generation with laterally packaged piezoelectric fine wires", converting the mechanical energy into electrical energy can be applied in sensing, medical science, defense technology and so on. [42] The power generator is based on clyclic stretching-releasing of a PZ fine wire that is firmly attached to metal electrodes at both ends. Repeatedly stretching and releasing single line with a strain of 0.05% -0.1% creats an oscillating output voltage of up to 50 mV, and the energy conversion efficiency of the wire can be as high as 6.8%.

In the future research areas, we can imagine that ZnO nano-generators could be transfered inside the body to supply power for some micro-mechanic devices while curing such as tumor disease. It is known that surgeries can be easily treated by

human being outside, but there are many difficulties for curing some organ diseases inside, not only the patients will suffer much pain, but also such diseaes are difficult to be treated by doctors. Hence, in the future medical development, if the 'surgery doctors' could be miniaturized, and they would be sent to the location for curing the dieseases, it is possible that ZnO nano-generators will be needed.

1.4 Conclusion

Through summary of the literatures related to ZnO mentioned above, it is observed that ZnO materials will have potential prospects and applications in the photoelectric devices, however, realizing low threshold with direction controlled optically pumped ZnO based lasers need further research ; considering the ZnO p type doping problems electrically pumped lasers uasually are fabricated based on other materials, not only the carrier injection problem should be considered, but also the cavity design should be considered, so there are only some initial research; there are also problems for the ZnO based UV-blue LEDs due to p type doping, so there are still some challenges exist for the realization of low threshold ZnO LEDs with high efficiency and stability at RT. However, the prospects are still bright. Although there are many reports related to ZnO nanostructure based PDs, there are not so many reports related to ZnMgO with component adjustable nanostructure based PDs; Zhonglin Wang et al scientists have obtained excellent results from the ZnO nano-generators. Because of these early researches, may be much more peculiar properties of the ZnO nanostructures are waiting for researchers to dig, so a majority of the researchers set off a study on the ZnO nanostructures, at the same time the researchers in our lab have devoted their interests in the research of ZnO material.

Chapter 2 Preparation and General Characterization Methods for ZnO Material

2.1 Preparation of ZnO material

So as to explore the properties of ZnO for applications, firstly we should know how to prepare ZnO material. There are a variety of methods for preparing ZnO material. For the preparation methods of ZnO thin films there are: pulsed laser deposition (PLD), molecular beam epitaxy (MBE), magnetron sputtering, metal-organic chemical vapor deposition (MOCVD). For the preparation methods of ZnO nano-material there are: Chemical vapor deposition (CVD), hydrothermal method, electrochemistry and template assisted method.

2.1.1 Pulsed Laser Deposition

Pulsed Laser Deposition which is also called pulsed laser ablation (PLA), is a kind of way using laser to evaporate materials from a target in order to form a thin film on a substrate. During pulsed laser deposition, photons are absorbed by a high purity ZnO target which is heated by the pulse laser leading to the evaporation. The evaporated material which runs into the plasma tube that is perpendicular to the ZnO target, and is deposited on the substrate. As reported in the article of R P H Chang et al [45], high quality ZnO film was grown using improved PLD method. Due to the presence of the plasma, ionized atoms and molecules on the substrate surface interacting with the ZnO film will reduce the quality of the film, so it is difficult to obtain smooth ZnO film with homogenous thickness by PLD, and the film quality is difficult to be further improved.

2.1.2 Molecular Beam Epitaxy

In an ultra-high vacuum chamber, the molecular beam is produced by heating the material using either heator by Joule effect or by electron beam method. The incident atomic or molecular beam is directed on the substrate. Surface adsorption, re-evaporation, diffusion and nucleation mechanisms lead to the formation of film.

MBE is a technology generated for growing high-quality crystalline thin film on a crystalline substrate. The advantages of this technique: the substrate temperature is low, the growth speed of film can be slowly, the beam intensity can be exactly controlled, and the component and doping concentration can be adjusted rapidly according to the changes of the sources. The technology can be used to prepare single crystal thin film with tens of atomic layers and ultra thin layered quantum well micro-structure with alternative growth of different composition or different doped thin layers. There are two kind of methods using MBE to grow high quality ZnO thin film: one is laser assisted MBE (L-MBE) [46] using the KrF laser to ablate ZnO target with purity of 99.999%, ZnO film can be grown on (0001) sapphire substrate with oxygen partial pressure of about 1×10^{-4} Pa, the growth temperature of 500 ℃; the other is plasma-assisted MBE (P-MBE), [47] the typical growth conditions are: sapphire substrates, oxygen radio frequency (rf) plasma source and Zn solid source. However, it takes much more fees using MBE method to prepare thin film.

By the way, the ZnO ceramic target is always used as the source to prepare ZnO thin film using electron beam evaporation equipment, [48] the vacuum in the chamber is generally 10^{-5} Torr during evaporation process, the electron beam current can arrive at 40 mA, the evaporation rate can reach 20 nm/min.

2.1.3 Magnetron Sputtering

For this preparation method electric field induced between a target and a substrate can ionize the gas introduced in the chamber. The collisions between the ions contained in the plasma and the target allow the sputtering of the target. Atomic and moleculars reach the substrate to form a thin layer. Magnetron sputtering is a method of high-speed deposition under low-pressure when the gas ionization rate is effectively improved. Through introducing magnetic field around the target cathode surface the electrons are trapped close to the target, the helicoidal paths of the electrons creat more ionizing collisions in the gas, so the plasma density can be increased, and the sputtering rate can be further increased. In some cases reactive sputtering is needed. In this case a second gas is introduced into the chamber, the composition of the film can be controlled by the pressure of the reactive gas, this is often for nitride or oxide films. Metal Zn or ceramic ZnO target can be used in the process of preparing ZnO in low-pressure environment through introducing Ar and oxygen mixture gases using direct current source or RF sputtering, [49] the substrate temperature can be adjusted from RT to 700 °C, and the sputtering pressure is

generally about 1 Pa.

2.1.4 Metal-organic Chemical Vapor Deposition

MOCVD is the abbreviation of metal-organic chemical vapor deposition. The source materials are often composed by organometallic compounds of Ⅲ, Ⅱ group elements and hydride of Ⅴ, Ⅵ group elements. The vapor phase epitaxy is performed on a substrate by thermal decomposition method, various Ⅲ-Ⅴ, Ⅱ-Ⅵ semiconductors and their diverse solid solution of thin layered materials can be prepared. Usually the crystal growth in the MOCVD system is under atmospheric pressure or low pressure (10-100 Torr) by introducing H_2 into the reaction chamber. The substrate temperature can up to 1200 ℃, the graphite base is heated by radio frequency induction (substrate above the graphite base). Metal organic sources is brought to growth area by a carrier gas H_2 passing through temperature controlled metalorganic liquid. The gas phase reaction can occur at room temperature. The production of ZnO particles reduces the quality of the grown film, so the key to grow high quality ZnO thin film is to limit the vapor phase reaction.

The Methods described above are often used for the growth of ZnO thin film. The following methods are often used for preparing ZnO nanostructures:

2.1.5 Chemical Vapor Deposition

Vapor transport is a simple method used for growing nanostructures. The growth principle follows these steps: solid sources which vaporize under conditions of specific temperature and pressure, and transport to substrate surface by a carrier gas flow for nucleation and growth. Vapor liquid solide (VLS) growth method is the most widely used method for preparing semiconductor nanowires. This method was firstly proposed by Wagner in the twentieth century and sixties for the growth of whiskers. [50] The method is a mature approach commonly used for the preparation of ZnO. [51-54] Theoretically, it is appropriate for growing ZnO using Au and Fe as the catalysts. Actually the Au catalyst is usually used. In the process of preparing ZnO nanostructures, a mixture of graphite and ZnO powder source is commonly used for growth, growth temperature is generally above 900 °C. In addition to VLS growth, another typical growth method of nano-material is vapor solide (VS) growth. This method can be used for preparing ZnO nanostructures using source material such as Zn metal, the lower growth temperature can be used at about 500-600 centigrade. [55]

2.1.6 Hydrothermal Method

This method is simple and has been widely used to prepare ZnO and other semiconductor nanowires and nanorods. [56-58] But for preparing multi-component nanowires using this method there are still some problems related to product quality and single-crystal dispersion. For the growth of ZnO nanowires, the sublayers such as GaN template or ZnO seed layer are generally used, hexamethylenetetramine and zinc salts such as zinc acetate are used as source materials, the reaction temperature are maintained at about 90 °C. Through our hydrothermal experiments, it is found out that reproducibility is much high and the growth process is stable using this method.

2.1.7 Electrochemistry

Electrochemical reaction is performed assisted with the electric field between electrodes, the electric field is the principal motor for the migration of the ions. In the year 1996, French Paulon and Lincot [59] and Japanese Izaki and Omi [60] reported the preparation of ZnO films by electrochemical deposition in the journals Adv Mater and Appl Phys Lett, respectively. The difference of preparing ZnO nano-material by electrochemical method from the hydrothermal method is the faster growth rate, but the substrates must be conductive using electrochemistry method.

2.1.8 Template Assisted Method

Template assisted method is a common approach of preparing one dimensional (1D) wires. In this technique template is just a framework of supplying for the material with similar growth morphology. Besides ZnO, [61] this method has been used for preparing a wide range of inorganic nano-materials such as Au, Ag, TiO_2, C nanotubes [62] and organic polymers. However, with this method it is difficult to obtain single crystal material.

2.2 Characterization Methods for ZnO Material

In order to fabricate photoelectric devices using prepared ZnO material, the properties should be characterized. It is easily for ZnO material to form different kinds of nanostructures such as NWs, nanorods, nanotubes and nanorings and so on, so the morphological and structural characterizations are nessary. Through the measurements of optic properties such as photoluminescence (PL), absorption and transmission of the material we can better understand its crystal quality. Then the device can be

fabricated based on the material with better quality for applications. The commonly used methods of characterizing ZnO material are showing as follows:

2.2.1 Scanning Electron Microscope

SEM owning high resolution allows us to observe nano-sized materials. Its main principle is using emmited electrons from the sample to detect or image. SEM can be used to observe surface micro-morphology and composition for solid materials. With its help we know how different kinds of ZnO nanostructures are obtained by adjusting experimental parameters, it is very helpful for analyzing the growth mechanisms. The basic structure of SEM is composed by three major components of electron-optics, vacuum and image signal processing display systems. [63] The main schematic diagram is shown in Fig 2.1. The emitted electrons from the electron gun go through condensed lens and objective lens become a very fine electron beam. The sample is hitted, the secondary electrons (SE) are excited from the sample. The image can be formed through detecting the SE by detector and magnifing the signal processes. Meantime SEM owns the function of measuring the composed elements of sample, thus not only the morphology can be measured by SEM, the composition of material can also be detected if the photons emitted by the sample are considered. Due to the image is formed by SE, thus it is a little difficult to obtain an image with high resolution for certain samples without conductivity.

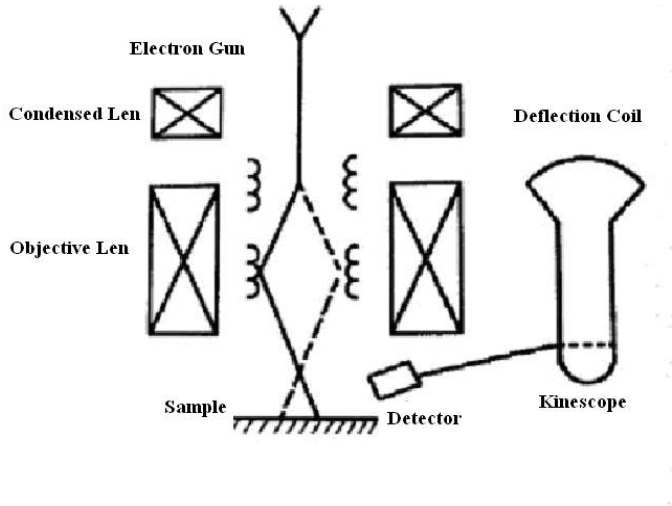

Fig 2.1 Schematic diagram of scanning electron microscope.

2.2.2 Transmission Electron Microscope

TEM owns much more high resolution than SEM. Its main principle is the emitted electrons which coming from the cathode filament are accelerated by anode and focused, then go through sample to image, its resolution can be 0.1 nm at maximum. Thus TEM can be used to detect the defects of the prepared sample in atomic size. Fig 2.2 is a structural diagram of TEM. The theories of electron diffraction in the electron microscope are in accordance with those of X-ray diffraction, which follow the requirement and geometry relationship of the Bragg diffraction equation.

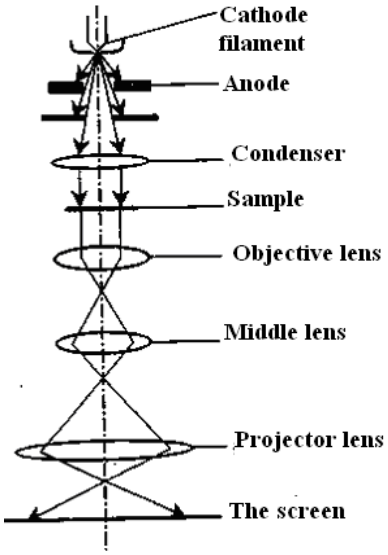

Fig 2.2 The schematic diagram of optical path for transmission electron microscopy.

The diffraction beam is formed by the role of the quasi-parallel incident beam with sample, the diffraction spot is formed by the role of parallel beam through the objective lens. Ultra thin samples are required, samples should be transparent for the electron beam. For the measurement of ZnO material by TEM size of samples should be less than 300 nm (the thinner the sample is, the higher resolution will be, and the formed image will be much more clearly), thus the electrons can pass through the material for the occurence of diffraction, atomic arrangement image can be obtained (some defects within atomic size can be observed through high resolution (HR) TEM, currently for the fabricated ZnO junction devices a key point is to check if the interface is ideal, the quality of the device can be measured by HR-TEM,

experimental parameters can be improved by analyzing HR-TEM results), or the crystal quality for the grown materials can be analyzed by selected area electron diffraction (SAED) (for single crystal sample its electron diffraction illustrates regular point pattern symmetrically arranged; for the polycrystal sample, diffraction of rings pattern is often displayed). Currently ZnO nanostructures with various morphologies can be obtained through changing growth parameters, the growth mechanisms for the nanostructures can be analyzed through TEM measurements, thus experimental program can be better constructed.

2.2.3 X-ray Diffraction (XRD)

The crystal quality of materials can be judged by XRD, the crystal quality can be judged by the FWHM of XRD (the narrower the peak is, the higher the crystal quality will be), the situation of the periodically arranged crystalline rods can be juded by XRD ϕ scan. The growth orientation can be measured by XRD (the X-ray 2θ diffraction results illustrates well alligned ZnO NWs fabricated on sapphire substrate owning only (002) peak besides substrate peak in the range 30-70°, there are many peaks observed for ZnO powder). Shown in Fig 2.3 the incident and reflected optical path (DB + BF) for *b* crystal plane is larger than that for *a* crystal plane, DB = BF =$d\sin\theta$. According to diffraction conditions, the diffraction intensity is only mutually strengthened when the optical path difference is equal to an integer multiple, that is

$$2d\sin\theta = n\lambda \quad \text{(n is a positive integer)} \qquad (2\text{-}1)$$

This is the Bragg diffraction equation, where n is diffraction series, θ is diffraction angle, λ is the wavelength of X-ray, d is interplanar distance. In single crystal, d is the lattice constant.

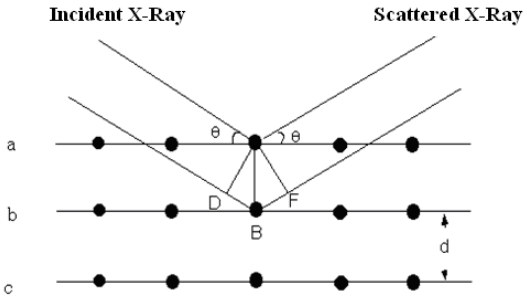

Fig 2.3 the X-ray diffraction of the crystal.

2.2.4 Photoluminescence, Absorption and Transmission

The optic properties of the prepared samples can be measured by PL, ZnO is a kind of photoelectric material, the band gap varies with volume change of nanostructures due to quantum size effects. So for the research of ZnO nanostructures, PL measurement is necessary. Luminescence is a relaxation process from excited state (An excited state is formed through absorption of certain energy by material) to ground state that energy is released in the form of light radiation. Back scattering experimental setup is used for PL measurements. Fig 2.4 shows the experimental setup of the micro-area PL. The experimental temperature of the sample can be adjusted between 77 K (the temperature of liquid nitrogen) and 300 K.

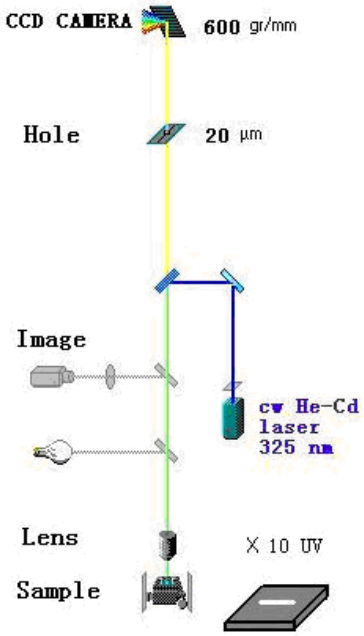

Fig 2.4 the schematic diagram for the micro-area photoluminescence optical path.

PL measurements illustrate the intensity of UV emission is stronger for prepared ZnO material with better crystal quality, the emission peak is located at 3.3 eV at RT, and this peak is attributed to near band edge emission; usually the week defects related emission ranging from 500 to 600 nm is accompanied, which is always a broad band, currently this peak is deduced from interstitial atoms or vacancies. The crystal quality of grown material can be judged by PL measurement.

At the same time, solid materials have properties of light absorption and

transmission. The absorption coefficient changes with photon energy, the information of energy band gap, half-width of band tail state can be obtained through absorption measurement. It is observed that the absorption edge is located at 3.3 eV for ZnO thin film owning better crystal quality through absorption measurement, the corresponding transmission is higher than 90% in the visible light range. So properties of materials can be better understood through absorption and transmission measurements.

2.3 Conclusion

This chapter describes the prepartion and general characterization methods for ZnO thin film and nano material. Characteristics and scope of applications for a variety of methods are analyzed. When these information mentioned above are better understood, the following will begin the main context of the thesis. My experiments are carried out based on the understanding of the ZnO related literatures, preparation and general characterization of methods of ZnO material.

This thesis is based on the preparation of ZnO nano-material, optically pumped ZnO lasers, electrically pumped ZnO lasers, ZnO based LEDs, ZnO based PDs, some preliminary explorations have been performed, the main research are listed as follows:

1. For the preparation of nano-material, the morphology controlled ZnO-based materials could be obtained?
2. The further lowered threshold of the optically pumped ZnO NW nanolasers could be realized? The electrically pumped ZnO based laser device could be realized? The ultra-low current injected ZnO based LEDs could be realized?
3. The PDs with different detecting wavelength could be integrated on a single chip? In order to achieve miniaturization of the detectors, the photodetectors without filters could be achieved?

My experiments are performed with these problems.

Chapter 3 Growth of ZnO Nanostructures and Related Structral, Photoluminescence Properties

So as to realize ZnO based nanodevices, the first step is to obtain ZnO nanostructures with controllable morphology. Then ZnO photoelectric nanodevices could be fabricated based on these structures. This chapter is mainly focused on how to prepare ZnO nanobolts using physical vapor deposition; how to realize ZnO nanowires with controllable growth; and how to measure the I-Vcharacteristic between ZnO nanowires and nanorods combing photolithography.

3.1 Structure and Photoluminescence Properties of Aligned ZnO Nanobolt Arrays

3.1.1 The Growth of ZnO Nanobolts

At present Wang Zhonglin et al have prepared various ZnO nanostructures with different morphologies such as nanorods, nanobelts, nano-combs, nano-sawteeth, nano-spirals, seamless nano-rings, core-shell structural nanobelts, nanotubes and nano-cage structures. [64] Although there were a mass of papers concerning the growth of 1D ZnO nanostructures, few reports tried to control the growth process to obtain designed nanostructures. They just got different ZnO nanostructures at certain growth parameters. In this work, we report a simple physical vapor deposition method to synthesize aligned ZnO nanobolts on a Si (100) substrate. In order to prepare this kind of nanostructure, two factors were considered. First a thin film of ZnO was used as the nucleation template to control the growth direction of the ZnO nanostructures. Second, a two-step growth process was performed to obtain bolt-like nanostructures on the Si (100) substrate at 650 °C by inducing the ZnO assisted layer. P-type Si (100) substrates were cleaned by organic solvent and etched in diluted HF acid to remove the contaminations and surface oxides. Subsequently, the substrates were coated with a ZnO thin film by electron beam evaporation. ZnO powder was prepared in tablet

form using traditional pressing technique, and was sintered in oxygen atmosphere at 800 °C for two hours. Using the prepared tablet as target, thin film was deposited using electron beam evaporation method under pressure of 2×10^{-4} Torr during deposition process, the substrate temperature was maintained at 400 °C. The Zn powder was placed in a quartz boat. The Si substrate was put downstream of the gas flow; the distance between the Zn source and the substrate was about 1 cm. The quartz boat was placed at the center of the tube furnace. Argon was introduced into the system as carrier gas with a flow rate of 200 SCCM. The tube was heated to 650 °C at a rate of 10 °C per minute and maintained at 650 °C for 1.5 h. Then the tube was cooled down to RT naturally (denoted as sample *A*). Under the same conditions, we conducted another experiment; the only difference was that when the system was cooled to 419 °C, we immediately turned off the argon gas. Air in the environment diffused into the reaction system. In this way, a gray-white layer was deposited on the substrates (denoted as sample *B*). For the sample grown under this condition but without a ZnO layer, we denoted it sample C.

Fig 3.1 (a, b) shows the SEM images of sample *A* synthesized on the Si (100) substrate at 650 °C by inducing the ZnO-assisted layer. We can see that nearly all the ZnO nanorods grow vertically to the surface of the substrate. The synthesized ZnO nanorods are about 1 μm in length and about 100 nm in diameter. Fig 3.1(c–e) shows the morphologies of sample B. When air was introduced into the reaction tube at 419 °C, the morphologies of the ZnO nanostructures dramatically changed from nanorods to nanobolts. The nanobolts are kept at about 1 μm in length with a stem diameter around 100 nm, while the top size of nanobolt is about 250 nm. A top view SEM image of ZnO nanobolts is displayed in Fig 3.1 (d), which shows that all the tops of the nanobolts have hexagonal morphology. The stem of the nanobolt exhibits almost circular shape as shown in the inset of Fig 3.1 (e) with high resolution. The SEM image of sample C is shown in Fig 3.1 (f), which indicates that without a ZnO seed layer the orientation of nanobolts is randomly distributed on the substrate surface. SEM image shown in Fig 3.1 (g) illustrates a homogenuous ZnO thin film prepared by electron beam deposition method.

Based on the above analysis, the ZnO nanobolt growth is assumed to proceed according to the following steps. The Zn source vaporized at 650 °C and went with the argon flow to form nanoisland structures on the substrate surface. Few amount of oxygen contained in the tube would react with Zn to grow 1D ZnO nanorods. Finally,

the Ar was stopped, and air in the environment diffused into the reaction tube at 419 °C. More oxygen would react with Zn vapor; this will lead to the formation of a large and flat hexagonal structure on the top, which may be ascribed to a 2D growth mode that dominated this procedure. Therefore, a capping layer with large diameter was grown on the top of the nanorod, which results in nanobolt formation. That is to say, the element ratio of Zn to O is a key parameter to synthesize the needed crystalline morphology in this experimental procedure.

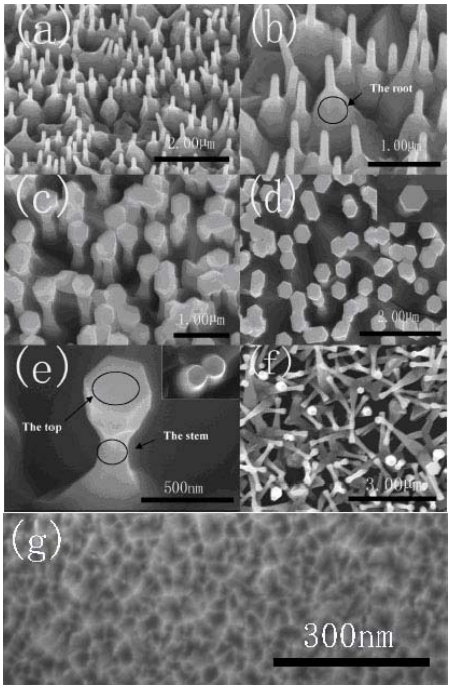

Fig 3.1 (a-b) SEM images of the aligned ZnO nanorods (sample *A*), (c-e) SEM images of the aligned ZnO nanobolts (sample *B*), and (f) ZnO nanobolts directly grown on a p-type Si (100) substrate (sample *C*), (g) SEM image of ZnO thin film prepared by electron beam deposition method.

3.1.2 Structural and Optical Properties of ZnO Nanobolts

The X-ray diffraction (XRD) patterns of the nanobolts and nanorods are displayed in Fig 3.2. The dominant diffraction peaks of two samples can be indexed to wurtzite hexagonal ZnO. For the nanobolts only, a (002) diffractive peak can be observed, which indicates that nanobolts are of perfect *c*-axis orientation. The peak position for nanobolts is located at 34.7°, which is larger than that of bulk ZnO (34.5°). The FWHM for nanobolts is 0.17°, which implies good crystallinity of ZnO nanobolts. According to the Laue equation, we can conclude that the *c* axis of ZnO nanobolts is

smaller than the bulk. For nanorods, three peaks related to ZnO were observed, which indicates that the orientation is not as good as that of the nanobolts; this may be ascribed to the lack of oxygen in the nanorods, for we did not let any oxygen in the reaction system during reactive time. The Si (200) peak emerged in the XRD pattern of the nanorods; this was attributed to the substrate.

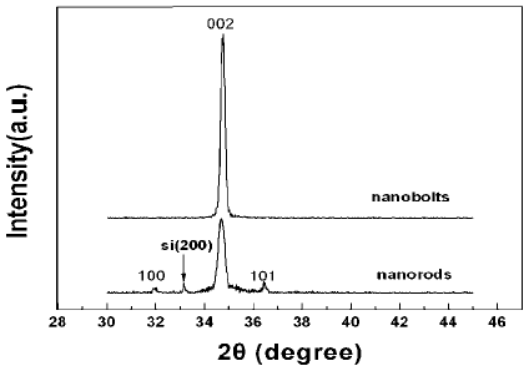

Fig 3.2 XRD patterns of ZnO nanorods (sample *A*) and nanobolts (Sample *B*) grown on P-type Si (100).

PL spectra of the ZnO nanostructures at RT are shown in Fig 3.3. A strong emission peak around 3.26 eV with a FWHM of 0.104 eV is observed for both ZnO nanorods and nanobolts. This emission peak could be attributed to exciton-related emission. Another defects-related emission band located at 2.48 eV was also found for these two samples. But the defects-related emission peak intensity of nanobolts is much weaker than that of nanorods. This defects-related emission in ZnO is generally speculated to originate from oxygen vacancies. [65]

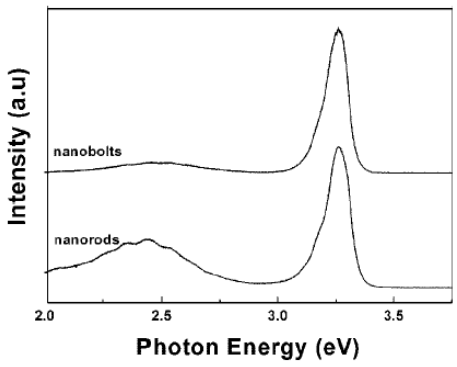

Fig 3.3 Room-temperature PL spectra of ZnO nanorods (sample *A*) and nanobolts (sample *B*) grown on P-type Si (100) substrates.

Table 3.1 shows the composition of ZnO nanorods and nanobolts measured by X-ray energy dispersive spectrometry (EDX) attached to SEM. We can clearly see that the ratio of O to Zn of nanobolts is larger than that of nanorods. The result is in good agreement with the discussion in the formation process of nanobolts and the PL spectra. More oxygen is observed in the case of 2D growth. It also means that the oxygen vacancies in ZnO nanobolts could be reduced, which decreases the defects-related emission.

Table 3.1 Zinc and Oxygen Composition of Nanorods and Nanobolts.

sample	Zn at %	O at %	Zn wt %	O wt %
nanorods	57.99	42.01	84.94	15.06
nanobolts	54.33	45.67	82.94	17.06

In order to further verify the origin of ultraviolet emission in ZnO nanobolts, the temperature-dependence of the PL spectra has been measured and is shown in Fig 3.4 in the temperature range 82–309 K. The inset of Fig 3.4 is a typical PL spectrum at 82 K. The so-called A-free exciton (FE) peak located at 3.371 eV was observed. A shallow donor-related bound exciton (BE) emission at 3.359 eV at the lower energy shoulder of the FE was found. The dominant peak located at 3.313 eV was assigned to E_V, which is a disputable one. According to experimental result, it did not show any shift with increasing excitation power, so it could not be a donor–acceptor pair. In order to explore the origin of the E_V transition, the energy positions of the BE, E_V and $E_V - kT/2$ versus temperature below 160 K are summarized in Fig 3.5. The fitting results are well in accordance with those reported by Zhao et al. [66] Therefore, the E_V peak was considered as a free to bound (FB) transition; meanwhile the longitudinal optical (LO)-phonon replicas of the E_V with up to four LO-phonons were observed, which were assigned to E_V - 1LO, E_V - 2LO, E_V - 3LO, and E_V - 4LO, because the energy separation between E_V and E_V - 1LO, E_V - 2LO, E_V - 3LO, and E_V - 4LO is one, two, three, and four times 70 meV, respectively.

The sharp transitions developing into a broad band was also observed with increasing temperature in Fig 3.4. The intensity of the E_V emission decreased more slowly than that of BE and FE with increasing temperature. The FE transition became part of the broad emission band when the temperature reached room temperature. Therefore, the strong emission (~3.26 eV) at room temperature is originated from a

free-to-bound transition.

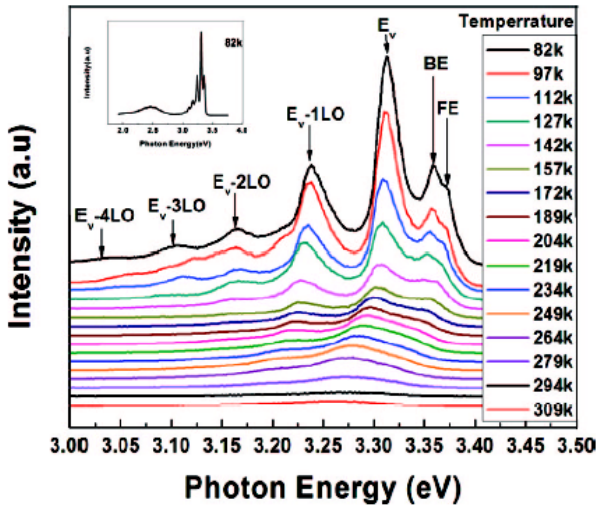

Fig 3.4 Photoluminescence spectra of the ZnO nanobolt arrays measured at different temperatures (from 82 to 309 K). The inset is a typical PL spectrum measured at 82K.

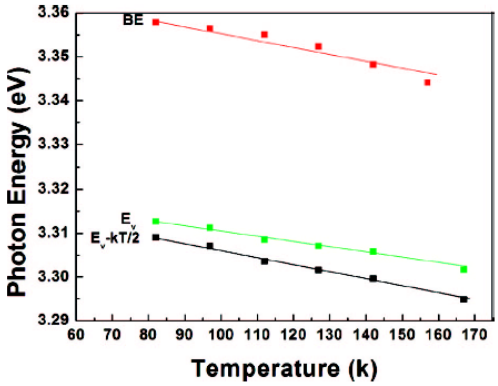

Fig 3.5 The transition energies of the BE, *E*V, and *E*V – *kT*/2 versus temperature.

It is observed the ZnO nanobolts were fabricated by vapor transport method through our experiment, and the growth mode can be changed from 1D to 2D growth by introducing oxygen gas, and the optical properties for the nanobolts were carried out.

3.2 Tuning the Growth of ZnO Nanowires

3.2.1 Preparation of ZnO Nanowires

Firstly, a direct current (DC) and radio frequency (RF) co-sputtering method was

used to deposit ZnO thin film (layer thickness from ~5 to 70 nm) on the cleaned Si (100) substrate. The samples with the growth time of 5, 10, 15 and 30min were denoted as *a*-, *a*, *a*+, *A*, respectively (Table 3.2). After the growth, the sample *a* was cut into four pieces, in which three pieces were annealed at 600 °C, 800 °C and 1000 °C in air for 30 min and were denoted as *b*, *c* and *d*, respectively. The sample *A* which was processed with the same procedure denoted as *B*, *C*, *D*, respectively (Table 3.2). Secondly, ZnO NWs were fabricated on the substrates *a*, *b*, *c*, *d*, *A*, *B*, *C* and *D* by hydrothermal method using $Zn(CH_3COO)_2 \cdot 2H_2O$ and $C_6H_{12}N_4$ as reaction source, the reaction solution was adjusted to identical concentration (0.01 mol/L). Then the reaction kettle was put into an oven and maintained at 90°C for 24 h. The obtained samples were denoted as *a'*, *b' c'*, *d'*, *E*, *F*, *G* and *H*, respectively (Table 3.2). ZnO NWs which grown on substrate a under the same conditions in the above except the solution concentration was adjusted to 0.001mol/L was denoted as *a"*. substrate *A* annealled in Ar gas, at 1000 ° C for 30 minutes was used for preparing NWs, and then the concentration of 0.01mol / L solution was explored for the growth of ZnO nanowires by hydrothermal method, the obtained sample was designated as *H '*.

Table 3.2 Time deposition, layer thickness, particle size, annealing temperature for ZnO sub-layers, experimental conditions of ZnO NWs.

sample name	time deposition (min)	layer thickness (nm)	particle size (nm)	annealing temperature (°C)/ atmosphere	sample name after NW elaboration	concentration (mol/L)
a-	5	5	5	-	-	-
a	10	10	10	-	*a′*	0.01
a	10	10	10	-	*a″*	0.001
a+	15	20	20	-	-	-
A	30	70	46	-	*E*	0.01
b	10	10	20	600°C/air	*b′*	0.01
c	10	10	15	800°C/air	*c′*	0.01
d	10	10	-	1000°C/air	*d′*	0.01
B	30	70	68	600°C/air	*F*	0.01
C	30	70	81	800°C/air	*G*	0.01
D	30	70	138	1000°C/air	*H*	0.01
A	30	70	140	1000°C/Ar	*H′*	0.01

3.2.2 Structural and Morphological Properties of ZnO Sub-layers

The SEM images in Fig 3.6 of the as-grown ZnO samples *a*-, *a* and *a*+ fabricated by magnetron sputtering with the growth time of 5, 10 and 15min respectively show that sub-layers (SLs) are composed by particles. The average particle size increases

with deposition time from ~5, ~10, ~20, to 46 nm for samples obtained with deposition time changing from 5, 10, 15 to 30 min respectively.

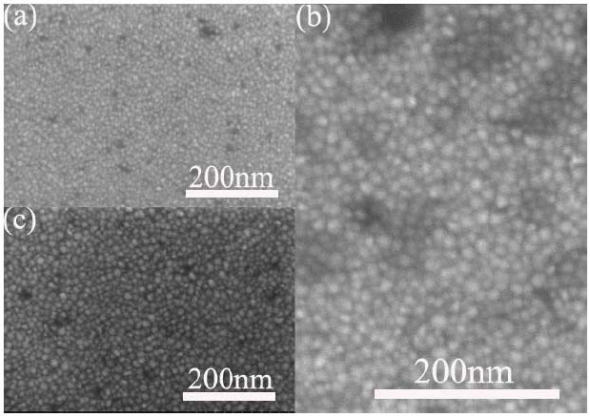

Fig 3.6 (a-c) SEM images of the SLs *a*-, *a* and *a*+, respectively fabricated by magnetron sputtering with the growth time of 5, 10 and 15min, respectively.

Fig 3.7 (a–d) shows the AFM images of the as-grown sample *A* and the corresponding annealed samples at 600 °C, 800 °C and 1000 °C in the air for 30 min. When the SL was annealed, the particle size became larger with increasing the annealing temperature. Clear grain like structure was observed for these images with an average size of 46, 68, 81 and 138 nm for the samples *A*-*D* respectively. For the sample *D* larger size dispersion was observed.

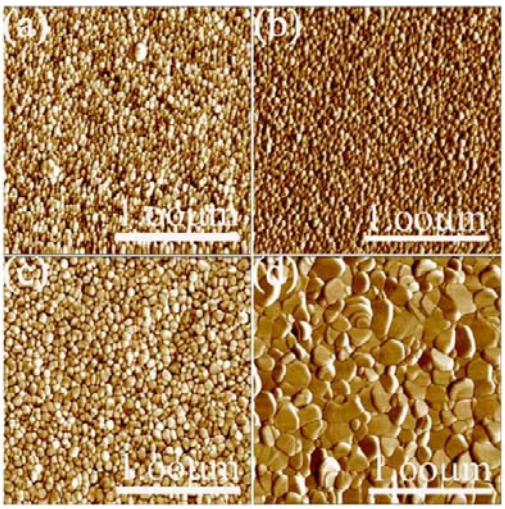

Fig 3.7 AFM images of the samples *A*, *B*, *C* and *D*: (a) as-grown SL, (b)-(d) 600 °C, 800 °C and 1000 °C annealed SLs respectively.

To explore structural properties of the as-grown and annealed SLs, XRD experiments were performed as shown in Fig 3.8. Only one peak corresponding to the (002) plane is observed in the x-ray spectra for all the samples indicating that all samples are highly c-axis oriented with the (002) plane parallel to the substrate. This behavior is due to the lowest surface energy of the (001) basal plane in ZnO. The (002) peak position of the reference ZnO powder is 2θ=34.45°. [67] The diffraction peak position of the as-grown ZnO SL (Table 3.3) is less than the powder value indicating that the film is in a uniform state of strain with expansion components parallel to the c-axis. It is also observed that the peak position of (002) plane shifts close to the powder value when the annealing temperature is at 600 °C. This peak position starts to shift into larger degree compared to the powder value when the annealing temperature is at 800 °C and 1000 °C. If this macro-strain was only due to residual stress effect induced by the growth method, the initial stress in the as-grown sample would be in one direction and changes into an opposite direction after annealing at higher temperature.

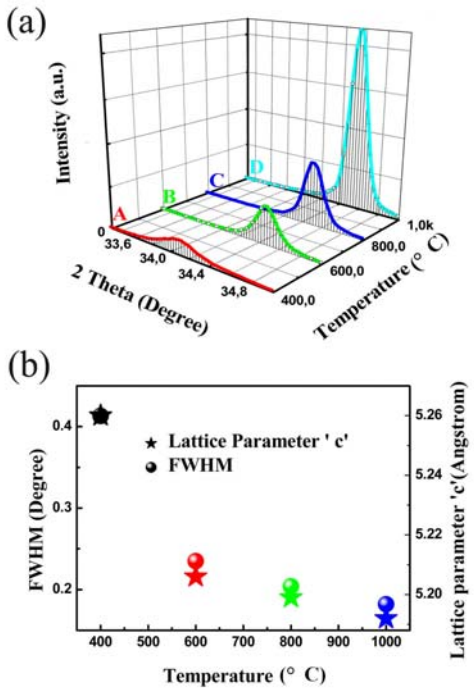

Fig 3.8 XRD pattern of (a) *A* - *D* samples with (c) corresponding 'c' lattice parameter and FWHM values versus temperature.

Table 3.3 the XRD structural analysis and RBS, EDX measurements for sample *a*, *A-D*.

Sample	$2\theta_{max}$	Integral area	FWHM β	Lattice Parameter	Stress (GPa)	Domain size	O at % RBS	O% EDX
	±0.01°	±5%	±0.01°	c (Å)	±0.1GPa	(nm)		
a(10nm)	33.98°	1107	0.671°	5.270	2.79	14		
A	34.08°	2270	0.413°	5.260	2.35	23	48.5	0
B	34.45°	2960	0.235°	5.206	0	39	49	0
C	34.49°	3390	0.204°	5.199	0.30	45	49	0
D	34.54°	6780	0.182°	5.192	0.61	56	50	+3
Unstress	34.45°	---	---	5.206	0	---	50	---

The calculated values of the lattice constant are listed in the Table 3.3. The large value of the lattice parameter "c" for the as-grown films compared with the unstressed powder value shows that the unit cell is elongated along the c axis, and compressive force acts in the plane of the film. The compressive force almost disappeared at annealing temperature of 600 °C resulting in a decrease in "c" value. Considering isotropic stress components in the film plane and no out-of-plane stress components (biaxial state), the in-plane stress σ can be expressed from the out-of-plane strain value e_{zz} as A. Segmüller et al reported: [68]

$$\sigma = \left[c_{13} - \left(c_{11} + c_{12}\right)c_{33} / 2 * c_{13}\right]e_{ZZ}, \tag{3-1}$$

$$e_{ZZ} = \left(c - c_0\right)/c_0, \tag{3-2}$$

Where c_{ij} are the elastic stiffness constants of ZnO, [69] c is the lattice parameter obtained from the (002) peak position, and the c_0 corresponds to the free stressed and stoichiometric value. According to the equations, the residual stress of our as-grown and annealed buffer layers could be calculated and summarized in Table 3.3. Stress in ZnO film contains a thermal component and an intrinsic component. The thermal stress is the result of the difference between the thermal expansion coefficient of the coating and the substrate. The thermal expansion coefficient of ZnO is larger than that of silicon, resulting in a tensile lateral stress in the ZnO film due to cooling after deposition. Considering the substrate and film expansion coefficients (bulk ZnO: 4.75×10^{-6}/K and bulk Si: 2.59×10^{-6}/K [70]) and the difference between the coating temperature (400 °C) and RT, the tensile thermal stress is evaluated around 0.5 GPa. The resulting intrinsic compressive stress (around 2.85 GPa) is a typical behavior in sputtered ZnO thin film and is commonly associated with grain boundaries and

interstitial atoms in ZnO lattice due to the 'atomic peening' mechanism originated from energetic species interaction with the growing surface. [71] The difficulty is to separate the strain variation due to the stress relaxation from the oxygen stoichiometry variation. The RBS measurements (Table 3.3) supported by EDX analysis show that the oxygen atomic concentration is almost constant between the as-grown sample and the *B* and *C* samples. These results confirm that the decrease of the c-axis parameter is due to annealing, which is a pure mechanical stress relaxation (defects, grains boundaries...) as reported by Vinay Gupta et al. [72] On the contrary, the annealing at 1000 °C is a combination of several mechanisms of atom diffusion which induces large re-crystallization process (grain growth and equi-atomic composition state). In this case, the variation of the lattice parameter c is due to complete stress relaxation and structural rearrangement of the crystalline domain. The variation Δc/c for the sample *D* with respect to a perfect unstressed sample is of -0.27% which is a very small variation. The domain size *D* has been evaluated from the integral width β of the (002) and (004) lines according to the Scherrer's relation: [73]

$$D = K\lambda / \left[\cos\theta\left(\beta^2 - \beta_0{}^2\right)^{1/2}(\pi/180)\right] \qquad (3\text{-}3)$$

With the Cu-Kα radiation wavelength of λ =0.15418 nm, the correction form factor k=1, the diffraction angle θ and the integral peak width β_0 caused by instrumental broadening. The grain size increases from 14 to 23 nm with increasing the deposition time and to 56 nm with increasing the annealing temperature. This process has been suggested by Hickernell as a re-crystallization occurring during annealing. [74] SEM observations in cross-section reveal a ZnO layer thickness around 70 nm. This value is close to the domain size *D* (which is an evaluation of the crystalline domain size in the c-axis dimension, perpendicular to the substrate surface) obtained in the sample *D*.

As observed by AFM, the as-grown ZnO SL was composed by smaller particles, and the particle size became larger after increasing annealing temperature, these observations indicated that merging processes at the interface occurred and became very important as the temperature increased. Finally the integral intensity of the (002) peak is a parameter allowing the evaluation of the preferential orientation of the re-crystallized grains with respect to the substrate. This indicates an optimization of the orientation in addition to an improvement of the crystalline quality.

3.2.3 Morphological and Optical Properties of ZnO Nanowires

Two series of samples have been explored (Table 3.2): The first ones were grown

on 10 nm thick as-grown and annealed SL (the samples are denoted *a'*, *b'*, *c'*, *d'* and *a"*as described above), the second ones were on 70 nm thick as-grown and annealed SLs (the samples are denoted *E*, *F*, *G*, and *H* as described above).

Fig 3.9 (a-d) shows top view SEM images of samples *a'*, *b'*, *c'* and *d'*. Top agglomerate ZnO NWs were observed forming wiring harness like structure for samples *a'*, *b'* and *c'* with the diameter of the NWs around 50 nm. The top agglomerate phenomenon became much more serious when the SL annealing temperature was 800 °C. The number of NWs forming one wiring harness increases from around 15 to around 30 wires for *a'* and *c'* samples. Nothing was obtained for sample *d'* may be due to the phase transition of the thin SL under higher annealing temperature at 1000 °C [O: Zn= 71:29 (atom ratio) for the sample *d*)].

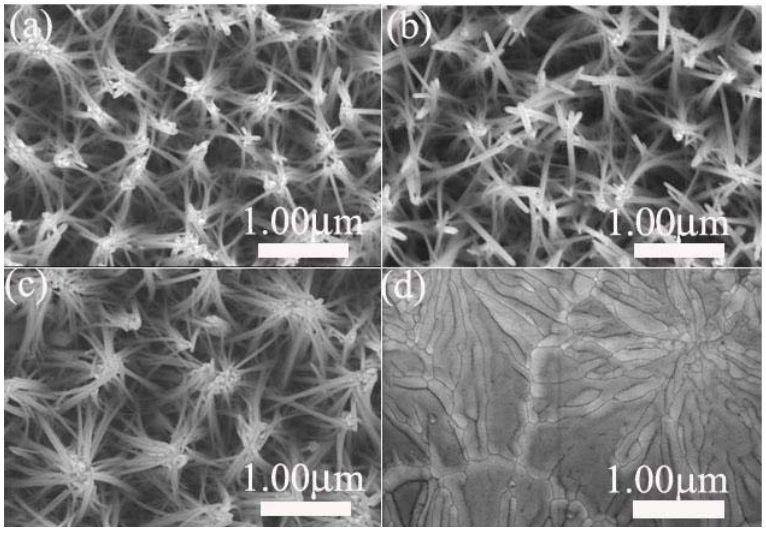

Fig 3.9 (a – c) SEM images of the samples *a'*, *b'*, *c'* and *d'*.

To get smaller diameter NWs, the solution concentration have been lowered to 0.001 mol/L for the sample *a"*. As shown in Fig 3.10, besides wires with larger diameter of about 30 nm, ultra fine ZnO NWs with diameter of ~11 nm with large aspect ratio (~200 for the longest NWs) were obtained.

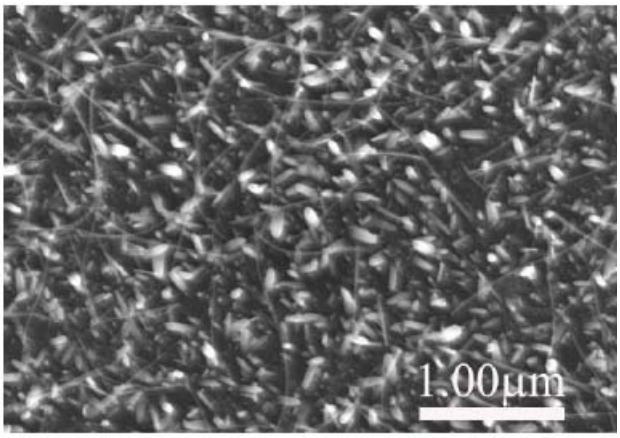

Fig 3.10 SEM image of the samples *a"*.

PL spectra of samples *a'*, *b'*, *c'* and *a"* are performed shown in the Fig 3.11. One obvious characteristic is that the PL peak position for the sample *a"* is located at 375 nm while that for sample *a'* located at 380 nm may be due to size effect; [75] the relationshipd between gap *E* and size can be expressed as follows:

$$E = E_g + h^2/8\mu R^2 - 1.8e^2/4\pi\varepsilon_0\varepsilon_\infty R \tag{3-4}$$

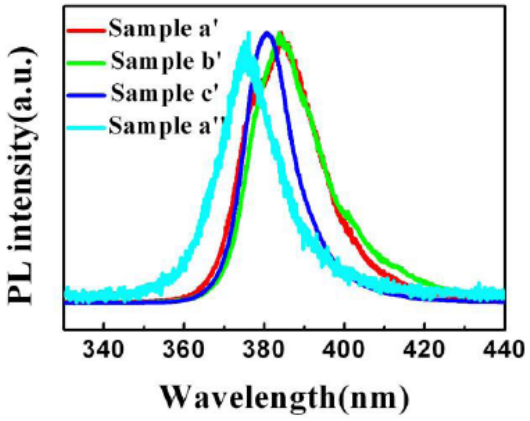

Fig 3.11 PL spectra of the samples *a'*, *b'*, *c'* and *a"*.

Where *h* planck constant，E_g is band gap for bulk material，μ is effective mass for exciton ($1/\mu=1/m_e+1/m_h$)，ε_∞ is high frequency dielectric constant，*R* is particle size，the first is the confinement term related to size ($\propto 1/R^2$)，the second is coulomb term ($\propto 1/R$)。In fact, the UV emission peak position is not only related to size of material, but also the defects inside ZnO will cause shift of the emission peak.

Another is that the FWHM of sample c' (less than 13 nm) is much narrower than that of others (the FWHM of sample a' and b' is both 17 nm). This result indicates that PL emission properties of the epitaxial NWs have close relation with the crystal quality of the substrate for the annealing could enhance the crystal quality of the SL, thus the improved crystal quality for the homo-epitaxial NWs could be easily obtained (the contribution of the SLs for the PL emission can be neglected compared with that of the epitaxial nanostructures).

Concerning the ZnO NWs obtained on thicker SLs (thickness=70 nm), top view and the corresponding cross-section images of the ZnO NWs fabricated on the substrates *A*, *B*, *C*, *D* are shown in Fig 3.12, which indicates that the thickness of the SL could influence the morphology of the ZnO NWs.

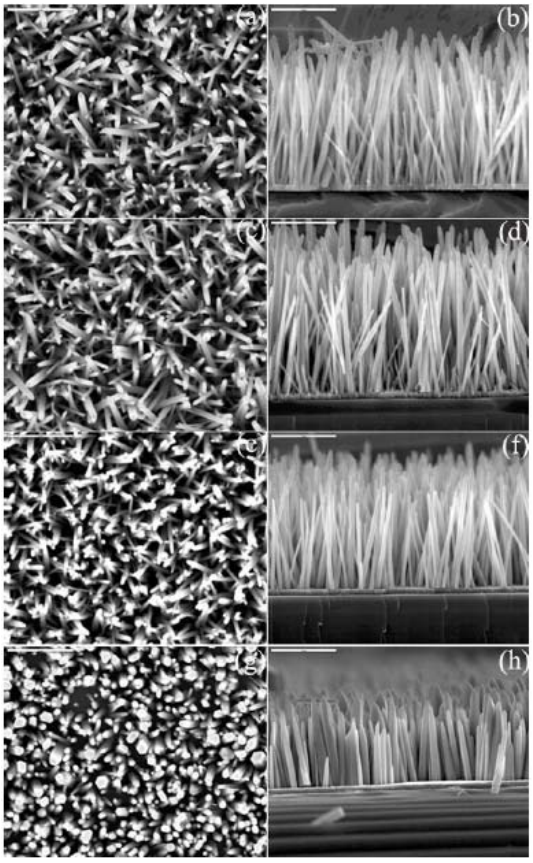

Fig 3.12 (a-b), (c-d), (e-f), (g-f) SEM images for samples *E*, *F*, *G* and *H*, respectively. The scale bar is 1 μm.

The intensity of the (002) peak enhanced with increasing the thickness of the SL in the XRD pattern. When the thickness of the SL reaches 70 nm, the NWs did not

agglomerate any more and became highly oriented. For the samples *E* to *H*, aligned ZnO NWs were obtained. The images of the sample H showed that the alignment is much better compared with the others. It seems that the annealing process has an important effect on the growth of the NWs: the thicker SL contributed to better growth orientation, and the larger grain size of the SL resulted in the bigger diameter of the NWs. The average diameter of the NWs was about 60 nm, 73 nm, 77 nm and 146 nm for the samples *E-H* respectively. These results illustrated that the morphology of the NWs could be affected by the thickness of the SL, and the diameter of epitaxial NWs could be tuned by the particle size of the SL. The average length is about 2.2, 2.1, 1.8 and 1.3 μm respectively for samples *F*, *G* and *H*, respectively. It is evident that the the sample *H* owning much shorter length compared with others may be due to higher diameter leading to lower growth rate along the c axis.

The corresponding XRD spectra of the samples E-H are shown in Fig 3.13(a). The measurements exhibited only one (002) peak indicating the highly preferential orientation for the samples.

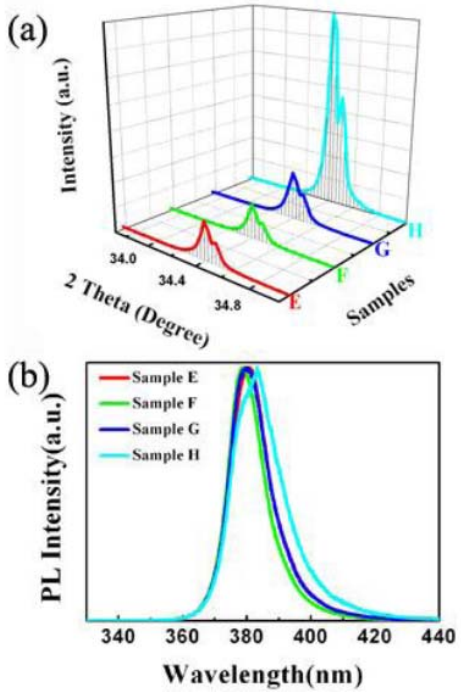

Fig 3.13 (a) The XRD patterns and (b) PL spectra of the samples *E* – *H*.

The small width of (002) peaks allows the resolution of $K\alpha_1/K\alpha_2$ radiation

contributions. Considering the $K\alpha_1$ contribution alone, the (002) peak analyzed by Gauss fitting is located at the same position for the four samples corresponding to a lattice parameter c=5.207 Å which is almost equals to the reference powder value. This illustrates that the oriented NWs are stress-free and probably close to the equi-atomic state. The obvious difference is that the (002) peak intensity of sample *H* is much stronger than those of other samples and the (002) integral breadth of this sample is close to the instrumental width. As the NW size in the c-axis direction is higher than 1 μm, this illustrates that the NWs own high crystal quality. The PL spectra indicating near band gap emission for the four samples E-H were shown in fig 3.13 (b). An obvious characteristic is that the UV peak position of the sample *H* has a slight shift to the longer wavelength, and the FWHM of the sample *H* in the UV is much broader than that of the others, which is also due to size effect as mentioned above. [75]

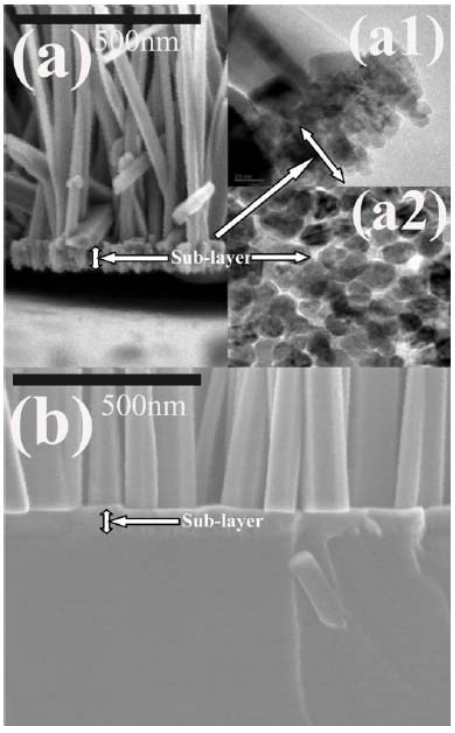

Fig 3.14 (a, b) SEM images of the samples *E* and *H*, respectively, The particle like structure of the SL is also shown in the TEM images in the inset in cross-section view (a_1) and in top view (a_2).

SEM and TEM analysis performed on samples *E* and *H* shown in Fig 3.14 revealing that the as-grown SL is formed by particle like structure as proved by the

insert TEM images (fig3.14 a_1 and a_2). The particle like structure disappeared after annealing (Fig 3.14 (b)). These observations indicated that merging processes at the interface occurred and became dominant as the annealing temperature increased.

TEM image (Fig 3.15) of the sample *H* shows a nanoneedle-like structure with large root and small tip. The HR-TEM and SAED (inserts) showed that the NWs are single crystalline. The lattice fringes are perpendicular to the wire axis indicating that the ZnO NW grew along the (001) direction. Moreover, the interplanar distance measured along the NW is equal for both the root and the tip. It means that lattice parameter "c" is uniform along the whole NW.

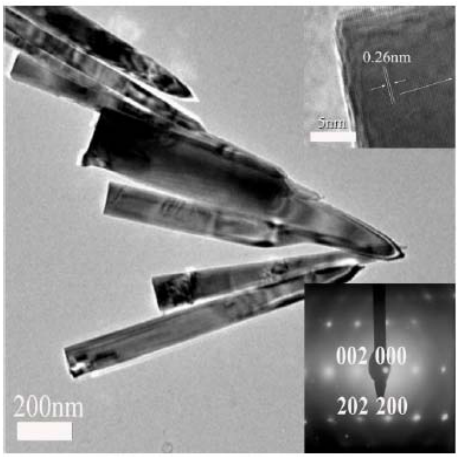

Fig 3.15 The TEM image of the ZnO NWs (sample *H*) with the HR-TEM image (upper trace) and the SAED (lower trace) of the NW shown in the insets.

These results demonstrate the homo-epitaxial growth of the c-axis oriented ZnO NWs onto the c-axis oriented SL. In order to control the growth rate of the NWs, the sample *A* annealed at 1000 °C in the Ar gas for 30 min used for growing NWs by hydrothermal method under the same conditions as mentioned above, similar results as the sample *D* were obtained in terms of the particle size, lattice parameter, stress value and domain size for the annealed SL, the corresponding AFM image of the annealed SL was shown in fig 3.16 (a). Concerning the NWs grown on this kind of SL shown in Fig 3.16 (b-c), the obvious difference is the length of the NW which is more than two times larger compared with that of the sample *H*.

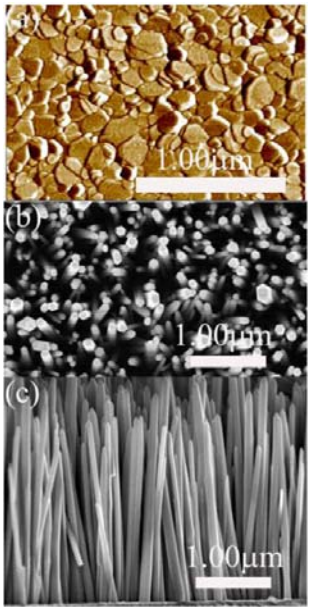

Fig 3.16(a) AFM image ZnO SL annealed at 1000 °C in Ar gas for 30 min, (b) and (c) top morphology and cross-section SEM images of the NWs prepared on the corresponding SL respectively.

ZnO NWs were prepared using hydrothermal method as mentioned above, it is found out that the size of the epitaxial nanowires can be tuned by design of the experimental parameters.

3.3 1D ZnO Based Homotype Homojunction

3.3.1 Fabrication of 1D Homotype Homojunction

The thin film fabricated by electron beam deposition was then etched into the interdigital electrodes in 5% HCl water solution. ZnO NWs were prepared on the interdigital ZnO film electrodes by hydrothermal method using $Zn(CH_3COO)_2 \cdot 2H_2O$ and $C_6H_{12}N_4$ as reaction source. The reaction solution was adjusted to identical concentration (0.01 mol /L) and the reaction kettle was put into an oven and maintained at 90 °C for 24 h. During this step, several nanorods were also formed in the solution. Then In metal was chosen for the Ohmic contact to the interdigital ZnO electrodes.

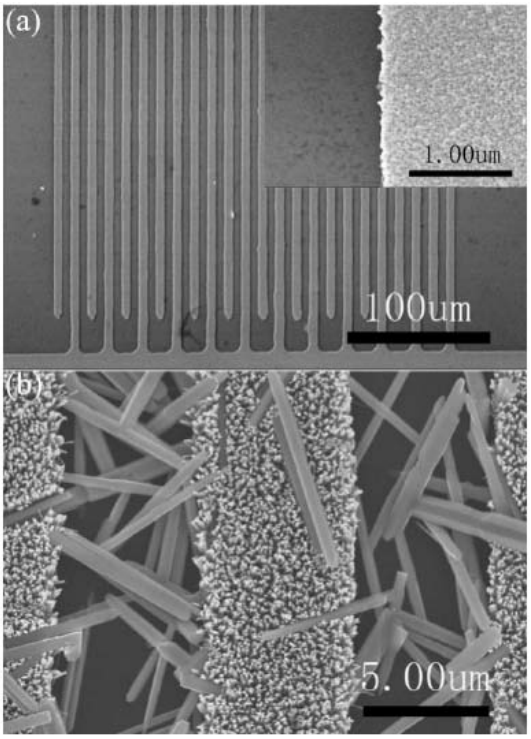

Fig 3.17 (a) SEM image of the interdigital ZnO film electrodes, the inset shows magnified image. (b) SEM image of ZnO NW arrays prepared on the interdigital ZnO film electrodes and the larger diameter nanorods lying between the interdigital electrodes.

Fig 3.17 (a) shows the interdigital ZnO film electrodes obtained after wet etching method using 5% HCl water solution, the inset shows magnified SEM image of the etched ZnO film, from which we can clearly observe that all the ZnO interdigital electrodes are homogeneous. The electrodes have 6 μm in width with same regularly space of 6 μm. Fig 3.17 (b) shows SEM image of ZnO NW arrays formed on the interdigital ZnO film electrodes, we can observe that all the ZnO NW arrays grow only vertically to the surface of the ZnO film. Moreover, some larger diameter nanorods (NRs) are deposited on the top of the ZnO NW arrays. These NRs, which formed in the solution allow the connexion of the interdigital ZnO electrodes. EDX measurements show that O to Zn concentration equals to 51:49 (atomic percentage) both for NWs and NRs.

3.3.2 Characterization of 1D Homotype Homojunction

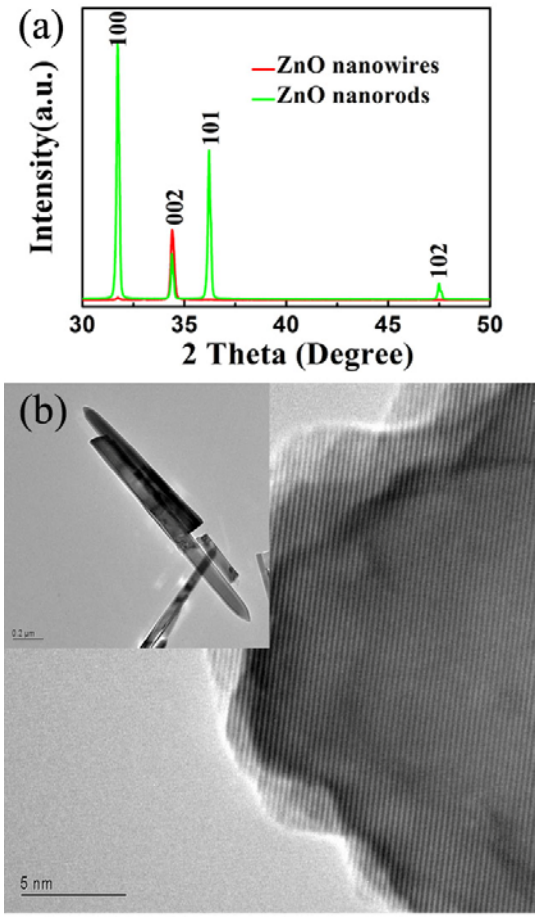

Fig 3.18 (a) XRD patterns of the ZnO NWs and NRs. (b) TEM image showing the morphology of ZnO NWs, the insert shows the corresponding HR-TEM image, revealing the monocrystalline nature of the NWs.

The XRD patterns of the NWs and NRs are displayed in Fig 3.18 (a). The dominant diffraction peak of NWs can be indexed to wurtzite hexagonal ZnO. For the NRs several diffractive peaks can be observed for the random distribution of NRs. The (002) peaks position for NWs and NRs are both located at 34.5°, the full width at half-maximum is 0.15°, which implies good crystallinity of ZnO nanostructures in the XRD. In order to further explore the crystal quality of the ZnO NWs, TEM and HR-TEM have been performed as shown in Fig 3.18 (b). The TEM image clearly displays that ZnO NWs are straight with sharp tips. The HR-TEM image of ZnO NW at the top shows a taper structure with a lattice spacing of about 0.26 nm which corresponds to the interlayer spacing of the (002) planes in the ZnO crystal lattice, one

can conclude that ZnO NWs grew in the (001) direction.

Fig 3.19 (a) shows current versus voltage curves of the homojunction exhibiting nonlinear symmetrical properties from 30 K to 290 K. It can be seen that this nonlinear behavior presents a turn on voltage of about 3.2 V at 30 K. The lower turn on voltage might be attributed to the homotype structure, and the high defect concentration in the interface as reported previously. [76,77] The homojunction keeps a nonlinear characteristic even when increasing the temperature up to 290 K. The *I-V* characteristics between two as-deposited In metal electrode contacts on ZnO film and NWs are both linear at RT (Fig 3.19 (b)) indicating the formation of Ohmic contacts, so we conclude that the homojunction may be formed between ZnO NWs and NRs, and the contacts between NWs and NRs are not so close, so the this kind of interface effcts may be magnified.

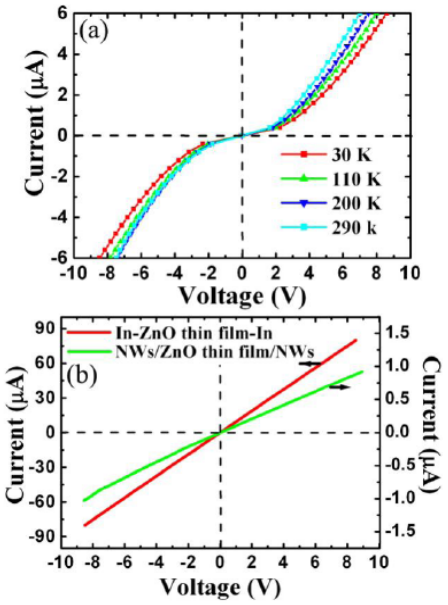

Fig 3.19 (a) Temperature dependent I-V curves of the homojunction. (b) The linear lines for In-ZnO thin film-In and In-NWs/ZnO thin film/NWs-In demonstrate the Ohmic contacts between ZnO film and In electrodes, thin film and NWs were formed.

In order to explore the origin of the homotype homojunction, XPS measurements were performed. As shown in Fig 3.20 (a), the C 1s peak position located at 284.6 eV for both NWs and NRs is observed. The intensity for NWs is much stronger than that for NRs, this is due to the surface adsorption capability of the NWs that is much more powerful than that of the NRs due to larger surface to volume ratio for the NWs. The

stronger peak intensity of C 1s for both samples was ascribed to the carbon contaminants due to the reactants decomposition reaction. This indicates that the surface of the NWs and NRs is far from "clean". The component on the binding energy side (Fig 3.20 (b)) of the O1s spectrum at 530.15 ± 0.15 eV is attributed to O^{2-} ions on wurtzite structure of hexagonal Zn^{2+} ion array, surrounded by Zn atom with their full complement of nearest- neighbor O^{2-} ions. [78] In this figure, a shoulder peak intensity of O 1s centered at 532 eV can be observed and is stronger for NWs than for NRs. This shoulder peak is due to the chemisorbed oxygen caused by surface hydroxyl, which corresponds to O-H bounds. [79] Because of the surface absorbed chemical elements such as C, O and H may cause a thin barrier layer between ZnO NWs and NRs. The homotype homojunction phenomena were observed based on 1D ZnO structures.

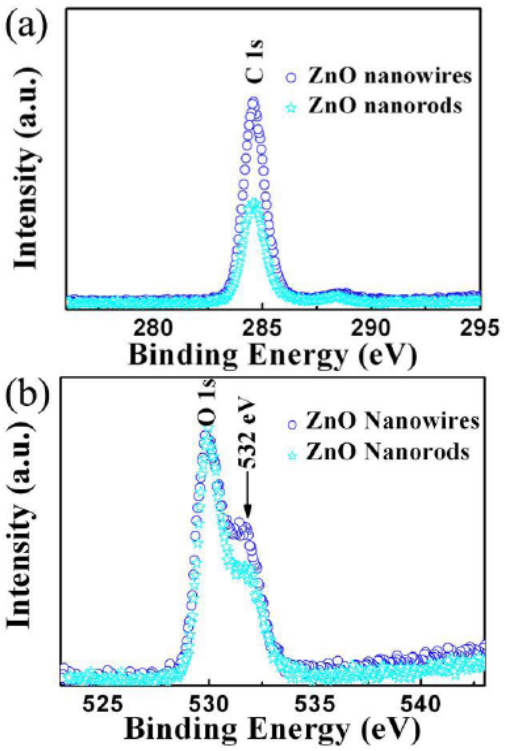

Fig 3.20 (a-b) XPS spectra of ZnO NWs and NRs for the C 1s and O 1s, respectively.

So as to further prove the existence of the surface adsorbed chemical elements, the normalized RT PL spectra of the ZnO NWs and NRs were performed as shown in Fig 3.21. The UV emission peak positions centered at almost the same place could be

attributed to the near band edge emissions in ZnO. An obvious characteristic is the broad visible emission ranging from 450 nm to 650 nm with peak position located at about 560 nm, this visible emission in ZnO is generally deduced originated from defects inside, the NWs and NRs formed under the same conditions should own the same crystal quality, so the same PL results should be obtained for NWs and NRs. Otherwise, the emission intensity in the visible region for NWs is much stronger than that of NRs. This observation proves further that ZnO NWs own much more powerful chemical elements adsorption resulting in stronger visible emission intensity for their larger surface to volume ratio, thus some donar and acceptor levels will be easily formed between valance band and conductive band resulting in much more surface to volume defects for NWs, the NWs will own much stronger visible emission.

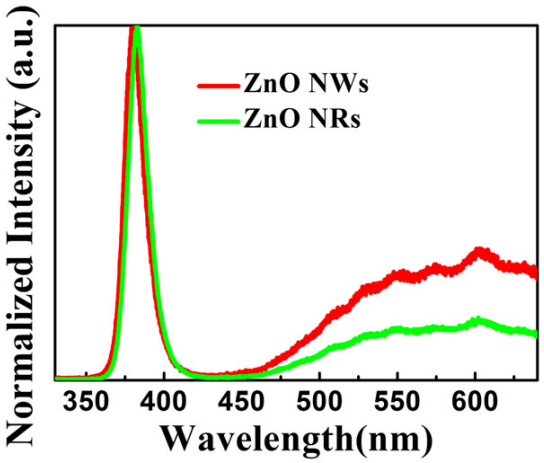

Fig 3.21 PL spectra for the as grown ZnO NWs and NRs.

In the above experiment, 1D ZnO homotype homojunction was fabricated combining photolithography and hydrothermal method, it is observed that the existence of surface defects resulting in the formation of homotype homojunction. In other words, we should pay more attention to the surface effects especially for fabricating nanodevices.

3.4 Conclusion

In this chapter, the controlled growth of ZnO nanostructures have been carried out by physical vapor deposition and hydrothermal method, the related structural and PL properties of the nanostructures are measured.

1. We have successfully fabricated the aligned ZnO nanobolt and nanorod arrays by physical vapor deposition method. Through our experiments, we confirmed that the morphology of ZnO nanomaterial could be controlled by adjusting the growth parameters such as temperature and carrier gas. With introduction of oxygen gas from environment, the defects related emission decreased. Furthermore, a transition of free-to-bound characteristic was observed by temperature dependent PL. This free-to-bound transition can survive up to room temperature, and E_V - 1LO, E_V - 2LO, E_V - 3LO, and E_V - 4LO were observed at 82 K. XRD patterns and PL spectra showed that our synthesized nanobolts had good crystal quality.
2. Highly oriented growth of the ZnO nanostructures can be tuned by a ZnO sublayer. The size (diameter and length) of the epitaxial NWs could be tuned under proper conditions by hydrothermal method combining ZnO sublayer, the diameter of the NWs is greatly influenced by the particle size of the SL and solution concentration. So we have shown that the diameter of the homo-epitaxial NWs is in accordance with the the particle size of the SL. The effects of annealing atmosphere on the SL will strongly influence the growth rate of the epitaxial NWs, thus we could tune the size of the ZnO NWs through adjusting growth conditions.
3. Homotype homojunction has been realized between ZnO NWs and NRs. The experimental results confirm the existence of the surface adsorbed chemical elements resulting in the formation of the homotype homounction based on ZnO NWs and NRs, these surface adsorbed chemical elements could form a thin barrier layer in the interface for the electrical devices.

Chapter 4 ZnO Based Light Emitting Devices

It is foud out that morphology and size of ZnO material can be tuned through adjusting experimental parameters in the above. Optically and electrically pumped ZnO lasers and ultralow driven current light emitting devices will be carried out in this chapter based on the experiments mentioned in the last chapter.

4.1 Optically Pumped ZnO Nanowire UV Lasers

4.1.1 ZnO Nanowire UV Lasers

(1) Fabrication of Aligned ZnO NWs

The ZnO thin film was fabricated by RF magnetron sputtering method using a 99.999% pure ZnO target under a power of 130 W. Before being loaded into the sputtering chamber, Si substrate was cleaned by organic solvents and rinsed by deionized water to remove the contaminations. During the sputtering process, a mixed gas of oxygen and argon with the same flow rate of 20 SCCM was introduced into the chamber and the working pressure was maintained at 1 Pa. The substrate was kept at RT with a rotation speed of 20 loops per minute and the growth time was 1 h. After sputtering ZnO thin film on Si substrate, the annealing process was done at 1000 °C for 30 min in the air. Then, a hydrothermal method was explored to grown ZnO NWs on thin film using $Zn(CH_3COO)_2 \cdot 2H_2O$ and $C_6H_{12}N_4$ as reactant source. The reaction solution was adjusted to identical concentration (0.01 mol/L). Then the reaction kettle was put into an oven and maintained at 90 °C for 16 h. Finally, the obtained sample was rinsed by deionized water and dried in the oven.

(2) Characterization of Morphological, Structural and Optical Properties of Aligned ZnO NWs

Fig 4.1 **(**a) shows top view SEM image of ZnO NWs synthesized on the Si (100) substrate with ZnO-assisted layer. We can see that nearly all the ZnO NWs grow vertically to the surface of the substrate. The synthesized ZnO NWs are about 1.3 μm in length and more than 100 nm in diameter. The XRD pattern of the NWs is displayed in Fig 4.1 (b). For the NWs, only a (002) diffractive peak of the ZnO

hexagonal wurtzite phase can be observed, which indicates that NWs are with perfect *c*-axis orientation. The peak position for NWs is located at 34.5 °, which equals to that of bulk ZnO. The FWHM for NWs is 0.11°, and the magnified (002) pattern shown in the inset is actually comprised by two peaks, which implies good crystallinity of ZnO NWs.

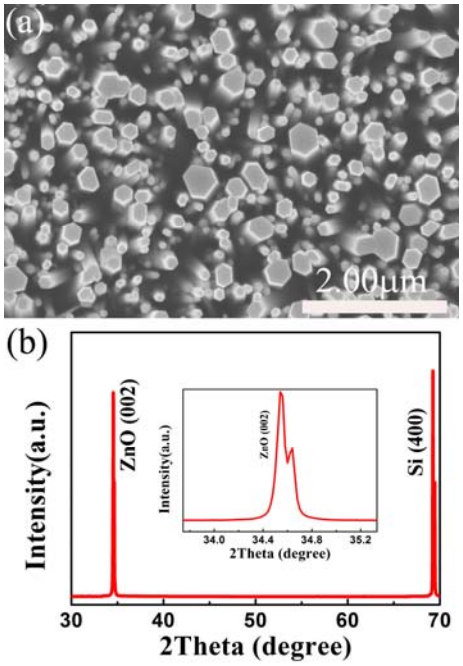

Fig 4.1 (a) SEM image of the aligned ZnO NWs, (b) XRD pattern of the ZnO NWs grown on Si substrate with ZnO sublayer.

PL spectrum of the ZnO NWs at RT is shown in Fig 4.2. A strong emission peak around 3.25 eV with a FWHM of 0.10 eV is observed for ZnO NWs. This emission peak could be attributed to near band edge emission. Another broad defects-related emission band located at around 2.40 eV was also found for the sample. This defects-related emission in ZnO is generally speculated to originate from oxygen vacancies.

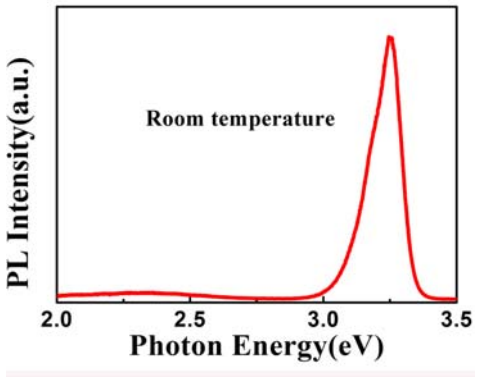

Fig 4.2 RT PL spectrum of ZnO NWs grown on Si substrate with ZnO sublayer.

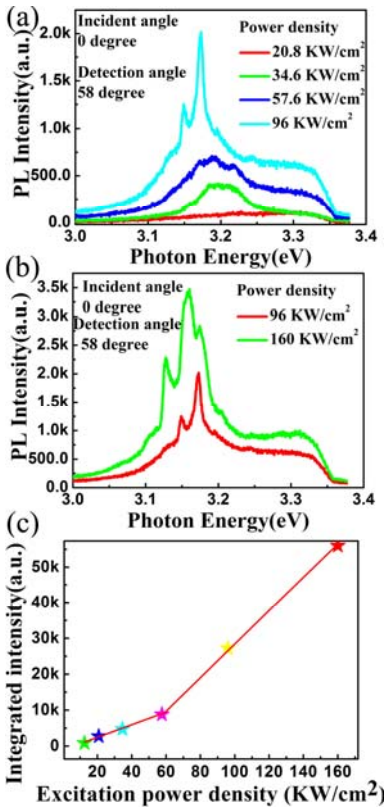

Fig 4.3 (a-b) The evolution of the RT PL spectra in the ZnO NWs as the excitation density increases from 20.8 to 160 kW/cm^2 by a mode-locked femtosecond Ti : sapphire laser. (c) The corresponding integrated intensity of the stimulated emission as a function of the excitation power density.

The optically pumped emission measurements were performed using an optical parametric amplifier (OPA) in an active passive mode-locked femtosecond Ti: sapphire laser. The excited wavelength of the laser output was adjusted to 350 nm.

Fig 4.3 (a-b) shows the optically pumped emission spectra with the laser beam normal to the sample surface while the emission spectra were detected with an optical fiber placed at 58 ° relative to the incident laser beam. With changing the excitation densities from 20.8 to 34.6 kW/cm^2, only a broad spontaneous emission with a main emission peak shifted from 3.3 eV to 3.2 eV is observed with emission intensities increasing linearly. When the excited laser power density exceeds threshold level of about 60 kW/cm^2, two sharp peaks with FWHM less than 0.006 eV emerged on the broad spontaneous emission band. As the excitation density increases further to 160 kW /cm^2, three obvious sharp peaks shown in Fig 4.3 (b) were observed accompanied with further red-shift for the lasing modes. As the pump power density increases, the gain becomes larger enough to enable cavity modes with higher loss to start lasing. As shown in the Fig 4.3 (c), the integrated intensity of the spectra increases nonlinearly with the excitation power density, and the transitions from the spontaneous emission to lasing at about 96 KW/cm^2 can be clearly observed.

As shown in Fig 4.4 with incident angle of 0 ° and excitation power density of 160 KW/cm^2 the laser emission spectra vary with the observation angle.

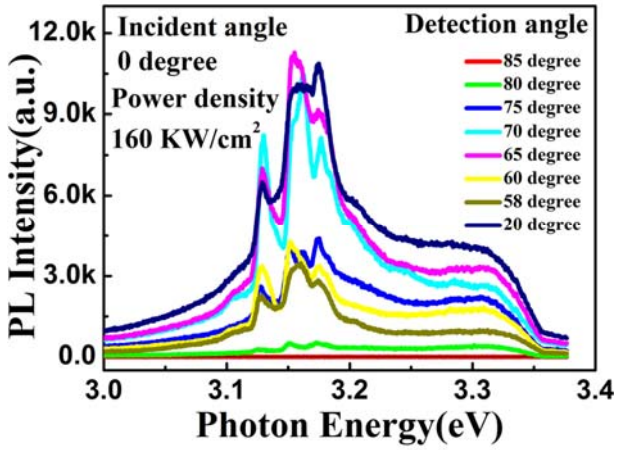

Fig 4.4 The RT PL spectra in the ZnO NWs under different detection angles with the excitation power density of 160 kW/cm^2.

These results force us to consider that different laser cavities may be formed by multiple scattering could have different output directions, lasing modes observed at different angles are different. Since the average NW size was much larger than the wavelength in the length, and less in the diameter, a single NW could serve as a FP resonator. For the NW size in the diameter is less than the emission wavelength

according to the SEM image. Thus a single NW is too small to serve as a laser resonator in the side surfaces. Instead, laser resonators are formed by recurrent light scattering. [80] Since this kind of lasing emission needs much larger excitation power density as reported by others, [81,82] in our case, the morphology of obtained NWs shows needle shaped structure, we think that the inclined surfaces at the top change the direction of the putput laser.

4.1.2 Further Lowered Threshold for Optically Pumped ZnO Nanowire UV Lasers

(1) Fabrication of ZnO NWs

Firstly, the Pt thin film (thickness: 300 nm) was prepared on Si substrate by RF magnetron sputtering method using a 99.999% pure Pt target, then a thin layer of ZnO (thickness ~30 nm) was sputtered on the Pt layer. Before being loaded into the sputtering chamber, the Si substrate was cleaned by organic solvents and rinsed by deionized water to remove the contaminations. During the sputtering process, only argon gas with flow rate of 30 SCCM for sputtering Pt film, and mixed gases of oxygen and argon with the same flow rate of 20 SCCM for sputtering ZnO layer were introduced into the chamber and the working pressure was maintained at 1 Pa. The substrate was kept at RT with a rotation speed of 20 loops per minute. Then, a hydrothermal method was explored to grow ZnO NWs using Zn $(CH_3COO)_2 \cdot 2H_2O$ and $C_6H_{12}N_4$ as reactant source. The reaction solution was adjusted to identical concentration (0.01mol/L), and the surface of the ZnO seed layer was loaded towards the bottom of the reaction kettle. Then the reaction kettle was put into an oven and maintained at 90 °C for 16 h. Finally, the obtained sample was rinsed by deionized water and dried in the oven.

(2) Characterization for Morphological, Structural and Optical Properties of Aligned ZnO NWs

Fig 4.5 (a) shows the cross-sectional SEM image of the ZnO NWs synthesized on the Si (Pt) substrate using the ZnO assisted layer. The obtained ZnO NWs are about 3 μm in length and more than 100 nm in diameter. The XRD pattern of the NWs is displayed in Fig 4.5 (b). The diffraction peak of the sample can be indexed to wurtzite hexagonal ZnO. For the NWs, only a (002) diffractive peak besides Pt (111) can be observed, which indicates that NWs are of c-axis orientation. The peak position for the NWs is located at 34.5°, which equals to that of bulk ZnO. The FWHM for the NWs is 0.10° and the magnified (002) pattern shown in the inset is

actually comprised by two peaks, which implies good crystallinity of the NWs. PL spectrum of the ZnO NWs at RT are shown in Fig 4.5 (c). A strong emission peak around 3.30 eV with a FWHM of 0.13 eV is observed for the ZnO NWs. This emission peak could be attributed to near band edge emission. Another very weak defects-related emission band located at around 2.30 eV was also found for the sample. This defects-related emission in ZnO is generally speculated to originate from oxygen vacancies.

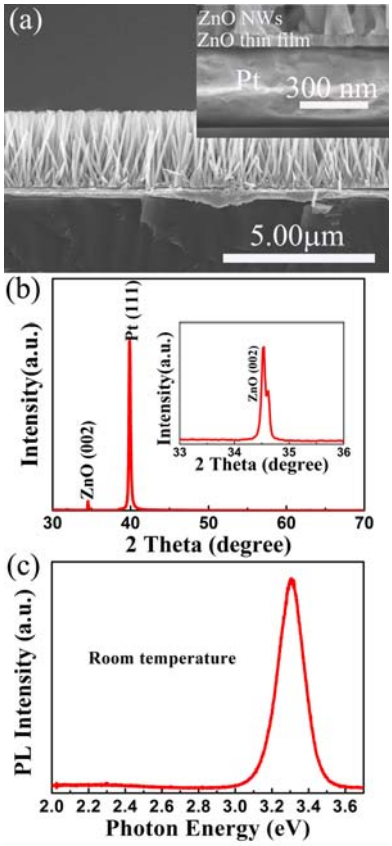

Fig 4.5 (a-c) SEM image, XRD pattern and RT PL spectrum for the ZnO NWs grown on Si (Pt) substrate. The inset of figure 1 (a) shows the cross-sectional SEM image of the Si, Pt and ZnO assisted layer. The inset of figure 1 (b) shows the magnified XRD pattern for the ZnO (002) peak.

In order to explore the stimulated emission from the ZnO NWs, the excitation power density dependent emission was performed using an optical parametric amplifier (OPA) in an active passive mode-locked femtosecond Ti: sapphire laser with the excited wavelength of the laser output of 350 nm at RT. The pump beam was focused on the NWs at an incident angle of 60° to the normal direction of the sample,

light emission was collected in the direction slightly deviated from the normal direction of the sample (detection angle of 5° to the normal direction). The excitation power density dependent PL emission spectra are shown in Fig 4.6 (a).

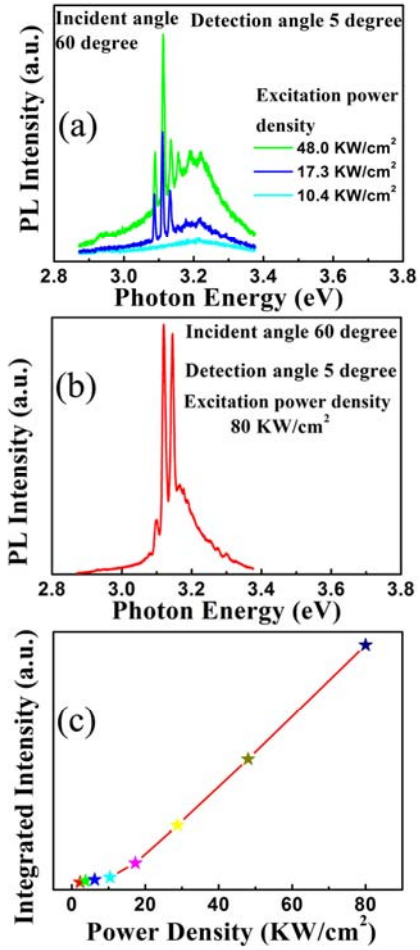

Fig 4.6(a-b) The evolution of the RT PL spectra in the ZnO NWs as the excitation density changing from 10.4 to 80 kW/cm^2 by a mode-locked femtosecond Ti: sapphire laser. (c) The corresponding integrated intensity of the stimulated emission as a function of the excitation power density.

At lower excitation power density of 10.4 kW/cm^2, the spectrum is comprised by a single broad spontaneous emission with FWHM of 0.11 eV, this spontaneous emission is 150 meV below the band gap and is generally ascribed to the recombination of excitons through an exciton-exciton collision process, where one of the excitons recombines to generate a photon.[83] When the power density exceeds the threshold of 17.3 kW/cm^2, three sharp peaks located at lower energy side with FWHM of 0.003 eV emerged on the broad spontaneous emission band. The linewidths of

these sharp peaks are <36 times smaller than the linewidth of the spontaneous emission peak below the threshold, and the observed mode spacing ~3 nm for ~3 μm long NWs, which agrees quantitatively well with the calculated spacing between adjacent resonance frequencies $v_F = c/2nl$, [84] where v_F is emission mode spacing, c is the speed of light, n is the refractive index, and l is the resonance cavity length. The cavity length could be calculated as ～3 μm. While the power density further increased to 48 kW/cm^2, four obvious sharp peaks were observed accompanied with increasing of the spontaneous emission intensity, as the pump power density increases, the gain becomes larger enough to enable cavity modes with higher loss to start lasing. Two strong sharp emission peaks located at 3.145 eV and 3.210 eV with FWHM of 0.006 eV were obtained as the excitation power density increased to 80 kW/cm^2 as shown in Fig 4.6 (b). The extended FWHM value could be due to the combination of the lasing modes. As shown in the Fig 4.6 (c), the integrated intensity L of the spectra increases superlinearly with the excitation density (I_{EX}). The dependence of L on I_{EX} can be fitted by $L \propto I_{EX}^2$, and the transitions from the spontaneous emission to lasing at 17.3 KW/cm^2 could be clearly observed. The narrow linewidth and the rapid increase of emission intensity indicate that stimulated lasing emission has occurred in the ZnO NWs. To realize the optically pumped lasing emission, the laser cavity is a definitive character for lasers. From the results reported by Z.K. Tang and P.D. Yang, we could conclude that the bottom and top planes of the ZnO NWs formed the natural FP lasing cavities. Since the refractive index of ZnO (2.45) is larger than that of air (1.0) and Pt (1.68), the well-faceted top surface of the small diameter ZnO NW (100 nm) serves as a mirror that defines an optical microcavity.

Obviously, the obtained lasing threshold in our experiment was further lowered in comparison with the previously reported values for random lasing in disordered particles (300 KW/cm^2), thin films and NWs (40 KW/cm^2). As we known, due to the intrinsic characteristics of ZnO, such as large exciton-binding energie and high optical gain, could contribute significantly to lower threshold, and the excellent microcavity will strongly increase the coupling efficiency of spontaneous emission into lasing modes, and thus help to reduce the threshold. [85] In our experiment the Pt layer was explored as one mirror for the laser, and the measured reflectivity for Si (Pt) sample is much larger than that for Si in the whole range from 2.0 eV to 3.4 eV as shown in Fig 4.7. The reflectivity for Si is 45.5% at the photon energy of 3.10 eV while that for Si (Pt) substrate is 69.3%, thus the threshold for the laser was further lowered in the ZnO

NWs grown on Si (Pt) substrate.

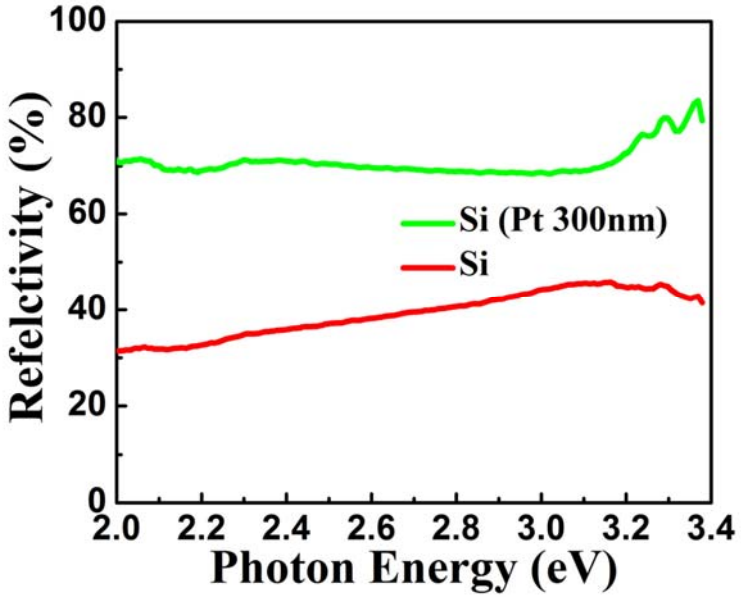

Fig 4.7 The reflectivity spectra of the Si and Si (Pt) substrates.

Like a conventional laser, laser emission direction measurement was also performed. As shown in Fig 4.8 (a, b), the laser emission intensity displayed an rapid decrease when changing the detection angle from 0° to 10° (the corresponding intensity decreased from 10^4 (a.u.) to almost zero) with incident angle of 60° and excitation power density of 80 KW/cm^2, thus we could conclude that these NWs form natural laser cavities with excellent emission direction owning divergence angle of 20°. It is also obvious to observe that there is a slightly laser peak position shift when changing the detection angle, this is due to that the laser cavity is formed by multiple NWs. The rocking curve shown in the Fig 4.9 indicats that the NWs are not well aligned (002) orientation (the corresponding FWHM is about 5.26°), and the main peak shifts to 10° from 17.2° (the well aligned ones), thus the strongest laser emission intensity was observed while the detection angle was located at 5° (deviated from the normal direction to the substrate).

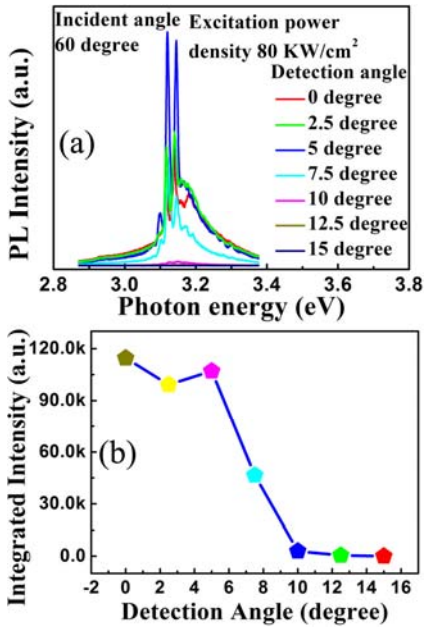

Fig 4.8 (a) The RT PL spectra in the ZnO NWs under different detection angles with the excitation power density of 80 kW/cm^2, (b) The laser divergence measurement curve.

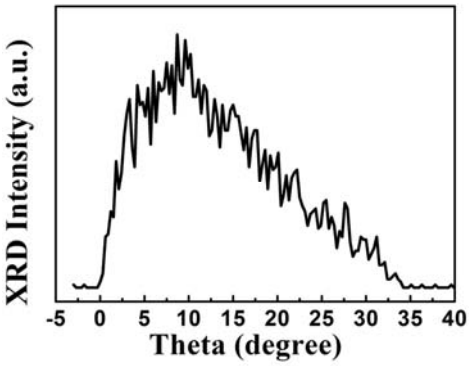

Fig 4.9 The XRD rocking curve of the ZnO NWs.

(4) **Supporting Information**

As shown in Fig 4.10 (a), the top agglomerate ZnO NWs were obtained while using Si (Pt thickness: 80 nm) substrate assisted with ZnO thin layer by hydrothermal method. The better oriented NWs were obtained using the same conditions except the thickness of the Pt layer was 300 nm as shown in Fig 4.10 (b). The corresponding inserted images show that the close contact between Si and Pt 80 nm thick layer has been formed, and there is an aperture between 300 nm thick Pt layer and Si substrate. Thus we could conclude that the stress between 300 nm thick Pt layer and Si substrate

could be released inducing the NWs with better growth orientation.

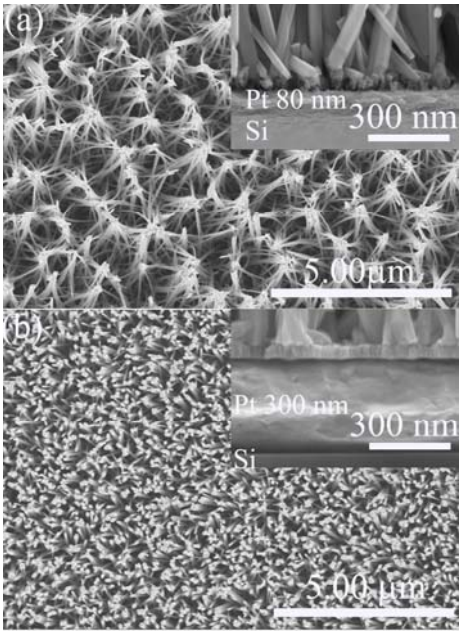

Fig 4.10 (a, b) SEM images of the ZnO NWs grown on Si (Pt thickness: 80 nm) and Si (Pt thickness: 300 nm) substrates, respectively. The inserted images show the corresponding cross-sectional SEM images for the Pt layer with different thickness.

The excitation power density dependent emission for the top agglomerate NWs grown on Si (Pt thickness: 80 nm) substrate was also performed using an optical parametric amplifier (OPA) in an active passive mode-locked femtosecond Ti: sapphire laser with the excited wavelength of the laser output of 350 nm at RT. The pump beam was focused on the NWs at an incident angle of 60° to the symmetric axis of the NWs, light emission was collected in the direction slightly deviated from the normal direction of the sample (detection angle of 5° to the normal direction). The excitation power density dependent PL emission spectra are shown in Fig 4.11 (a), only the spontaneous emissions were observed while changing the power density. Since the top agglomerate NWs owning random orientation, instead laser resonators could be formed by recurrent light scattering among multiple NWs. Since this kind of lasing emission needs much larger excitation power density as reported by others. Light emission direction measurement was also performed for obtaining the possible laser emission in the top agglomerate NWs, as shown in Fig 4.11 (b). Only the intensities of the spontaneous light emission changed with varying the detection angle.

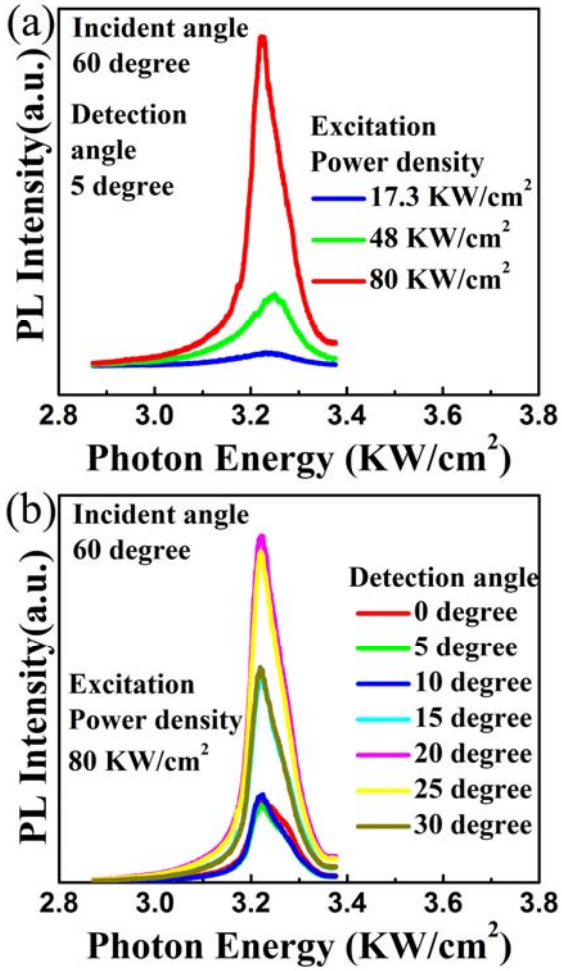

Fig 4.11(a) The evolution of the RT PL spectra in the ZnO nanowires grown on Si (Pt thickness: 80 nm) substrate as the excitation power density changing from 10.4 to 80 kW/cm^2 by a mode-locked femtosecond Ti : sapphire laser. (b) The RT PL spectra in the ZnO nanowires under different detection angles with the excitation power density of 80 kW/cm^2.

In the above experiments, aligned ZnO NW array was obtained on 1000 °C annealed ZnO seed layer by hydrothermal method. The optically pumped stimulated emission was obtained besides normal direction in these NWs, it is observed that the orientationof the NWs are important, the orientation of the mirrors are also important because they will change the direction of the output lasers; through adding a high reflectivity mirror on one side of the ZnO NWs, the threshold was further lowered, meantime the divergence angle of the laser was also performed, and the obtained value is 20°.

4.2 Electroluminescence for ZnO Based Devices

4.2.1 Electrically Pumped Single-Mode Lasing Emission of Self-Assembled n-ZnO Microcrystalline Film/p-GaN Heterojunction Diode

(1) Fabrication of n-ZnO Microcrystalline Film/p-GaN Heterojunction

For the fabrication of n-ZnO/p-GaN heterojunction, undoped n-ZnO was fabricated onto commercially available p-GaN (Mg doped) /sapphire substrate by a hydrothermal method using Zn-$(CH_3COO)_2 \cdot 2H_2O$ and $C_6H_{12}N_4$ as reactant sources. The hole concentration and mobility were 3.0×10^{17} cm^{-3} and 10 cm^2 V^{-1} s^{-1}, respectively, for p-GaN wafer. Prior to the growth the p-GaN /sapphire substrates were cleaned by organic solvents to remove contaminations. The p-GaN wafer was placed facing toward the bottom of the kettle during the growth in our case. The ZnO microcrystalline film was obtained through repeated growth for 6 times under the same conditions by the low temperature hydrothermal method. The ZnO microcrystalline film could form epitaxially on the GaN layer because of the lower mismatch between them. In the hydrothermal growth process the reaction solution was adjusted to identical concentration for both sources (0.01 mol /L). The reaction kettle was put into an oven and maintained at 90 °C for 16 h for each experiment. The obtained samples were rinsed by deionized water. Bilayer Ni /Au and monolayer In electrodes were employed as the contacts for the p-GaN wafer and n-ZnO layers, respectively.

(2) Characterization for n-ZnO Microcrystalline Film /p-GaN Heterojunction

The surface morphology of ZnO grown on p-GaN layer through 2 times, 4 times, and 6 times growth by the hydrothermal method are shown in Fig 4.12 (a-c), respectively. It is easy to observe that 2 times growth ZnO still displays hexagonal column morphology as shown in the inset of Fig 4.12 (a), and the formed ZnO merged each other after repeated growth. The connected web structures were obtained after 4 times growth shown in Fig 4.12 (b); the connected structure can be divided into different size hexagonal columns. The inset of Fig 4.12 (b) shows the typical combined interface of two hexagonal columns. The self-assembled ZnO microcrystalline film was formed after repeated growth for 6 times as shown in Fig 4.12 (c). The side surfaces of the most columns show natural combination morphology, and the top surface shows a smooth ZnO (001) facet illustrating high

crystalline orientation shown in the inset of Fig 4.12 (c).

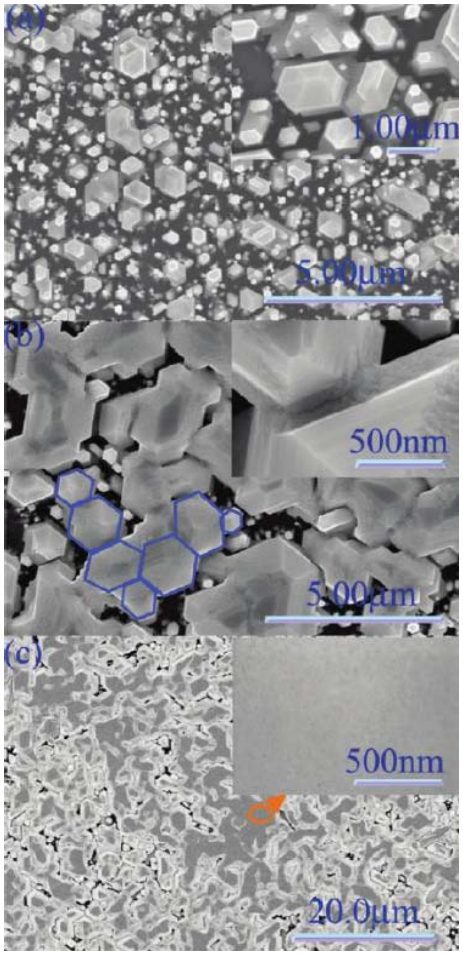

Fig 4.12 SEM images of ZnO samples grown on p-GaN wafer through 2 times (a), 4 times (b), and 6 times (c) by the hydrothermal method under the same conditions for each time growth, the insets of (a) and (b) show the magnified SEM images of 2 times and 4 times growth ZnO, respectively. The inset of (c) shows the top surface morphology as indicated by an arrow.

Fig 4.13 (a) shows wide range (30°-70°) X-ray diffraction (XRD) 2θ-scan of the ZnO microcrystalline film sample. As shown in the figure, only one diffractive peak located at 34.5° could be observed, which corresponds to the (002) direction of ZnO diffractive peak. This result indicates the ZnO microcrystalline film is of *c*-axis preferred orientation. Because the lattice parameters of ZnO and GaN are very close, a ω-scan was performed to identify the ZnO (002) and GaN (002) diffractive peaks. From the inset of Fig 4.13 (a) the (002) diffractive peaks originated from ZnO and GaN could be distinguished clearly with the corresponding narrow FWHM of 0.16°

and 0.12°, which reveals the good crystal quality of ZnO microcrystalline film.

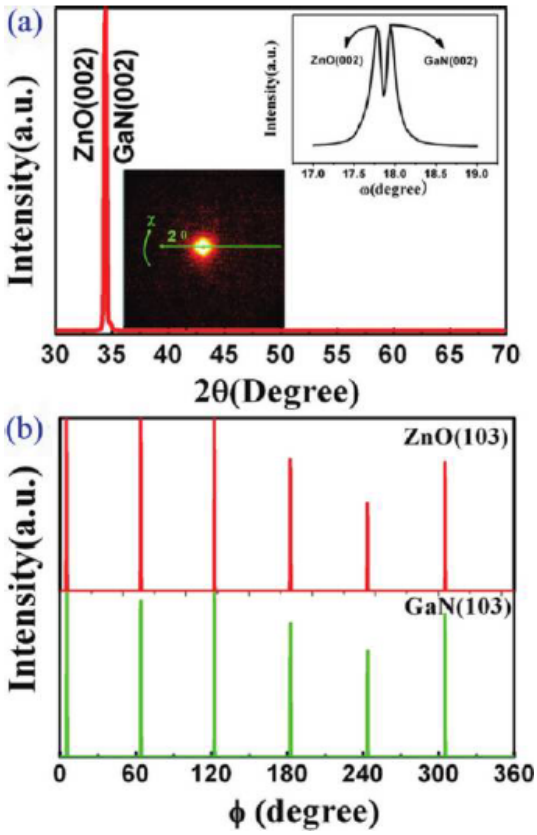

Fig 4.13 (a) Wide-range XRD 2θ-scan of the ZnO microcrystalline film grown on *p*-GaN /sapphire substrate. The upper trace of the inset shows XRD ω-scan curve of the ZnO microcrystalline film (002) pattern. The lower trace shows the corresponding 2D XRD image of the ZnO microcrystalline film grown on GaN wafer. (b) XRD ϕ-scans of the epitaxial ZnO microcrystalline film and GaN wafer.

The 2D-XRD image of the ZnO microcrystalline film is also shown in the inset of Fig 4.13 (a). The image of the film does not show any diffraction rings but gives a focused dot, which symbolizes the uniform in-plane atom alignment and the structural isotropy of the film. Fig 4.13 (b) shows the in-plane scan (ϕ-scan) orientation relationship between ZnO microcrystalline film and the GaN wafer. The well-defined peaks showing a 6-fold symmetry are obtained, which is consistent with the wurtzite crystal structure. The respective peaks of ZnO and GaN are at the same angle on the *c*-axis, which results in ZnO and GaN have an in-plane orientation relationship of $[103]_{ZnO} || [103]_{GaN}$. This result agrees well with the report from ZnO nanostructures on GaN by Kim et al.[86] The ϕ-scan spectrum implies the same crystal facets from different ZnO microcrystalline film are parallel to each other without any rotations.

Fig 4.14 shows the RT PL spectra of ZnO layers through 2 times, 4 times, and 6 times growth by the hydrothermal method on p-GaN wafer.

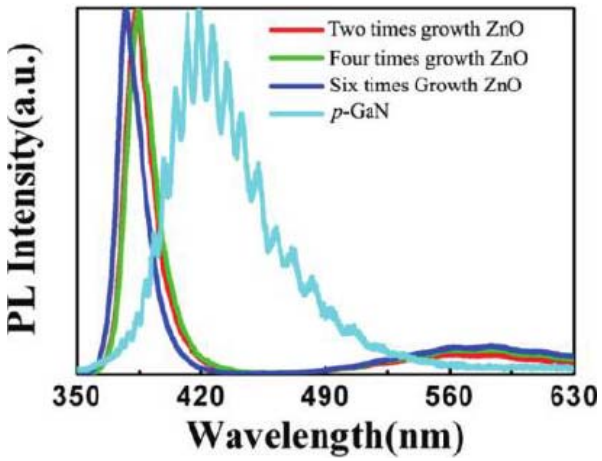

Fig 4.14 PL spectra of the ZnO samples and the p-GaN wafer.

As shown in the figure, the spectra of all the ZnO samples display a dominant sharp near-band-edge (NBE) emission at about 380 nm accompanied by a weak deep-level emission at around 550 nm. It is also obvious to find out that 6 times growth ZnO microcrystalline film displays a dominant sharp NBE emission at 377 nm while the UV peaks of the 2 times and 4 times growth ones are located at 383 nm, which may be due to the larger surface induced red shift. The PL spectrum of the p-GaN is dominated by a broad peak centered at about 420 nm, which is frequently observed in Mg-doped p-GaN corresponding to the transitions between conduction-band electrons or donors and Mg-related acceptors. [87] The fringes observed in the spectrum are due to the interference between GaN /air and the sapphire /GaN interfaces.

To make a diode, Ni /Au and In electrodes were used for p-GaN wafer and n-ZnO microcrystalline film, respectively. The ZnO layer is comprised by the merged hexagonal columns as shown in the device scheme of Fig 4.15 (a). Fig 4.15 (b) shows *I-V* characteristic of a heterojunction device; a nonlinear rectifying behavior is observed. The linear curve for Ni /Au on p-GaN reveals that good Ohmic contacts have been obtained in the electrodes. As reported everywhere, In metal can form good Ohmic contact to n-ZnO; from this point of view, we can conclude that the rectifying behavior of the LED originates from the n-ZnO microcrystalline film/p-GaN

heterojunction. Fig 4.15 (c) shows the ideal heterojunction band diagram for n-ZnO /p- GaN, which was constructed by following the Anderson model. [88] To construct the band diagram, the electron affinities (χ) of ZnO and GaN were assumed to be 4.35 eV [89] and 4.2 eV, [90] respectively. The band-gap energies (E_g) are 3.37 and 3.39 eV for ZnO and GaN at room temperature. As shown in the energy band diagram, the energy barrier ΔE_c for an electron is $\Delta E_c = \chi_{(GaN)} - \chi_{(ZnO)} = 4.2-4.35=-0.15$ eV, and the energy barrier ΔE_V for a hole is $\Delta E_V = E_{g\,(GaN)} + \Delta E_c - E_{g\,(ZnO)} = 3.39-0.15-3.37=-0.13$ eV. There are two energy band offsets due to the different electron affinities and the band gaps between ZnO and GaN.

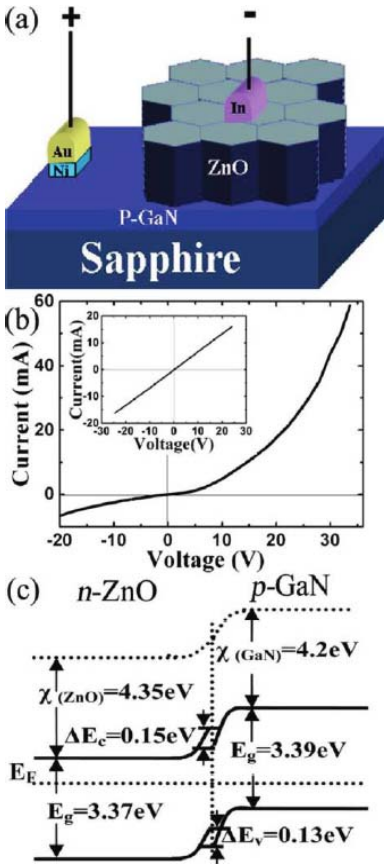

Fig 4.15(a) Schematic diagram of the ZnO microcrystalline film /p-GaN heterojunction, (b) *I-V* characteristic of the heterojunction showing a typical rectifying characteristic, the inset shows the *I-V* characteristic of Ni /Au contacts to p-GaN wafer. (c) Energy band diagram of the n-ZnO /p-GaN heterojunction under zero bias.

By applying a forward bias onto the heterojunction, the EL spectra are collected from the edge of the device at RT. As shown in Fig 4.16, an emission peak centered at around 530 nm due to the interfacial recombination could be observed under lower

driven current of 0.5 mA; a UV emission peak located at 383 nm appeared for a small portion of holes that are injected into n-ZnO from the p-GaN side with increasing the current to 1 mA. The UV emission peak becomes dominated and shifts to 392 nm accompanied by weak visible emission when the current further increased to 3 mA. A slight shift of peak position could also be observed with further increasing the injection current. This red shift is due to the band p emission under high injection current as often observed in optical pumped emission in ZnO. These results imply the recombination zone of EL emission is mainly in ZnO, and the dominated UV EL emission peak could be attributed to the band edge emission from ZnO under lower forward injection current.

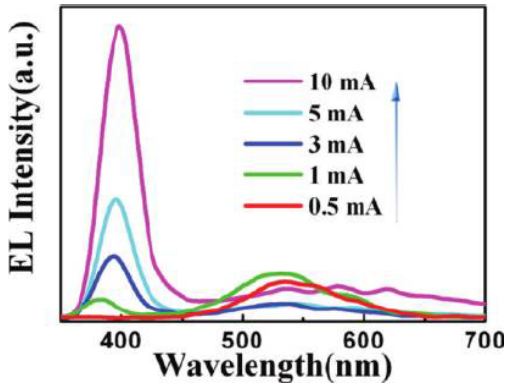

Fig 4.16 EL spectra of the n-ZnO microcrystalline film /p-GaN heterojunction under lower forward injection current.

With increasing the applied current to 36 mA, the emission peak red-shifts to the longer wavelength side. The thermal effect can also induce this kind of phenomenon as reported by Yu et al. [91] Moreover some very sharp peaks superimposed on a broad emission are observed (Fig 4.17 (a)). These sharp emission peaks become more clearly with further increasing the driven current. At 46 mA a single-mode lasing emission peak centered at 407 nm with FWHM of 0.7 nm is detected. The dependence of the integrated emission intensity on the injection current is shown in the inset of Fig 4.17 (a), from which a threshold of 36 mA could be obtained. When the applied current exceeds this point, the emission intensity increases nonlinearly. The sharp emission peak with the narrow FWHM, the threshold, and the clear emission mode imply that the electrically pumped single mode lasing action has been realized in n-ZnO microcrystalline film /p-GaN heterojunction diode. Fig 4.17 (b) shows the EL spectra detected from the edge and the top surface of the diode at an applied current of

46 mA. The spectrum recorded from the top surface shows only a weak and broad UV emission, while a lasing action could be observed from the edge, which indicates the laser cavity may be formed directionally parallel to the substrate.

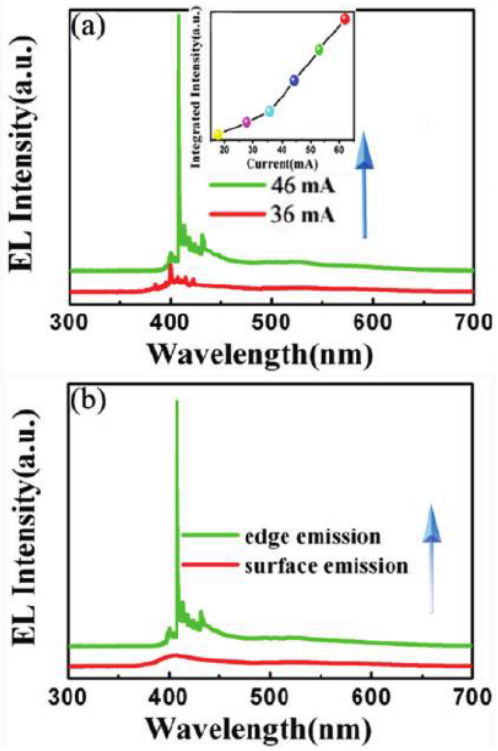

Fig 4.17(a) Single mode lasing emission for the n-ZnO microcrystalline film /p-GaN heterojunction was obtained under higher forward injection current of 46 mA. The lasing effect is evident when the injection current exceeds 36 mA; the integrated EL intensity as a function of the injection current is shown in the inset. (b) The surface and the edge EL spectra of the diode under the same injection current of 46 mA.

To realize electrically driven lasing, the efficient carrier accumulation and the laser cavity are essentials. Because of $\Delta E_V < \Delta E_c$, larger ΔE_c blocks the escape of the majority carriers (electrons) in ZnO; meanwhile, the majority carriers (holes) in GaN could be efficiently injected into ZnO under forward bias. The injected holes from GaN into ZnO could recombine radiatively with the electrons in ZnO microcrystalline film. The self-assembled ZnO microcrystalline film in our case owns excellent crystal quality, and ideal interface can be formed due to the ZnO was freely synthesized by the low-temperature hydrothermal method.

Another key point to realize lasing action is the laser cavity formation. From the ϕ-scan spectrum and SEM images it could be deduced same crystal facets from

different ZnO microcrystalline film are parallel to each other without any rotations. Since the refractive index of ZnO (2.45) is larger than that of air (1.0), the parallel side-facets of the close packed ZnO microcrystalline film may serve as a mirror to form the laser cavities naturally.

(3) Supporting Information

Fig 4.18 (a) shows the edge emission spectrum of one n-ZnO microcrystalline film / p-GaN heterojunction laser diode under a forward injection current of 40 mA, from which we can observe a regular laser modes spaced with 6 nm. Fig 4.18 (b-c) shows the electrically pumped single mode lasing emission spectra obtained from other self-assembled n-ZnO microcrystalline film /p-GaN heterojunction diodes under higher forward injection current.

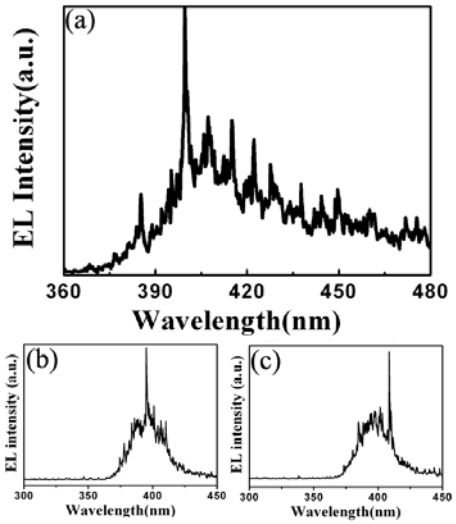

Fig 4.18 (a-c) EL emission spectra of ZnO microcrystalline film/p-GaN heterojunctions.

4.2.2 Ultralow Driven Current of ZnO Based LED

(1) Fabrication of LED Devices

For fabrication of *n*-ZnO/*i*-MgO/*p*-GaN LED, 10 nm-thick MgO film is prepared with magnetron sputtering method using Mg target with purity of 99.999%, and then 20 nm-thick ZnO film is grown by magnetron sputtering using ZnO target with purity of 99.999%, before loading into the sputtering chamber, p-GaN wafer/sapphire substrate was cleaned using organic solvents to remove the surface contamination, during the sputtering process, a mixture of Ar and oxygen gases with the same flow rate of 20 SCCM was introduced into the growth chamber, and work pressure was

maintained at 1 Pa, the growth of MgO and ZnO was sputtered at RT, but the time for the growth of MgO and ZnO were 10 and 20 min, respectively. For the preparation of *i*-polymers inserted LED, a thin layer of negative photoresist with thickness of 10 nm was spin coated *p*-GaN layer with rotation speed of 7000 rpm, and then hydrothermal method was explored to prepare ZnO NWs using Zn-$(CH_3COO)_2 \cdot 2H_2O$ and $C_6H_{12}N_4$ as reactant sources, In the hydrothermal growth process the reaction solution was adjusted to identical concentration for both sources (0.01 mol/L). The reaction kettle was put into an oven and maintained at 90 °C for 16 h for each experiment. The obtained samples were rinsed by deionized water. To fabricate LEDs, Ni/Au electrodes was prepared on *p*-GaN wafer by vacuum thermal evaporation method, and then prepared electrodes were annealed in air at 450 °C for 5 min, In metal was used as electrodes for ZnO.

(2) Characterization for LED Devices

As shown in Fig 4.19, when the MgO thin layer is deposited on the *p*-GaN wafer, the epitaxial ZnO NWs are aligned along the vertical direction assisted with ZnO thin film in a large scale. The average diameter of the hexagonal ZnO NWs is about 300 nm shown in the inset of Fig 4.19 (a). Meanwhile, as shown in Fig 4.19 (b), when the polymer was spin-coated on the *p*-GaN wafer, the obtained ZnO NWs have a random distribution with the average diameter of about 300 nm likewise. To explore the crystalline quality of the as-grown ZnO NWs, the RT PL spectra for ZnO NWs were performed (Fig 4.19 (c)). For ZnO NWs grown on different substrates, the PL spectra are almost the same, which show a dominant sharp NBE emission at 388 nm with FWHM of 16 nm accompanied with a weak deep-level emission at around 560 nm. The PL spectrum of *p*-GaN is also dominated by a broad peak centered at about 420nm.

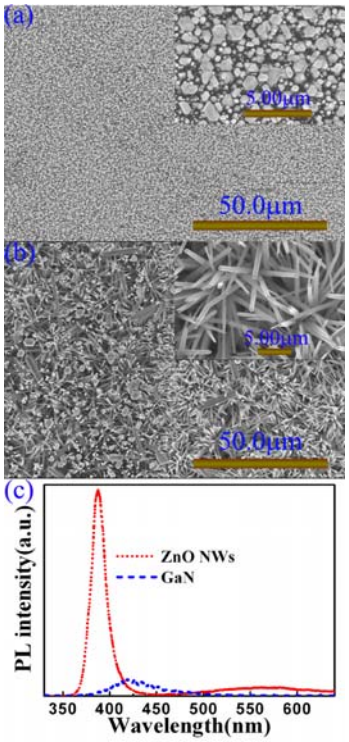

Fig 4.19 (a, b) SEM images of ZnO NWs prepared on *p*-GaN wafer with *i*-MgO and *i*-polymer thin layers inserted, respectively, their magnified SEM images are shown in the inset. (c) PL Spectra of ZnO NWs and *p*-GaN.

The schematic diagram of the fabricated *n*-ZnO/*i*-layer/*p*-GaN heterojunction LED is shown in Fig 4.20 (a), the Ni/Au and In metals were used as electrodes for *p*-GaN wafer and *n*-ZnO nanostructures, respectively. Fig 4.20 (b) shows the RT I-V characteristics of the *n*-ZnO NWs/*i*-MgO/ *p*-GaN and *n*-ZnO NWs/ *i*-polymer/*p*-GaN heterojunction LEDs. The *i*-MgO layer inserted LED demonstrates a nonlinear behavior with a similar forward turn-on voltage as that of the *i*-polymer inserted one. The I-V curve of the *n*-ZnO NWs/ *i*-polymer/*p*-GaN heterojunction LED shows a typical back to back diode, the polymer layer acts as double Schottky diodes. Meanwhile, the injection current is much lower for the polymer inserted LED due to the polymer can be regarded as electron and hole blocking layer. The linear curve in the inset for Ni/Au on *p*-GaN reveals good Ohmic contacts have been formed in the electrodes. In metal can form good Ohmic contact with *n*-ZnO as reported everywhere. Therefore, the nonlinear behavior of the LEDs is considered originated from the *n*-ZnO NWs/ *i*-layer/*p*-GaN.

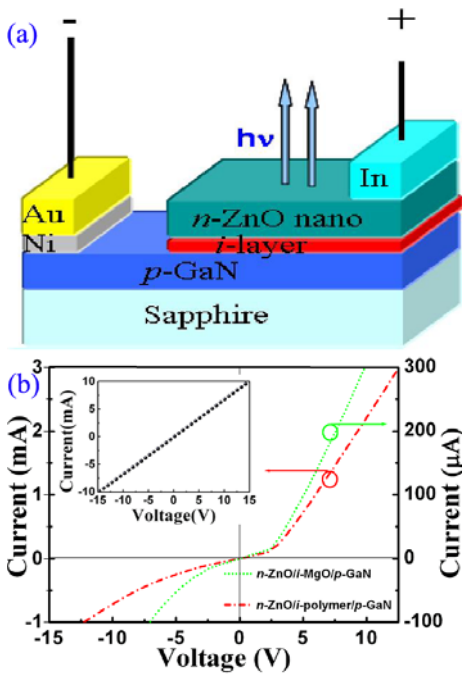

Fig 4.20 (a) Schematic diagram of *n*-ZnO nanostructures/*i*-layer/*p*-GaN heterojunction LED. (b) Current-voltage characteristics of *n*-ZnO/ *i*-MgO/ *p*-GaN and *n*-ZnO/ *i*-polymer/*p*-GaN diodes, respectively. The inset shows current-voltage characteristic of Ni/Au Ohmic contact to the *p*-GaN.

The EL spectra of the *n*-ZnO NWs/*i*-MgO/ *p*-GaN and *n*-ZnO NWs/ *i*-polymer/*p*-GaN heterojunction LEDs are shown in Fig 4.21 (a). The EL spectra of MgO inserted LED display a blue emission located at 420 nm and a broad orange-yellow defects related emission. By comparing the PL spectra, it can be easily identified that the 420 nm emission originates from the transition in *p*-GaN layer. The broad emission band from 500 to 700 nm can be ascribed to the defects related emission in ZnO, which may be due to the interfacial defects formed among ZnO, MgO, and GaN. The emission origins will be further discussed in the following. The EL intensities for blue and defects related emissions are almost in the same order under a low forward injection current of 1.93 mA. With increasing the injection current to 3.36 mA, the blue EL emission dominates the spectrum accompanied with the relatively weak defects related emission. As shown in Fig 4.21 (b), the *n*-ZnO NWs/ *i*-polymer/*p*-GaN LED exhibits the UV-blue emission located at 400 nm with weak defects related emission. The UV-blue emission peak which overlapped with the PL emission bands of ZnO and GaN can be considered as compound radiative transitions originated from ZnO, GaN, and the interface. The most obvious

characteristic is that the UV-blue emission could be detected under an ultra low driven current of 25 μA, which is almost one order of magnitude lower than all the reported driven current data. With increasing the injection current to 330 μA, the EL emission peak position is unchanged and the corresponding intensity increases quickly. The photoimages of EL emission from the devices shown in the inset of Fig 4.21 illustrate clearly the above results.

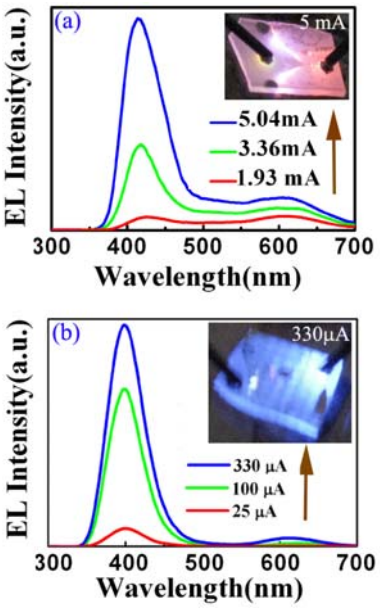

Fig 4.21 RT EL spectra of (a) *n*-ZnO/ *i*-MgO/ *p*-GaN and (b) *n*-ZnO/ *i*-polymer/*p*-GaN LEDs under different forward injection current, the inserts show the corresponding EL images.

To further understand the originations of the EL emissions, the EL emission spectra are analyzed by Gauss fittings. The corresponding transitions are illustrated by the energy band diagram for the better understanding. For each EL emission band the fitted four emission peaks could be obtained. As displayed in Fig 4.22 (a), the EL spectrum of the *n*-ZnO NWs/ *i*-MgO/ *p*-GaN LED under injection current of 5.04 mA can be divided into four individual peaks by the Gauss analysis. According to the reported results by other groups, [92,93] the fitted EL emission bands located at 404, 430, 487, and 602 nm could be attributed to the transitions from the conduction band edge of ZnO to the acceptor level of GaN, from the donor level ED in ZnO to the acceptor level E_A in GaN, from the conduction band of ZnO to the defects level E_d in ZnO, from the donor level E_D to the defects level E_d in ZnO as shown in Fig 4.22 (b), respectively. For the *n*-ZnO NWs/ *i*-polymer/*p*-GaN LED the main emission peak of

the EL spectrum under injection current of 330 μA is comprised of a UV emission at 385 nm and a blue emission at 404 nm shown in Fig 4.22 (c). The EL emission located at 385 nm is ascribed to the NBE excitonic emission in ZnO NWs as shown in Fig 4.22 (d). The weak EL emission at 584 nm could also be attributed to the transition from the donor level E_D to the defects level E_d in ZnO, the defects related emission is always a broad peak as reported everywhere. Another obvious characteristic is that the ratio of the UV emission intensity to that of the defects related emission for the polymer inserted LED is always much larger than that of the MgO inserted one with increasing injection current. From this point of view, the interface defects for the polymer inserted LED are much less than those for the MgO inserted one.

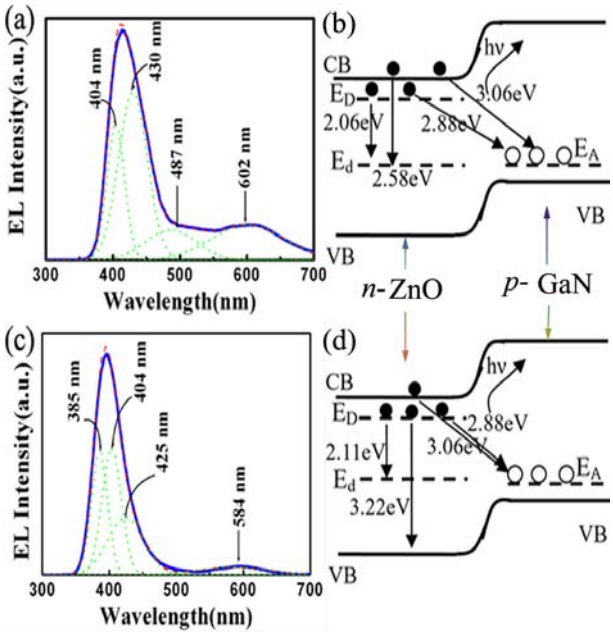

Fig 4.22 (a and c) The EL spectra and the Gauss analysis curves of *n*-ZnO/ *i*-MgO/ *p*-GaN LED and *n*-ZnO/ *i*-polymer/*p*-GaN LED, respectively, (b and d) The corresponding energy band diagrams and transition processes responsible for the EL spectra.

The results of Chen *et al.* showed that for the ZnO thin film/*i*-layer/*p*-GaN heterojunction the thickness of the *i*-layer determined the recombination zone in the LED. [94] With the thicker *i* layer the recombination zone preferred at the ZnO side because of the efficient electron blocking property. In our experiment, the *i*-layers were quite thin, which was proposed to simulate the different interface properties between ZnO and GaN. By overall analysis of our experiment results and other

reports for the ZnO/GaN heterojunction LED, the following conclusion could be drawn: (1) Because the electron mobility in ZnO is much higher than the hole mobility in GaN, the electrons have the high probability to transit from ZnO to GaN side through the interface or the thin *i* layer resulting the radiative recombination in GaN. (2) The EL emission of the heterojunction LED is the compound transitions composed with different originations from ZnO, GaN and the interface. Due to the above two reasons, the EL spectra of ZnO/GaN heterostructures always show a broad emission band located in the UV-blue to visible regions and the dominated EL emission peaks are governed by the electronic properties of ZnO and GaN layers and the carrier blocking ability of the interfaces.

The results also showed carrier blocking ability of the *i*-polymer is better than MgO, which induced the excitonic related EL emission of ZnO presented in the EL spectra. The other advantage of the polymer inserted LED is that the low driven current (microampere magnitude), compared with the tens or even several hundreds milliamperes threshold current for the ZnO/GaN LEDs reported by many papers. [93-98] The photoresist is usually used as an insulating layer in LEDs. There are no reports about the luminescence from the photoresists. For the low-driven current property of the heterojunction LED, we believe the *i*-polymer plays an important role in the device. According to literatures, although the values of ΔEc are as high as 3.0 eV, [99,100] the *i*-layers, such as SiO_2, AlN, and MgO, could not confine the electrons efficiently due to the mismatch, dislocation and stress that could be easily formed. For the *i*-polymer inserted LED, ideal interfaces could be built for the well flexible properties. As a result, the dominant EL emission peaks are located at around 400 nm with a quite broad FWHM, which means the electrons could tunnel into the GaN layer and obtain radiative recombinations with holes. As a contrast, the *i*-polymer used in our experiment showed a better block for both of the carriers, which induced a quite low current under the same voltage compared with the MgO inserted device. For the *n*-ZnO/*i*-polymer/*p*-GaN LED, the carriers could accumulate at the different interfaces by applying a forward voltage. When the electronic field applied on the devices is high enough, the carriers could tunnel through the thin polymer layer to generate luminescence with different emitting centers. Due to this reason the driven current is quite low for the *n*-ZnO/*i*-polymer/*p*-GaN LED. Considering the life time of the *n*-ZnO/*i*-polymer/*p*-GaN LED, the similar EL results were obtained through continuous EL measurements (1 h per time, two times per week) during two months.

In the above experiments, ZnO microcrystalline film was prepared on GaN template through multi-time growth by hydrothermal method, electrically pumped single mode laser emission of heterojunction was obatined by EL measurement, and further research is needed; using i-polymer as carrier blocking layer ultralow driven current heterojunction light emission device was realized, the UV-blue light emission located at 400 nm was obtained.

4.3 Conclusion

This chapter is mainly focused on the fabrication of different kinds of light emission devices：optically pumped ZnO lasers, electrically pumped single mode laser and ultralow current driven light emission diode. The corresponding light emission mechanisms have been discussed.

1. Aligned ZnO NWs was prepared by the low temperature hydrothermal method assisted with ZnO thin film, the stimulated emission were obtained with threshold of 96 KW/cm^2 excited by femtosecond laser in the optically pumped ZnO NWs; Further lowered threshold laser was realized in the ZnO NWs fabricated on Si (Pt) substrate assisted with ZnO thin layer. The threshold of this laser is 17.3 KW/cm^2. The reasons for the low threshold besides the microcavities formed in the well faceted ZnO NWs as well as the large exciton binding energy and high optical gain, another characteristic we explored here the higher reflectivity of Pt layer as mirror. The observed laser with excellent emission direction owning divergence angle of 20° was realized. Based on our experiment we believe that further lowered threshold, direction controlled laser will be realized exploring higher reflectivity mirrors in the well aligned ZnO NWs with parallel side surfaces in periodic arranged structure.
2. The electrically pumped single-mode lasing emission operating at room RT has been realized based on the self-assembled ZnO microcrystalline film prepared on the p-GaN template. The self-assembled ZnO could form an excellent interface with GaN wafer benefiting the holes injection from GaN to ZnO, a single-mode lasing emission located at 407 nm with FWHM of 0.7 nm was observed. The reason for the red shift of the lasing emission peak may be due to the thermal effect; we believe that electrically pumped single mode lasing emission located at the shorter wavelength for the

self-assembled ZnO/p-GaN heterojunctions could be realized under optimal conditions. Using the polymer as the *i*-layer in *n*-ZnO NWs/*p*-GaN heterojunction LED the device showed a dominated UV-blue EL emission with very low driven current of microampere magnitude. By analyzing the EL spectra carefully, it is believed the originations of EL emission were the compound radiative transitions between ZnO and GaN layers. Ultralow driven current LED devices resulting in less thermal effects may have potential application prospects.

Chapter 5 ZnO Based Photodetectors

The last chapter introduces some initial studies on optically, electrically pumped ZnO lasers and ultralow current driven light emission devices, this chapter will discuss some research related to ZnO photodetectors (PDs).

5.1 Visible and Ultraviolet Light Alternative Photodetector Based on ZnO Nanowires/n-Si Heterojunction

5.1.1 Device Fabrication

In this work, we adopted a direct current (DC) and RF cosputtering method to prepare closely packed ZnO NW arrays. *n*-type Si (100) was used as a substrate. Interestingly, we succeeded in making a ZnO NWs/*n*-Si heterojunction photodiode, which can detect either visible or UV light by applying forward or reverse bias on the device.

The cosputtering method includes a DC magnetron sputtering of a 99.999% pure Zn target under a power of 70 W and a RF magnetron sputtering of a 99.9% pure ZnO target under a power of 20 W. Before being loaded into the sputtering chamber, the Si substrate was cleaned by organic solvents and etched in dilute HF acid to remove the contaminations and surface oxides. During the sputtering, a mixed gas of oxygen and argon with the same flow rate of 20 SCCM was introduced into the chamber and the working pressure was maintained at 1 Pa. The substrate was kept at 400 °C with a rotation speed of 20 loops/minute and the growth time was 2 h. To make devices, 100 nm thick Au film was deposited on the ZnO NW arrays and 100 nm thick Al film was deposited on the back side of the *n*-type Si substrate as electrodes using evaporation method.

5.1.2 Characterization of the Device

Fig 5.1 (a) shows the cross-sectional image of the ZnO NW arrays prepared on the Si (100) substrate at 400 °C by the dc and RF cosputtering method. It reveals that all the ZnO NWs grow vertically on the substrate. The surface morphology of the

ZnO NW arrays shown in Fig 5.1 (b and d) proves that the NWs are closely packed. From the magnified cross-sectional image in Fig 5.1 (c), the length of the ZnO NWs can be measured to be about 500 nm. Also the root diameter of each single ZnO NW is smaller than the top diameter. The average diameter is determined to be about 40 nm. The EDX data shown in Fig 5.1 (e) indicate that the sample consists of O and Zn elements with more O atoms. The XRD pattern of the ZnO NW arrays prepared on the Si (100) substrate is displayed in Fig 5.1 (f). The diffraction peak of the sample can be indexed to that of hexagonal wurtzite ZnO. Only the (002) diffraction peak and the Si (400) can be observed, which indicates that ZnO NWs are with perfect *c*-axis orientation. The FWHM of the diffraction peak is 0.177°, suggesting the good crystallinity of the ZnO NW arrays. The detailed growth process of ZnO NWs will be discussed elsewhere.

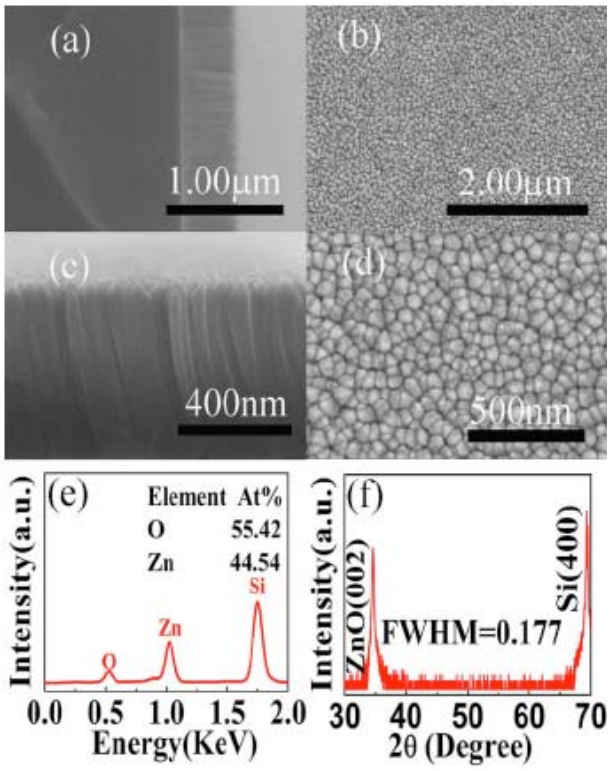

Fig 5.1(a) Cross-sectional SEM image of the ZnO NW arrays fabricated on Si substrate, (b) Top view image of the ZnO NW arrays, (c) Magnified cross-sectional SEM image of the ZnO NW arrays, (d) Magnified surface image of the ZnO NW arrays. (e) The EDX spectrum shows the composition of Zn and O element. (f) The XRD pattern of the ZnO NW arrays fabricated on the Si (100) substrate.

The PD structure is sketched in Fig 5.2 (a) Au and Al were used as electrodes for ZnO and Si, respectively. When a forward bias was applied on the ZnO side, the *I-V* characteristic shown in Fig 5.2 (b) (black color) exhibits a good rectifying behavior with rectification ratio ($I_{forward}$ / $I_{reverse}$) of above 1.6×10^{2} at 4 V in the dark, indicating the formation of a diode. The rectification ratio is much larger than that (~24) of molecular beam epitaxy grown ZnO-based heterojunction observed by Mandalapu *et al.*, [101] which indicates that the electrical property of our magnetron sputtering heterojunction is quite good. The turn-on voltage and the reverse leakage current are found to be 2.58 V and 1.17×10^{-7} A (at -4 V), respectively. For the heterojunction, the current increases exponentially following the equation, $I\sim\exp(\alpha V)$, which is usually observed in the wide band gap *p-n* diodes due to recombination-tunneling mechanism. [102,103] The constant α was evaluated to be 1.169 V^{-1} by fitting the experimental data in Fig 5.2 (b) (shown in red color), which falls in the range of 0.45–1.50 V^{-1} for the semiconductor junctions, as suggested by Fedison *et al.*[101] The *I-V* characteristics between two as deposited gold contacts on ZnO NW arrays is linear, indicating the formation of Ohmic contacts (Fig 5.2 (c)).

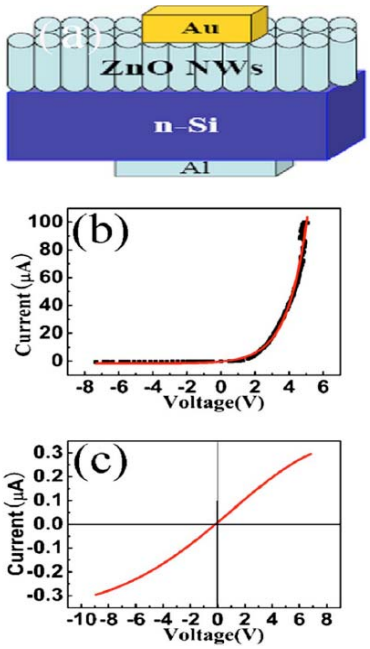

Fig 5.2(a) The schematic of the ZnO NW array/*n*-Si heterojunction. (b) *I-V* curve (black color) of the ZnO NW array/*n*-Si heterojunction, the red color shows the fitting result. (c) *I-V* characteristics between two gold contacts on the ZnO NW arrays.

Fig 5.3 shows the photocurrent spectra of the heterojunction irradiated from the ZnO NW array side when applying forward (red color) and reverse biases (green color). Interestingly, we only observed visible light response under forward bias and UV response under reverse bias. The wavelength of the decreasing edge under forward bias is about 375 nm, which corresponds to the cut off wavelength under reverse bias. The photoresponse mechanism of this heterojunction can be understood in terms of the energy band diagram based on Anderson's model [104] and the carrier diffusion process, as shown in Fig 5.4 (a). The band gap and electron affinity values are $E_{g\ ZnO}$=3.37 eV and χ_{ZnO}=4.35 [105] for ZnO and $E_{g\ Si}$=1.12 eV and χ_{Si}=4.05 [105] for Si, respectively. The model shows a small conduction band offset (0.3 eV) and a large valence band offset (2.54 eV). To understand the different spectral responses under forward and reverse biases, the energy band diagrams of the junction were also displayed in Fig 5.4 (b and c).

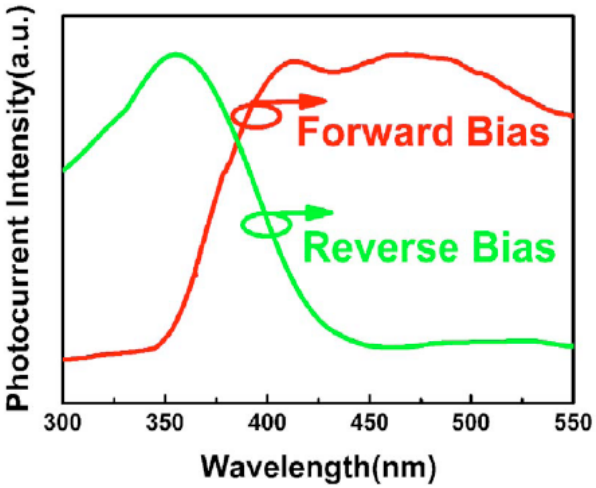

Fig 5.3 Photocurrent spectra of the ZnO NW array/*n*-Si heterojunction when applying forward bias (red color) and reverse bias (green color), respectively.

When a forward bias is applied on the ZnO NW array/*n*-Si heterojunction, the energy band diagram is described as in Fig 5.4 (b). In this case, a visible light arriving at the junction will pass through the ZnO layer and be absorbed in the underlying *n*-Si to generate *e*-*h* pairs. These photogenerated electrons will pass through the barrier and drift toward ZnO side driven by the applied bias. Owing to the small conduction band offset value, a photocurrent signal can be obtained. When the heterojunction is illuminated by UV light, photons will be absorbed by the NWs, generating carriers in

the ZnO layer. The generated electrons are confined in the ZnO layer by the electric field. The generated holes cannot drift toward Si side to form current for its low mobility and short lifetime. Furthermore, it is easy to form a thin SiO_2 layer between Si and ZnO NW arrays at the beginning of the sputtering process as reported by Tan *et al.* [106] which can easily block the movement of the holes. Therefore, no photocurrent signals will be detected in this case. Although the formed thin SiO_2 layer may also block the electrons under forward bias when a visible light irradiates, the much larger tunneling probability for electrons makes the heterojunction with good photoresponse. We find a fast decrease in photocurrent in the range of 400–350 nm because of the strong absorption of ZnO NW arrays.

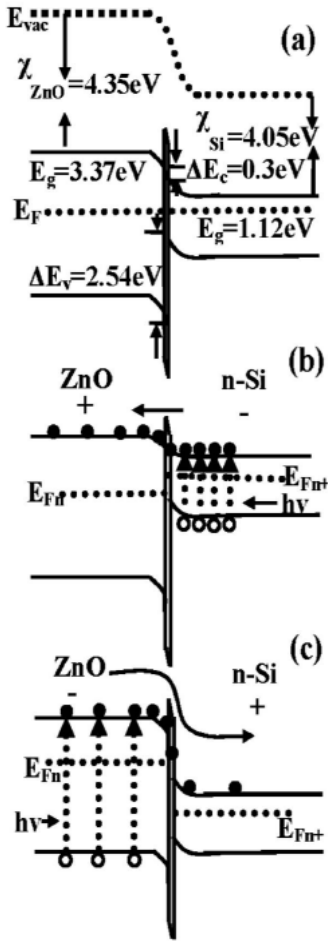

Fig 5.4 The energy band diagram of the ZnO NW array/*n*-Si heterojunction under zero bias (a), forward bias (b), and reverse bias (c), respectively.

When the junction is negatively biased (a positive bias is applied on the Si side), the energy diagram is shown in Fig 5.4 (c). The visible light-generated electrons in Si cannot drift toward ZnO side owing to the reverse bias. The photogenerated holes are confined in the Si side because of the large valence band offset. As a result, no photocurrent is observed for visible light excitation. When an UV light shines on the junction, the ZnO NWs will absorb the light and generate electrons and holes. Since the undoped ZnO usually exhibits a *n*-type conductivity, the photon-generated electrons will easily drift toward Si side, giving good photoresponse signal in the UV band.

It is found out that different wavelength light can be detected combining materials with different band gaps, and thus the tradition of preparing only one kind of material on the substrate for detection is broken up.

5.2 Short Wavelength Cut-off for ZnO Based n-Nanowires/i-Thin Film/n-Nanowires Photodetector

5.2.1 Device Fabrication

The intrinsic (*i*)-ZnO thin film was fabricated by RF magnetron sputtering method using a 99.999% pure ZnO target under a power of 130 W. Before being loaded into the sputtering chamber, the glass substrate was cleaned by organic solvents and rinsed by deionized water to remove the contaminations. During the sputtering process, a mixed gas of oxygen and argon with the same flow rate of 20 SCCM was introduced into the chamber and the working pressure was maintained at 1 Pa. The substrate was kept at RT with a rotation speed of 20 loops per minute and the growth time was 1 h. A hydrothermal method was explored to grown *n*- ZnO NWs on *i*-ZnO thin film using $Zn(CH_3COO)_2 \cdot 2H_2O$ and $C_6H_{12}N_4$ as reactant source. The reaction solution was adjusted to identical concentration (0.01 mol/L). Then the reaction kettle was put into an oven and maintained at 90 °C for 16 h. Finally, the obtained sample was rinsed by deionized water and dried in the oven. Au particles were deposited on the surface of the ZnO NWs for 1 minute using an ion-sputtering method. To make devices, two In metal spots with a distance of 2 mm were used as electrodes for the NWs.

5.2.2 Characterization of the Device

Fig 5.5 (a) shows the schematic diagram of the PD using *n*-ZnO NW array

fabricated on glass substrate assisted with *i*-ZnO thin film. Fig 5.5 (b) shows the typical current versus voltage (I-V) characteristics of the as grown *n*-ZnO NWs based PD device in the dark and under UV illumination focused around one electrode from NWs side, the I-V curve is linear for as grown PD in the dark, which indicates good ohmic behavior for the contacts between ZnO NWs and electrodes. Under the illumination of 380 nm, the current increased greatly compared with the dark current under the same voltage. The I-V measurements for the ZnO NWs based PD in the dark and under UV illumination focused on the NWs side were obtained using Hall measurement system. A Xe lamp was used as the illumination source. The experiments were performed on ZnO based devices in standard ambient conditions. The photoresponse mechanism for ZnO nanostructures are commonly explained by the surface absorption and desorption processes of oxygen. As oxygen molecules are easily adsorbed on the oxide surface because of the surface defects, the free electrons can be captured by the adsorption of oxygen to generate the electronegative oxygen ($o_2 + e^- \rightarrow o^{2-}$), then, a low-conductivity depletion layer is formed near the surface. Upon illumination with the photon energy above band-gap of ZnO, electron-hole pairs are generated ($hv \rightarrow e^- + h^+$), the holes could be trapped close to the NWs surface by the adsorped electronegative oxygen. Due to this reason, the probability of the unpaired electrons recombined with holes is decreased greatly, which induces the photocurrent increases a lot. [107] This hole-trapping mechanism through oxygen adsorption and desorption in ZnO NWs could be affected by the density of trap states formed by the dangling bonds on the NWs surface. Any detrimental recombination that occurs at the surface will reduce the magnitude of photocurrent. [108] It is also obvious to find that photocurrent curves for the PD is not linear under illumination of 380 nm. The asymmetrical *I-V* curves of ZnO NWs were also presented by other reports. [109-111] However, the origins of the rectifying *I-V* characteristic are still under debate. Here, we propose that the nonlinear characteristics may mostly originate from the effective carrier concentration resulting in the contact barrier. The intrinsic carrier concentration for the ZnO NWs can be as high as 6.1×10^{18} cm^{-3}, [112] and the measured carrier concentration for the ZnO thin film in our case is 5×10^{16} cm^3. The NWs-thin film-NWs could be considered as an *n-i-n* structure, quasi ohmic contacts could be formed between NWs and thin film in the dark. However, a barrier between NWs and thin film could be built under UV illumination on the NWs side.

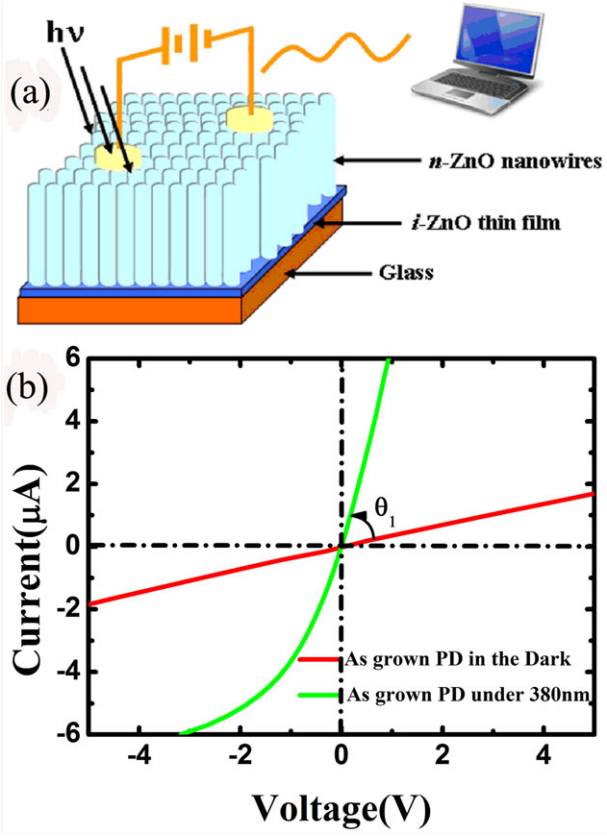

Fig 5.5 (a) The schematic diagram of the ZnO NWs based PD. (b) I-V characteristic curves of the as grown ZnO NWs based PD in the dark and under UV illumination of 380 nm, respectively.

Fig 5.6 (a) shows the I-V curve of the Au particles modified PD under UV illumination of 380 nm. It is obvious the θ_2 is much larger than θ_1, (θ_1, θ_2 are denoted as the angles between I-V curves in the dark and under the illumination of 380 nm) which means the photocurrent is greatly enhanced by the Au particles modification for the NWs based PD. So as to find out the reasons of the enhanced photocurrent for the Au modified PD, the RT PL of the as grown and the Au particles modified ZnO NWs were performed and shown in Fig 5.6 (b), the SEM image of the NWs modified with Au particles is shown in the inset, it is observed that some small particles deposited on the surface of the NWs. The UV emission peaks centered at 388 nm and 386 nm, the corresponding FWHM of 15 and 17 nm for the as grown and the Au modified ZnO NWs samples are observed, respectively. This UV emission peak could be attributed to exciton-related emission in ZnO. Broad visible emissions ranging from 450 nm to 650 nm with peak position located at about 560 nm was also observed. An obvious characteristic is that the emission intensity in the visible region for Au

particles modified NWs is much weaker than that of the as grown one. This visible emission in ZnO is generally deduced originated from oxygen vacancies. It is known for the Au particles with size ranging from 5 to 20 nm in diameter, the electrons could be trapped in Au nanoparticles resulting in a characteristic collective oscillation frequency of the plasmon resonance, which gives rise to the plasmon resonance band at around 520 nm. [113,114]

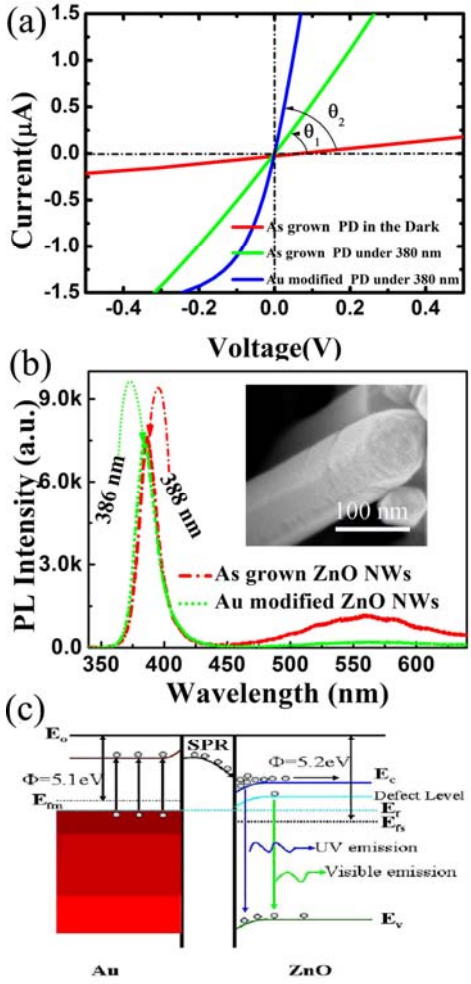

Fig 5.6(a) I-V characteristic curves of the as grown and Au particles modified ZnO NWs based PD in the dark and under UV illumination of 380 nm, respectively. (b) RT PL spectra of the as grown and Au modified ZnO NWs, the inset shows SEM image of Au modified NWs. (c) The energy band structure of Au and ZnO with uniform Fermi Level induced by electron transfer between ZnO and Au.

The Au modified ZnO NWs have weaker visible range light emission compared with that of as grown one, most probably due to light absorption through the SPR of

Au nanoparticles as shown in Fig 5.6 (c), since the work function is smaller for gold than for ZnO NW. [115] When the Au particles are combined with ZnO, the electrons accumulate at the interface leading to a slight blue-shift in the PL, meanwhile causing the downward band bending of the ZnO side. These deficient electrons on the Au surface consequently induce the broadening of the surface plasmon band. [116] It should be noted the UV emission intensity of Au modified ZnO NWs is almost the same as that of the as grown ones. In this case we could consider that the charge separation may play an important role in increasing the photocurrent using Au nanoparticles modification as reported by others. [117,118] The SPR electrons transfer to ZnO causes an increase of the Fermi energy level in the ZnO NWs, which promotes electron density in the conduction band of ZnO and benefits the charge separation for increasing the photocurrent.

In order to explore the detailed information of ZnO based *n*-NWs/i-thin film/*n*-NWs PD, the simplified schematic diagram was depicted as shown in Fig 5.7 (a), the corresponding photocurrent spectrum for the as grown ZnO NWs based PD is shown in Fig 5.7 (c). An obvious characteristic is that a peak shaped photocurrent spectrum was obtained without using filters, which could be called “short wavelength cut-off photoresponse”. Under UV illumination of 380 nm light focused around one electrode of the NWs side, the drifting process should dominate the transport of the carriers due to a strong built-in electric field. Since the built-in electric field across the junction is mainly distributed in the *i* region, photogenerated holes inside the NWs are not efficiently collected by the field unless the minority carrier diffusion length is large. As a result, strong recombination leads to the decrease of the photocurrent. [119] Under UV illumination focused on the *i*-thin film side as shown in Fig 5.7 (b), and the corresponding photocurrent spectrum of as grown PD is shown in Fig 5.7 (d). A new peak for as grown PDs centered at about 351 nm was also observed, which is in accordance with that of the exciton absorption peak position of the ZnO thin film, the peak position in UV region around 350 nm is corresponding to the effective band gap of ZnO due to the presence of high density of states. [120] The Fermi levels for the electrons in the *i*-thin film would shifted to a high level under UV illumination, thus the photogenerated carriers could be easily collected by the electric field, and short wavelength cut-off phenomena disappeared.

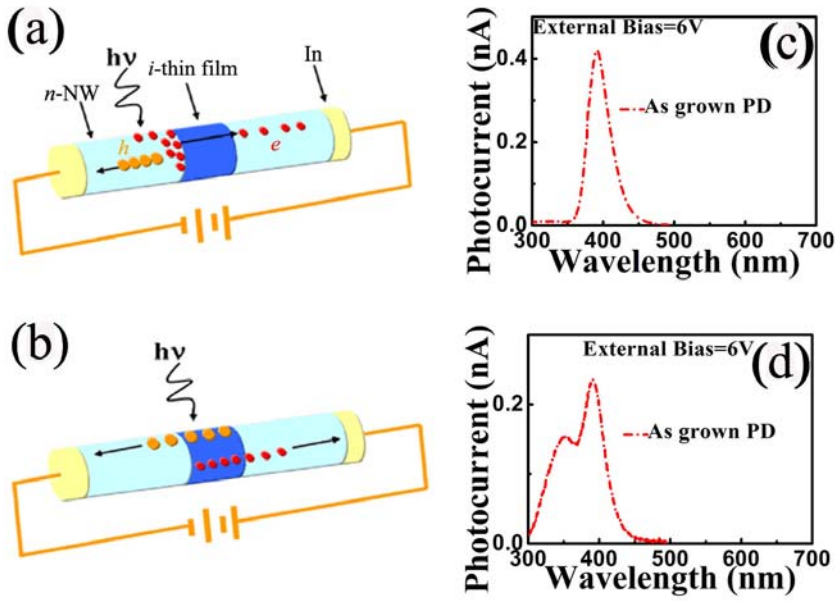

Fig 5.7(a, b) The schematic diagram of the photodetector under different conditions. (c, d) Photocurrent spectra of the as grown ZnO NWs based PDs under corresponding conditions as depicted in (a, b) respectively.

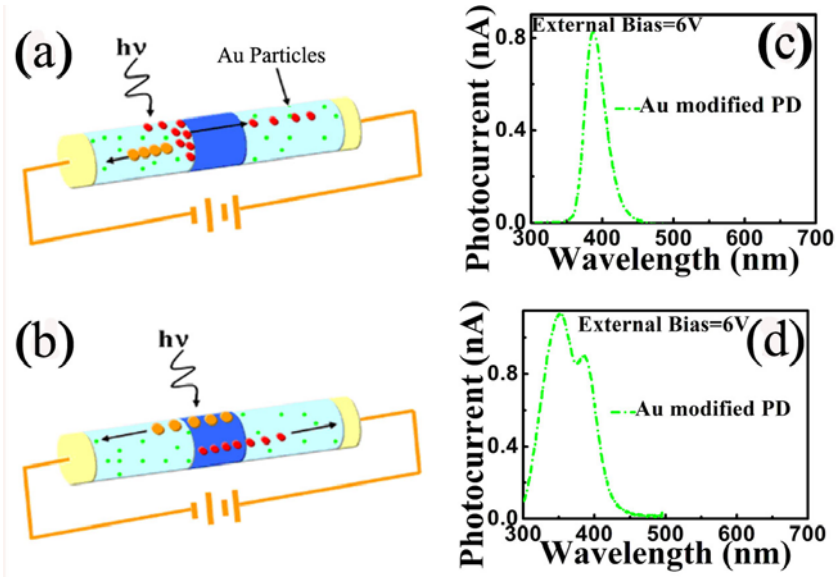

Fig 5.8 (a, b) The schematic diagram of the photodetector under different conditions. (c, d) Photocurrent spectra of the Au modified ZnO NWs based PD under corresponding conditions (a, b).

The similar experimental process has also been performed for the Au nanoparticles modified PD. The photocurrent for the Au modified PD under different

external conditions displayed in Fig 5.8 (a, b) has been largely enhanced as shown in Fig 5.8 (c, d). When the UV light illuminated on the Au particles modified ZnO NWs the photocurrent could be further increased similar as other report, [121] which indicates the SPR electrons could be injected into the conduction band of ZnO and collected by electrode through the electrical field. Such an interfacial charge transfer brings down the recombination probability of electrons and holes. If electrons pass multiple times, this mechanism yields photoconductive gain greater than unity. [122,123]

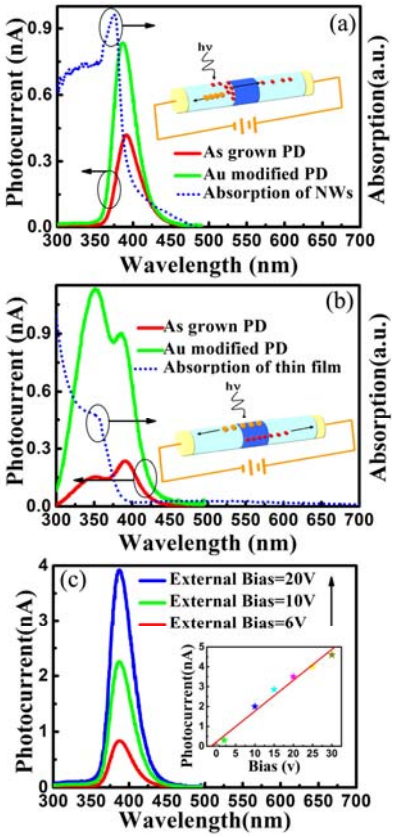

Fig 5.9 (a-b) Photocurrent spectra of the as grown and the Au particles modified PDs under the conditions as depicted in the insets of the Fig 5.9 (a, b). The absorption spectra for the NWs and thin film are also displayed in Fig 5.9 (a, b) respectively. (c) Photocurrent spectra of the Au particles modified PD under the same conditions as shown in Fig 5.9 (a) with changing external bias, the photocurrent of the peak intensity has a linear relationship with the bias shown in the inset.

The photocurrent is proportional to the absorption, the exciton related absorption peak position for the NWs is located at 375 nm as shown in Fig 5.9 (a), the photoresponse signals obtained under the conditions as shown in Fig 5.9 (a) can be attributed to the light absorption of the NWs. The photoresponse peaks located at 351

nm for as grown and Au modified PDs under the conditions depicted in the inserted image shown in Fig 5.9 (b), which is in accordance with that of the exciton absorption peak position of the ZnO thin film. The photocurrent spectra with changing external bias of the Au particles modified PD under the conditions as depicted in the Fig 5.9 (a) are shown in Fig 5.9 (c). The peak position and the corresponding FWHM of about 29 nm is unchanged with increasing the external bias, thus, the maximum photocurrent peak intensity is linearly dependent on the bias voltage shown in the inset of Fig 5.9 (c), which is in agreement with the reported result. [124]

Short wavelength photodetection was realized based on ZnO n-i-n structure, this kind of PD can detect light without filters, this kind of structure may have potential contributions to miniaturize the future PDs.

5.3 Conclusion

This chapter introduces some research work on the ZnO based PDs: visible and UV light alternative photodetector was realized combining Si and ZnO materials; short wavelength cut-off PD without using any filters was realized based on n-i-n structure.

1. ZnO NW array/n-Si heterojunction has been fabricated by a magnetron cosputtering method. The heterojunction showed a rectification ratio of above 1.6×102 at 4 V in the dark. A PD working in either visible or ultraviolet regions was achieved by applying forward or reverse biases on the heterojunction. We believe that this technique is very useful to integrate PDs with different cut off wavelengths on one chip.
2. Short wavelength cut-off properties for the ZnO based n-NWs/i-thin film/n-NWs PDs was realized without using filters, the photoresponse properties of the devices were discussed in terms of the n-i-n structure and the carrier transport processes. This kind of ZnO nanostructure based PDs without using filters may have potential applications in minimizing the size for the PDs in the future.

Chapter 6 Conclusion and Outlook

6.1 Conclusion

The dissertation focuses on the preparation of ZnO nano-material, optically pumped lasers, electrically pumped lasers, ZnO based LEDs and PDs, some initial research has been performed, the obtained results are listed as follows:

1. Concerning the preparation of ZnO nano-material: physical vapor deposition method have been used to obtain ZnO nanobolt arrays. The growth mechanism, the structure and optical properties were studied. The growth mode can be changed from 1D to 2D growth by introducing oxygen gas. Diameter and length of ZnO NWs could be adjusted to achieve the growth by hydrothermal method, it is observed that size of seed particle and concentration of the solution will affect diameter of epitaxial NWs, the effects of annealing atomosphere on the seed layer will influence the growth rate of epitaxial NWs, the size of epitaxial ZnO NWs can be tuned by growth parameters. Current and voltage characteristic for ZnO NWs and nanorods was measured combining intedigital electrodes, due to the interface barrier homojunction based on NWs and nanorods has been obtained.
2. Aligned ZnO NW array was fabricated on ZnO seed layer which was annealed at 1000 ° C in air by hydrothermal method, and the stimulated laser emission was realized in aligned nanowires array. Its threshold was 96 KW/cm^2; ZnO NWs grown on Si substrate were optically pumped with Pt as high reflectivity mirror, a lower threshold 17.3 KW/cm^2 was realized for the optically pumped laser emission.
3. Closely packed ZnO microcrystalline thin film was obtained through multiple growths on p-GaN wafer by hydrothermal method, and edge electrically pumped single-mode laser emission was realized. Using polymer as carrier blocking layer, ultralow driven current UV - blue light

emitting diode based on n-ZnO NWs / i-polymer / p-GaN heterojunction was realized.

4. Closely packed ZnO NWs were prepared on n-Si substrate by magnetron sputtering, and visible and UV light alternative PD was realized. PD based on n-ZnO NWs/i-film/n-ZnO NWs was prepared by magnetron sputtering method and hydrothermal method, short-wave cut-off PD without any filters was realized, the photocurrent was further enhanced by Au particles modification on the surface of the NWs.

6.2 Outlook

I would like to make an outlook based on the understanding of the present literatures and my experimental research, the details are listed as follows:

1. Optically pumped ZnO NWs lasers with lower threshold and excellent emission direction will be realized, and these nano-lasers can realize information storage, my be the basic storage unit of the computer will be replaced by ZnO nanostructures. Electrically pumped ZnO UV-blue lasers owning single mode and controllable emission direction could be realized; through the hard work of the scientific researchers, once the ZnO p-type doping problem was solved, UV-blue displays based on ZnO homojunction LEDs could be realized, and the resolution of display will be further improved combining ZnO nanostructures.
2. Concerning ZnO based PDs, chips with different wavelength detection (such as ZnMgO PDs with component adjustable) could be integrated onto only one mirco-wafer, light detection of different wavelength could be realized by controlling the bias or the value of the bias. Short wavelength cut-off PD was realized based on *n-i-n* structure according to my experiment without using any filters, hence, short wavelength cut-off PD could be realized based on only single NW without filters, and single NW PD owning characteristics such as high gain and fast response will be born without using filters.

References

[1] Klingshirn C. The Luminescence of ZnO under One and Two-Quantum Excitation[J]. Phys. Status Solid (b). 1975, 71(2)：547-556.
[2] Liang W Y, Yoffe A D. Transmission Spectra of ZnO Single Crystals[J]. Phys. Rev. Lett, 1968, 20(2): 59–62.
[3] Jin B J, Bae S H, Lee S Y, et al. Effects of native defects on optical and electrical properties of ZnO prepared by pulsed laser deposition, Materials Science and Engineering B[J]. 2000, 71(1-3): 303-305.
[4] Bagnall D M, Chen Y F, Zhu Z, et al. Opticallly pumped lasing of ZnO at room temperature. Appl.PhysLett[J], 1997, 70(17): 2230-2232.
[5] Tang Z K, Wong G K L, Yu P, et al. Room-temperature ultraviolet laser emission from self-assembled ZnO microcrystallite thin films[J], Appl.Phys.Lett, 1998,72(27): 3270—3272.
[6] Yu P, Tang Z K, Wong G K L, et al.Ultraviolet spontaneous and stimulated emission from ZnO mictrocrystallite thin films at room temperature[J]. Solid State Com, 1997, 103(8): 459-463.
[7] Cao H, Zhao Y G, Ong H C, et al. Ultraviolet lasing in resonators formed by scattering in semiconductor polycrystalline films[J]. Appl.Phys.Lett, 1998, 73(25): 3656-3658.
[8] Cao H, Y. G. Zhao. Random Laser Action in Semiconductor Powder[J]. Phys. Rev. Lett, 1999, 82(11): 2278-2281.
[9] Cao H, Xu J Y,Zhang D Z. Spatial Confinement of Laser Light in Active Random Media[J]. Phys. Rev. Lett, 2000,84(24): 5584-5587.
[10] Huang Michael H, Mao Samuel, Yang Peidong, et al. Room-Temperature Ultraviolet[J].Science, 2001,292: 1897-1899.
[11] Leong Eunice S P, Yu Siu Fung. UV Random Lasing Action in p-SiC(4H)/i-ZnO–SiO2 Nanocomposite/n-ZnO:Al Heterojunction Diodes[J]. Adv. Mater. 2006, 18: 1685–1688.
[12] Ma Xiangyang,Chen Peiliang, Yang Deren, et al. Electrically Pumped ZnO Film Ultraviolet Random Lasers On Silicon Substrate[J]. Appl.Phys.Lett, 2007, 91(25): 251109-251112.
[13] Chu Sheng,Olmedo Mario, Liu Jianlin, et al.Electrically Pumped Ultraviolet ZnO diode Lasers On Si[J]. Appl.Phys.Lett, 2008, 93(18): 181106-181108.
[14] Zhu Hai,Shan Chongxin,Yao bin,et al.Ultralow Threshold Laser Realized in Zinc Oxide[J]. Adv. Mater. 2009, 21: 1613–1617.
[15] Zhu Hai,Shan Chongxin,Yao bin,et al.Ultralow Threshold Laser Realized in Zinc Oxide[J]. Adv. Mater, 2009, 22: 1877–1881.
[16] Leong Eunice S P, Chong M K,Yu Siu Fung,et al. Sol–Gel ZnO–SiO2 Composite Waveguide Ultraviolet Lasers[J]. IEEE Photonics Technol Lett, 2004, 16(11): 2418–2420.
[17] Tsukazaki Atsushi, Othomo Akira, Kawasaki Masashi,et al. Repeated temperature modulation epitaxy for p-type doping and light-emitting diode based on ZnO[J]. Nature Materials, 2005, 4, 42-46.
[18] Jiao S J, Zhang Z Z, Lu Y M, et al. ZnO p-n junction light-emitting diodes fabricated on sapphire substrates[J]. Appl.Phys.Lett, 2006, 88(3): 031911-031913.
[19] Wei Z P, Lu Y M, Zhang Z Z, et al.Room temperature *p-n* ZnO blue-violet

light-emitting diodes [J]. Appl.Phys.Lett, 2007, 90(3): 042113-042115.
[20] Lim Jae-Hong, Kang Chang-Ku,Park Seong-Ju, et al. UV Electroluminescence Emission from ZnO Light-Emitting Diodes Grown by High-Temperature Radiofrequency Sputtering[J]. Adv. Mater, 2006, 18: 2720-2724.
[21] Xu W Z, Ye Z Z, Zeng Y J, et al. ZnO light-emitting diode grown by plasma-assisted metal organic chemical vapor deposition[J]. Appl.Phys.Lett, 2006, 88(17): 173506-173508.
[22] Ye J D,Gu S L,Zhu S M, et al. Electroluminescent and transport mechanisms of *n*-ZnO/*p*-Si heterojunctions[J]. Appl.Phys.Lett, 2006, 88(17): 182112-182114.
[23] Alivov Ya I,Nostrand J E Van,Look D C , et al. Observation of 430 nm electroluminescence from ZnO/GaN heterojunction light-emitting diodes[J]. Appl.Phys.Lett, 2003, 83(14): 2948-2951.
[24] Hwang Dae-Kue, Kang Soon-Hyung, Park Seong-Ju, et al. p-ZnO/ n-GaN heterostructure ZnO light-emitting diodes[J]. Appl.Phys.Lett, 2005, 86(22): 222101-222103.
[25] Rongers D J, Teherani F Hosseini, Yasan A, et al. Electroluminescence at 375 nm from a ZnO/GaN:Mg/*c*-Al_2O_3 heterojunction light emitting diode[J]. Appl.Phys.Lett, 2006, 88(14): 141918-141921.
[26] Jeong Min-Chang, Oh Byeong-Yun, Myoung Jae-Min, et al. ZnO-Nanowire-Inserted GaN/ZnOHeterojunction Light-Emitting Diodes[J]. Small, 2007, 3(4): 568-572.
[27] Zhong J,Chen H,Saraf G, et al. Integrated ZnO nanotips on GaN light emitting diodes for enhanced emission efficiency[J]. Appl.Phys.Lett, 2009, 90(20): 203515-203517.
[28] Liang S,Sheng H,Lu Y , et al. ZnO Schottky ultraviolet photodetectors[J].J.Cryst.Growth, 2001, 225: 110-113.
[29] Law J B K, Thong J T L. Simple fabrication of a ZnO nanowire photodetector with a fast photoresponse time[J]. Appl.Phys.Lett, 2006, 88(13): 133114-133116.
[30] Soci C, Zhang A, Wang D, et al. ZnO Nanowire UV Photodetectors with High Internal Gain[J]. Nano Lett, 2007,7(4): 1003-1009.
[31] Jin Yizheng, Wang Jianpu, Greenham Neil C, et al. Solution-Processed UltravioletPhotodetectors Based on Colloidal ZnO Nanoparticles[J]. Nano Lett, 2008,8(6): 1649-1653.
[32] Kind Hannes, Yan Haoquan, Yang Peidong, et al. Nanowire Ultraviolet Photodetectors and Optical Switches[J]. Adv. Mater, 2002, 14(2): 158-160.
[33] Kumar, Sanjeev, Gupta, Vinay, Sreenivas, K Sreenivas.Synthesis of photoconducting ZnO nano-needles using an unbalanced magnetron sputtered ZnO/Zn/ZnO multilayer structure[J]. Nanotechnology, 2005, *16*, 1167-1171.
[34] Fan Z Y, Chang P C, Lu J G, et al. Photoluminescence and polarized photodetection of single ZnO nanowires[J]. Appl.Phys.Lett, 2004, 85(25): 6128-6131.
[35] Li Q H, Gao T, Wang Y G,et al. Adsorption and desorption of oxygen probed from ZnO nanowire films by photocurrent measurements[J]. Appl.Phys.Lett, 2005, 86(12): 123117-123120.
[36] Li Q H, Wan Q, Liang Y X, Wang T H, et al. Electronic transport through individual ZnO nanowires[J]. Appl. Phys. Lett, 2004, 84(22): 4556-4558.
[37] Li Q H, Liang Y X, Wan Q, et al. Oxygen Sensing Characteristics of individual ZnO nanowire transistors[J]. Appl. Phys. Lett, 2004, 85(26): 6389-6391.
[38] Mehta R R, Sharma B S. Photoconductive gain greater than unity in CdSe films with Schottky barriers at the contacts[J]. J. Appl. Phys. 1973, 44(1), 325-328.
[39] Zhao Minhua,Wang Zhong Lin,Mao Scott X. Piezoelectric Characterization of Individual Zinc Oxide Nanobelt Probed by Piezoresponse Force Microscope[J]. Nano Lett, 2004, 4(4): 587-590.
[40] Wang Zhong Lin, Song Jinhui. Piezoelectric Nanogenerators Based on Zinc Oxide Nanowire Arrays[J]. Science, 2006,312: 242-246.

[41] Song Jinhui，Zhou Jun, Wang Zhong Lin. Piezoelectric and SemiconductingCoupled Power Generating Process of aSingle ZnO Belt/Wire. A Technology for Harvesting Electricity from the Environment[J].Nano Letters, 2006,6(8): 1656-1662.
[42] Yang Rusen，Qin Yong, Wang Zhong Lin. Power generation with laterally packaged piezoelectric fine wires[J].Nature Nanotechnology, 2008,4: 34-39.
[43] Wang Z L, Kong X Y, Zuo J M. Induced growth of asymetric nanocantilever arrays on polar surfaces [J]. Phys. Rev. Lett, 2003, 91(18): 185502-185505.
[44] Wang Z L, Song J H. Piezoelectric Nanogenerators Based on Zinc Oxide Nanowire Arrays[J]. Science, 2006, 312(5771): 242-246. See supporting material on Science Online.
[45] Vispute R D, Talyansky V, Trajanovic Z, et al. High quality crystalline ZnO buffer layers on sapphire (001) by pulsed laser deposition for III–V nitrides[J]. Appl.Phys.Lett, 1997, 70(20): 2735-2737.
[46] Makino T, Chia C H, Kawasaki M, et al. Exciton spectra of ZnO epitaxial layers on lattice-matched substrates grown with laser-molecular-beam epitaxy[J]. Appl.Phys.Lett, 2000, 76(24): 3549-3552.
[47] Ko H J, Chen Y. F, Yao T, et al. Biexciton emission from high-quality ZnO films grown on epitaxial GaN by plasma-assisted molecular-beam epitaxy [J]. Appl.Phys.Lett, 2000, 77(4): 537-539.
[48] Nakanishi Yoichiro, Miyake Aki, Kominami Hiroko, et al. Preparation of ZnO thin films for high-resolution field emission display by electron beam evaporation[J].Applied Surface Science, 1999, 142(1-4): 233-236.
[49] Carcia P F, McLean R S, Reilly M H**,** et al. Transparent ZnO thin-film transistor fabricated by rf magnetron sputtering[J]. Appl.Phys.Lett, 2003, 82(7): 1117-1119.
[50] Wagner R S, Ellis W C.Vapor-liquid-solid mechanism of single crystal growth[J]. Appl.Phys.Lett,1964,4(5): 89-91.
[51] Wang Y W, Zhang L D, Wang G Z, et al. Catalytic growth of semiconducting zinc oxidenanowires and their photoluminescence properties[J]. J.Crys.Grow.2002, 234,171-175.
[52] Ng H T, Chen B, Li J, et al.Optical properties of single-crystalline ZnO nanowires on *m*-sapphire[J]. Appl.Phys.Lett, 2003,82,2023-2025.
[53] Zhao Q X, Willander M, Morjan R R, et al. Optical recombination of ZnO nanowires grown on sapphire and Si substrates[J]. Appl. Phys. Lett. 2003, 83, 165-167.
[54] Wang Xudong, Summers Christopher J, Wang Zhong Lin. Large-Scale Hexagonal-Patterned Growth of Aligned ZnO Nanorods for Nano-optoelectronics and Nanosensor Arrays[J]. Nano.Lett,2004,4,423-426.
[55] Umar A, Kim S H Hahn Y B, et al. Catalyst-free large-quantity synthesis of ZnO nanorods by a vapor–solid growth mechanism: Structural and optical properties[J]. Journal of Crystal Growth, 2005, 282(1-2): 131-136.
[56] Liu Y F, Zheng J H, Zhang W X, et al. Solvothermal route to Bi_3Se_4 nanorods at low temperature[J]. J.Mater. Res, 2001,16,3361-3365.
[57] Choy J H, Jang E S, Won J H, et al. Soft Solution Route to Directly Grown ZnO Nanorod Arrays on Si Wafer:Room Temperature Ultraviolet Laser[J]. Adv.Mater, 2003, 15,1911-1914.
[58] Tong Y H, Liu Y C, Shao C L, et al.Structural and Optical Properties of ZnO Nanotower Boundles[J].Appl.Phys.Lett.2006,88(12):123111-123113.
[59] Peulon Sophie, Lincot Daniel. Cathodic electrodeposition from aqueous solution of dense or open-structured zinc oxide films[J]. Adv. Mater. 1996, 8(2): 166-170.
[60] Izaki Masanobu, Omj Takashi. Transparent zinc oxide films prepared by electrochemical reaction[J]**.** Appl. Phys. Lett 1996, 68(17): 2439-2440.
[61] Li Y, Meng G W, Zhang L D,et al. Ordered semiconductor ZnO nanowire arrays and

their photoluminescence properties[J]. Appl. Phys. Lett. 2000,76(15): 2011-2013.
[62] Huckzko A. Template-based synthesis of nanomaterials，Appl. Phys. A-Mater[J]. 2000，70: 365-376.
[63] Ma Jinxin, Zhu Guokai. Introduction of Scanning Electron Microscope[M]. Beijing：Science Press, 1985. p49.
[64] Wang Zhonglin. Zinc oxide nanostructures: growth, properties and Applications[J]. J. Phys. Condens. Matter, 2004, 16: 829-858.
[65] Vanheusden, K.; Warren, W. L.; Seager, C. H. et al. Mechanisms behind green photoluminescence in ZnO phosphor powders[J].J Appl.Phys, 1996, 79, 7983-7990.
[66] Zhao Q X, Willander M, Hu Q-H, et al. Optical recombination of ZnO nanowires grown on sapphire and Si substrates[J]. Appl. Phys.Lett, 2003, 83(1): 165-167.
[67] American Standard for Testing of Materials (ASTM) 36,1451.
[68] A. Segmüller and M. Murakami. Analytical Techniques for Thin Films edited by K.N. Ellmer, K. Wiesemann. (Acad., Boston, 1988) 143.
[69] Bateman T B. Elastic Moduli of Single-Crystal Zinc Oxide[J].J. Appl. Phys，1962，33 (11)：3309-3312.
[70] S.M. Sze. In: Semiconductor Devices Physics and Technology, Wiley. (2002) 538.
[71] Lee H W, Lau S P, Wang Y G, et al. Internal stress and surface morphology of zinc oxide thin films deposited by filtered cathodic vacuum arc technique[J]. Thin Solid Films, 2004, 458 (1-2): 15-19.
[72] Gupta Vinay，Mansingh Abhai.Influence of postdeposition annealing on the structural and optical properties of sputtered zinc oxide film[J]. J. Appl. Phys，1996， 80 (2)：1063-1073.
[73] Klug H P, Alexander L E. In X-Ray Diffraction Procedures for Polycrystalline and Amorphous Materials. (Wiley, New York, 1974) 687.
[74] Hickernell F S. MRS spring meeting San Francisco, California. (1985).
[75] Wong Eva M, Searson Peter C. ZnO quantum particle thin films fabricated by electrophoretic deposition[J].Appl. Phys. Lett. 1999，74 (20)：2939-2941.
[76] Aoki T, Hatanaka Y, Look D C. ZnO diode fabricated by excimer-laser doping[J].Appl. Phys. Lett，2000，76 (22)： 3257-2359.
[77] Xu W Z，Ye Z Z, Zeng Y J. ZnO light-emitting diode grown by plasma-assisted metal organic chemical vapor deposition[J].Appl. Phys. Lett. 2006，88 (17)：173506-173508.
[78] Cebulla R, Weridt R, Ellmer K. Al-doped zinc oxide films deposited by simultaneous rf and dc excitation of a magnetron plasma: Relationships between plasma parameters and structural and electrical film properties[J]. J. Appl. Phys, 1998, 83 (2): 1087-1095.
[79] Li Z, Xiong Y, Xie Y. Selected-Control Synthesis of ZnO Nanowires and Nanorods via a PEG-Assisted Route[J].Inorganic Chemistry, 2003，42 (24)： 8105-8109.
[80] Wiersma D S, Albada M P van, Tiggelen B A Van, et al. Experimental Evidence for Recurrent Multiple Scattering Events of Light in Disordered Media[J]. Phys. Rev. Lett, 1995, 74(21): 4193-4196.
[81] Zimmler Mariano A, Capasso Federico, M uller Sven, et al. Optically pumped nanowire lasers:invited review[J]. Semicond. Sci. Technol, 2010, 25 (2): 024001(12pp).
[82] Vanheusden K, Warren W L, Seager C H, et al. Mechanisms behind green photoluminescence in ZnO phosphor powders[J]. J. Appl. Phys. 1996, 79（10）: 7983-7990.
[83] Bagnall D M, Chen Y F, Zhu Z, et al. Optically pumped lasing of ZnO at room temperature[J]. Appl. Phys. Lett, 1997, 70(17): 2230-2232.
[84] Saleh B E A，Teich M C. Fundamentals of Photonics (Wiley, New York, 1991).
[85] Yamamoto Y, Machida S, Bjork G. Microcavity semiconductor laser with enhanced

laser emission[J]. Phys. Rev. A, 1991, 44(1): 657-668.
[86] Kim J H, Kim E-M, Andeen D. et al. Growth of Heteroepitaxial ZnO Thin Films on GaN-Buffered Al2O3 (0001) Substrates by Low-Temperature Hydrothermal Synthesis at 90 °C[J]. Adv. Funt. Mater, 2007, 17(3): 463-471.
[87] Nakamura S， Mukai T， Senoh M. Jpn. J. Appl. Phys. 1991, Part 2, 30, L1998.
[88] Milnes A G， Feucht D L. Heterojunctions and Metal-Semiconductor Junctions. Academic: New York, 1972.
[89] Aranovich J A, Golmayo D G, Fahrenbruch A L, et al. Photovoltaic properties of ZnO/CdTe heterojunctions prepared by spray pyrolysis[J]. J. Appl. Phys, 1980, 51(8), 4260-4268.
[90] Qiao, D.; Yu, L. S.; Lau, S. S.; et al. Dependence of Ni/AlGaN Schottky barrier height on Al mole fraction[J]. J. Appl. Phys, 2000, 87(2), 801-804.
[91] Li H D, Yu S F, Lau S P, et al. High-Temperature Lasing Characteristics of ZnO Epilayers[J]. Adv. Mater, 2006, 18(6): 771-774.
[92] Fu H K, Cheng C L, Wang C H, et al.Selective angle electroluminescence of light-emitting diodes based on nanostrucutred ZnO/GaN heterojunctions[J]. Adv. Funct Mater. 2009，19, 3471.
[93] Hwang D K, Kang S H, Lim J H, et al.*p*-ZnO/*n*-GaN heterostructure ZnO light-emitting diodes[J].Appl. Phys. Lett, 2005,86(22): 222101.
[94] J. Zhong, Chen H, Saraf G, et al. Integrated ZnO nanotips on GaN light emitting diodes for enhanced emission efficiency[J]. Appl. Phys. Lett. 2007, 90(20): 203515-203517.
[95] Park W I， Yi G C.Electroluminescence in n-ZnO nanorods arrays vertically grown on P-GaN[J]. Adv. Mater, 2004, 16(1): 87-90.
[96] Jeong M C, Oh B Y, Ham M H, et al. Electroluminescence from ZnO nanowires in *n*-ZnO film/ZnO nanowire array/*p*-GaN film heterojunction light-emitting diodes[J].Appl. Phys. Lett. 2006, 88(20): 202105-202107.
[97] Rogers D J, Teherani F Hossein. Electroluminescence at 375 nm from a ZnO/GaN:Mg/*c*-Al_2O_3 heterojunction light emitting diode[J].Appl. Phys. Lett. 2006, 88(14): 141918-141920.
[98] Chen C P, Ke M Y, Liu C C, et al. Observation of 394 nm electroluminescence from low-temperature sputtered *n*-ZnO/SiO_2 thin films on top of the *p*-GaN heterostructure Appl. Phys. Lett. 2007, 91(9): 091107-091109.
[99] You J B, Zhang X W, Zhang S G, et al. Improved electroluminescence from n-ZnO/AlN/p-GaN heterojunction light-emitting diodes[J]. Appl. Phys. Lett. 2010, 96(20): 201102-201104.
[100] Zhu H, Shan C X, Yao B, et al. Ultralow-threshold laser realized in Zinc Oxide[J].Adv. Mater, 2009, **21**(16): 1613-1617.
[101] Mandalapu L J, Xiu F X, Yang Z, et al. p-type behavior from Sb-doped ZnO heterojunction photodiodes[J], Appl. Phys.Lett, 2006, 88(11): 112108-112110.
[102] Fedison J B, Chow T P, Lu H, et al.Electrical characteristics of magnesium-doped gallium nitride junction diodes[J],Appl. Phys. Lett, 1998,72(22): 2841-2843.
[103] Ghosh R, Basak D, Electrical and ultraviolet photoresponse properties of quasialigned ZnO nanowires/p-Si heterojunction[J],Appl. Phys. Lett,2007,90, 243106-243108.
[104] S. M. Sze, Physics of Semiconductor Devices, 2nd ed. （Wiley, New York,1981）.
[105] Aranovich J A, Golmayo D G, Fahrenbruch A L, et al.Photovoltaic properties of ZnO/CdTe heterojunctions prepared by spray pyrolysis[J],J.Appl. Phys. 1980,51(8): 4260-4268.
[106] Tan S T, Sun X W, Zhao J L, et al.Ultraviolet and visible electroluminescence from n-ZnO/SiO_x/(n,p)-Si heterostructured light-emitting diodes[J], Appl. Phys. Lett. 2008,93(1): 013506-013508.

[107] Kouklin, N. Cu-doped ZnO nanowires for efficient and multispectral photodetection applications[J],Adv. Mater. 2008, 20(11): 2190–2194.
[108] Adivarahan V， Simin G， Yang J W， et al. SiO_2-passivated lateral-geometry GaN transparent Schottky-barrier detectors[J],Appl. Phys. Lett. 2000, 77(6): 863-865.
[109] Harnack O, Pacholski C, Weller H, et al. Rectifying Behavior of Electrically Aligned ZnO Nanorods[J],Nano Lett. 2003, 3(8): 1097-1101.
[110] Lao C S, Liu J, Wang Z L, et al. ZnO Nanobelt/Nanowire Schottky Diodes Formed by Dielectrophoresis Alignment across Au Electrodes[J],Nano Lett. 2006, 6(2): 263-266.
[111] Liao Z-M, Xu J, Zhang J-M, et al. Photovoltaic effect and charge storage in single ZnO nanowires[J],Appl. Phys. Lett. 2008, 93(2): 023111-023113.
[112] Yuan G D，Zhang W J，Lee S T，et al. p-Type ZnO Nanowire Arrays [J],Nano Lett. 2008, 8(8): 2591-2597.
[113] Daniel M-C, Astruc D. Gold Nanoparticles: Assembly, Supramolecular Chemistry, Quantum-Size-Related Properties, and Applications toward Biology, Catalysis, and Nanotechnology[J]. Chem. Rev, 2004, 104(1): 293-346.
[114] Yu H, Chen M, Rice P M, et al. Dumbbell-like Bifunctional Au−Fe_3O_4 Nanoparticles[J]. Nano Lett. 2005, 5(2): 379-382.
[115] Wang, X.; Summers, C. J.; Wang, Z. L. Self-attraction among aligned Au/ZnO nanorods under electron beam[J].Appl. Phys. Lett. 2005, 86（1）：013111.
[116] Cao, Y. W.; Jin, R.; Mirkin, C. A. DNA-Modified Core−Shell Ag/Au Nanoparticles[J].J. Am. Chem. Soc. 2001, 123（32）：7961-7962.
[117] Said B,Surat H. Enhanced charge separation in chlorophyll a solar cell by gold nanoparticles[J].J. Appl. Phys, 2004, 96(12): 7744-7746.
[118] Tian Y, Tatsuma T. Mechanisms and Applications of Plasmon-Induced Charge Separation at TiO_2 Films Loaded with Gold Nanoparticles[J]. J. Am. Chem. Soc. 2005, 127(20): 7632–7637.
[119] Xu G Y， Salvador A， Kim W，et al. High speed, low noise ultraviolet photodetectors based on GaN p-i-n and AlGaN(p)-GaN(i)-GaN(n)structures[J].Appl. Phys. Lett. 1997, 71（15）：2154-2156.
[120] Mandalapu L J， Xiu F X， Yang Z，et al. p-type behavior from Sb-doped ZnO heterojunction photodiodes[J].Appl. Phys. Lett. 2006. 88(11): 112108-112110.
[121] Fukuda M, Aihara T, Yamaguchi K, et al. Light detection enhanced by surface plasmon resonance in metal film[J].Appl. Phys. Lett. 2010, 96(15): 153107-153109.
[122] Mehta R R, Sharma B S. Photoconductive gain greater than unity in CdSe films with Schottky barriers at the contacts[J].J. Appl. Phys. 1973, 44(1): 325-328.
[123] Katz O, Garber V, Meyler B, et al. Gain mechanism in GaN Schottky ultraviolet detectors[J]. Appl. Phys. Lett. 2001, 79(10): 1417-1419.
[124] Basaka D， Amin G， Mallik B，et al.Photoconductive UV detectors on sol-gel-synthesized ZnO films[J]. Journal of Crystal Growth. 2003, 256(1-2): 73–77.

Academic Achievements

Articles Published：

1. **Guo Zhen**, Zhao Dongxu, Shen Dezhen, Fang Fang, Zhang Jiying, and Li Binghui, Structure and photoluminescence properties of aligned ZnO nanobolt arrays, Crystal Growth & Design, 2007, 7, (2294). (SCI)
2. **Guo Zhen**, Zhao Dongxu, Liu Yichun, Shen Dezhen, Zhang Jiying, and Li Binghui, Visible and ultraviolet light alternative photodetector based on ZnO nanowire/*n*-Si heterojunction[J]. APPLIED PHYSICS LETTERS, 2008, 93, (163501). (SCI)
3. **Guo Zhen**, Zhang Hong, Zhao Dongxu, Liu Yichun, Yao Bin, Li Binghui, Zhang Zhenzhong, and Shen Dezhen, The ultra-low driven current ultraviolet-blue light-emitting diode based on n-ZnO nanowires/i-polymer/p-GaN heterojunction[J]. APPLIED PHYSICS LETTERS, 2010, **97**, (173508). (SCI)
4. **Guo Zhen**, Zhao Dongxu, Liu Yichun, Shen Dezhen, Yao Bin, Zhang Zhenzhong and Li Binghui, Electrically Pumped Single Mode Lasing Emission of Self-Assembled n-ZnO Microcrystalline Film/p-GaN Heterojunction Diode[J]. The Journal of Physical Chemistry, 2010, 114, (15499). (SCI)
5. **Guo Z,** Andreazza-Vignolle C, Andreazza P, Sauvage T, Zhao D.X. , Liu Y.C, Yao B, Shen D.Z, Fan X.W. Tuning the growth of ZnO nanowires[J]. Physica B, 2011, 46, (2200). (SCI).
6. **Guo Zhen**, Andreazza-Vignolle Caroline, Andreazza Pascal, Zhao Dongxu，Liu Yichun, Zhang Ligong, Li Binhui, Zhang Zhenzhong, Shen Dezhen, The lasing action observed in the aligned ZnO nanowires[J]. Accepted by "Chinese Journal of Luminescence" (EI), in press.
7. **Guo Zhen**, Zhao Dongxu, Andreazza-Vignolle Caroline, Andreazza Pascal, Liu Yichun, Shen Dezhen, Yao Bin, Zhang Zhengzhong, Li Binghui, Short wavelength cut-off for the ZnO based nanowires/thin film/nanowires

photodetector[J]. Submitted to The Journal of Physical Chemistry, (SCI), under review.

8. **Guo Zhen,** Andreazza-Vignolle C, Andreazza P, Sauvage T, Zhao D.X. ,Liu Y.C, One dimensional ZnO based homotype homojunction[J]. Submitted to Applied Surface Science. (SCI), under review.
9. **Guo Zhen**, Zhao Dongxu， Zhang Ligong, Andreazza-Vignolle Caroline, Andreazza Pascal, Liu Yichun, Li Binghui, Zhang Zhengzhong, Shen Dezhen, The Ultra-low threshold for the optically pumped lasing emission in the ZnO nanowires[J]. Submitted to Nano Letters, (SCI).

Zhen GUO

Préparation de nanostructures de ZnO et intégration dans des dispositifs photoélectriques

Résumé :
L'oxyde de Zinc (ZnO) est un oxyde semi-conducteur à large bande interdite dont un paramètre primordial est la valeur importante de l'énergie du premier exciton. Ces caractéristiques font de ZnO un matériau à fort potentiel applicatif notamment pour l'électronique.
Cette thèse développe d'une part l'étude de la croissance contrôlée de nanostructures de ZnO sur différents supports et d'autre part l'étude de l'intégration de telles nanostructures dans des nano-composants.
Plusieurs méthodes de préparation ont été utilisées au cours de ce travail : l'élaboration par voie chimique en phase vapeur et la synthèse hydrothermale qui ont permis l'obtention de nanofils, « nanopilliers » de taille et de densité variables pouvant être alignés perpendiculairement au support. L'intégration de ces réseaux alignés de nanofils dans des nano-composants a montré une émission stimulée par pompage optique utilisant un laser femtoseconde présentant un seuil de 96KW/cm^2. Une couche de platine utilisée comme miroir de haute réflectivité a par ailleurs montré une diminution du seuil jusque 17.3KW/cm^2.
Des microtiges de ZnO présentant un arrangement périodique avec des faces parallèles entre elles, obtenues sur un film mince monocristallin de GaN, a permis l'obtention d'une cavité résonante de qualité. Par pompage optique, une émission stimulée est observée dans ces hétérojonctions GaN / micro-tiges de ZnO. Des expériences d' électoluminescence ont montré une raie d'émission unique centrée à 407nm avec une largeur à mi-hauteur de 0.7nm. L'analyse par photoluminescence de ces hétérojonctions a montré que cette émission provenait des micro-tiges de ZnO. Enfin, des réseaux très compacts de nanofils de ZnO sur substrat de silicium ont été obtenus par pulvérisation magnétron et ont permis la conception de nano-photodetecteurs.

The Research on Preparation of ZnO Nano-material and Photoelectric Devices

Abstract:
ZnO is a wide band gap semiconductor material, which has a band gap of 3.37 eV at room temperature, its most important characteristic is the high exciton bounding energy of 60 meV. Based on these characteristics, ZnO has potential applications in short wavelength photoelectric devices.
The dissertation develops the following creative research on the problems of the growth controlled ZnO nanostructures, design and preparation of nanodevices. Exploring chemical vapor deposition method, through controlling the oxygen flux, the conversion from 1D to 2D growth was realized, thus ZnO nanobolt arrays were obtained; exploring hydrothermal method, through adjusting the size of the seed particle and solution concentration, ZnO nanowires with different size were obtained. The stimulated emission were observed with threshold of 96 KW/cm^2 excited by femtosecond laser in the optically pumped aligned ZnO nanowires; in order to lower the threshold of the stimulated emission, Pt layer as a high reflectivity mirror was fabricated on Si substrate, optical loss has been effectively decreased, thus the threshold of the stimulated emission was further lowered to 17.3 KW/cm^2 for the optically pumped ZnO nanowires. The ZnO microcrystalline film obtained by hydrothermal method with multiple growth present periodically arranged structure with parallel sides. The electrically pumped single mode lasing emission located at 407 nm with FWHM of 0.7 nm was obtained based on ZnO microcrystalline film /p-GaN heterojunction. Closely packed ZnO nanowire array was fabricated on Si substrate by magnetron sputtering method, the visible and UV dual bands alternative photo-detection was realized through adjusting forward and reverse bias.

CRMD, 1b rue de la férollerie 45071 Orléans Cedex 2, France.
Changchun Institute of Optics, Dong Nanhu Road 3888 Changchun 130033 Jilin, China.